Thesis for a Ph.D. Degree

Influences of ENSO and QBO on East Asian winter surface climate on sub-seasonal to seasonal timescale

ENSO와 QBO가 겨울철 동아시아 지상 기후에 미치는 계절내-계절 영향

August 2023

Graduate School of Seoul National University
Interdisciplinary Program of
Computational Science and Technology

Chang-Hyun Park

Influences of ENSO and QBO on East Asian winter surface climate on sub-seasonal to seasonal timescale

ENSO와 QBO가 겨울철 동아시아 지상 기후에 미치는 계절내-계절 영향

지도 교수 손 석 우

이 논문을 이학박사 학위논문으로 제출함

2023년 5월

서울대학교 대학원
협동과정 계산과학전공
박 창 현

박창현의 이학박사 학위논문을 인준함

2023년 7월

위 원 장 김 정 훈 (인)

부위원장 손 석 우 (인)

위 원 예 상 욱 (인)

위 원 국 종 성 (인)

위 원 김 대 현 (인)

Influences of ENSO and QBO on East Asian winter surface climate on sub-seasonal to seasonal timescale

By

Chang-Hyun Park

Dissertation Submitted to the Faculty of the Graduate School of the Seoul National University in Partial Fulfillment of the Requirement for the Degree of Doctor of Philosophy

Degree Awarded:
August 2023

Advisory committee:

Professor Jung-Hoon Kim, Chair

Professor Seok-Woo Son, Advisor

Professor Sang-Wook Yeh

Professor Jong-Seong Kug

Professor Daehyun Kim

Abstract

El Niño–Southern Oscillation (ENSO) and Quasi–Biennial Oscillation (QBO) are the two leading modes in tropical regions. The ENSO is a large–scale interannual variability of the sea surface temperature and the associated atmospheric circulation changes in the equatorial Pacific Ocean, while the QBO is a dominant interannual variability of stratospheric equatorial zonal winds. These two tropical leading modes explain over 90% of the winter climate variability in tropical regions and have significant influences on mid–latitude surface climates through teleconnections. Therefore, it is important to understand the teleconnections to improve the prediction of the East Asian winter surface climate. However, previous studies have mainly focused on the seasonal mean effects during winter, resulting in a relative lack of research on a sub–seasonal time scale. Therefore, the present dissertation investigates the influences and mechanisms of the teleconnections on the sub–seasonal to seasonal time scales and provides three remarkable findings:

First, the teleconnections on East Asia vary within the winter season. Thus, the timing of their influences can be distinguished as ENSO in early winter vs. QBO in late winter. In early winter

(December), ENSO exerts a dominant influence on East Asian surface climate. The ENSO–East Asia teleconnections show a positive relationship between the ENSO and surface air temperature over the East Asia region, which is modulated by the atmospheric circulation variation over the Kuroshio region. In late winter (February–March), the influence of ENSO becomes weak, and that of QBO become relatively dominant. The QBO–East Asia teleconnections exhibit a negative relationship between the QBO and surface air temperature over the East Asia region, which is related to the meridional shift of the Asian–Pacific jet. The above results indicate that ENSO and QBO should be considered in sub–seasonal to seasonal prediction of East Asian winter surface climate. For instance, ENSO in early winter and QBO in late winter. In addition, it should be considered more actively to take into account the influence of the QBO in the East Asian climate prediction. Because the QBO–East Asia teleconnection has become more pronounced in the last 30 years, i.e., since the 1990.

Second, the key mechanisms of the teleconnections are identified. The ENSO–East Asia teleconnection is a result of a linear combination of poleward Rossby waves stemming from the tropical convection variations associated with ENSO, which enhances the atmospheric circulation variations over the Kuroshio

region. During El Niño years, the tropical convection activity over the Indian Ocean increases while that over the Maritime Continent decreases, leading to the poleward Rossby waves that reinforce the anti-cyclonic circulation anomalies over the Kuroshio region. As a result of the constructive interference, the ENSO-East Asia teleconnection is strengthened, resulting in a relatively warm anomaly over the East Asia. Since this constructive interference is primarily driven by tropical convection rather than mid-latitudes mean states, the strong tropical convections in December lead to the strongest ENSO-East Asia teleconnections in December. On the other hand, the QBO-East Asia teleconnections is mainly modulated by the meridional shift of the Asian-Pacific jet, which is induced by background and eddy changes in the subtropical stratosphere and upper troposphere. When the QBO is westerly phase, the westerly vertical wind shear and positive air temperature anomalies in the lower subtropical stratosphere region strengthen the wave propagation towards that region, inducing a southward shift of the Asian-Pacific jet. This leads to the development of cyclonic circulation anomalies in the North Pacific region, causing the cold advection into East Asia. The above results indicate that the second pathway of QBO associated with the subtropical jet among three pathways (i.e., polar, subtropical, tropical), plays the

most important role in East Asian winter surface climate. In addition, the geographical features of East Asia, located downstream of the Asian–Pacific jet and the Tibetan Plateau, reinforces the QBO downward influences.

Third, a more realistic representation of the key mechanisms of the teleconnections is required to improve the East Asian winter surface climate prediction. For instance, the state–of–the–art prediction systems are able to predict the spatial distribution of the ENSO–East Asia teleconnections, but have difficulties in predicting its sub–seasonal variations. In addition, the QBO–East Asia teleconnections are well predicted by operational prediction systems but poorly simulated by climate models. The possible reasons for the low predictability are the poor representation of sub–seasonal variations in tropical convection associated with ENSO and the poor representation of subtropical pathway of the QBO–East Asia teleconnections. Therefore, to improve the sub–seasonal to seasonal prediction of East Asian winter surface climate, it is important to enhance the modeling capabilities of tropical convection and its teleconnections to mid–latitudes in early winter, as well as the mean state changes associated with QBO in late winter.

Keyword : El Niño-Southern Oscillation, Quasi-Biennial Oscillation, Teleconnection, Downward Coupling, Sub-seasonal to Seasonal Prediction

Student Number : 2013-23010

Table of Contents

List of Tables

List of Figures

level. The red contour indicates the intraseasonal positive anomaly by subtracting the seasonal-mean anomaly from the pentad anomaly. The blue contour also indicates the intraseasonal negative anomaly. The contour interval is 1 $\mathrm{W\,m^{-2}}$ starting from 1 $\mathrm{W\,m^{-2}}$ in (a), and 0.3 $\mathrm{mm\,day^{-1}}$ starting from 0.3 $\mathrm{mm\,day^{-1}}$ in (b).

Figure 2.12. (a) Temporal evolutions of outgoing longwave radiation (OLR) anomalies over the IO in each El Niño year (gray), their average value (black), and the mature stage of the IO convection based on the average value (vertical line). (b) Mature stages of IO convections in each El Niño year. (c) The OLR anomaly map at the mature stage of each El Niño year, defined in b. The longitudinal ranges of the IO domain in (a) are defined as 70°–90°E in 4),12) cases and 40°–60°E in 6),7),14) cases to pick up the enhanced convection (blue shading in c).

Figure 2.13. (a-f) Number of MJO events in El Niño years from phases 1 to 6 (from IO to MC and western Pacific). The outline bar indicates all the MJO cases and green filled bar indicates strong MJO cases (amplitude $\geq$ 1.5). Star denotes the period of the highest MJO frequency for each phase (from phase 1 to 6) is observed. The MJO phases are defined by using the OLR based MJO index (i.e., OMI index).

Figure 2.14. 2-pentad lagged partial regression of a yearly time series of Z500 anomaly onto the yearly time series of (a) IO, (b) MC, (c) CP precipitation anomalies from the convection's maximum period. The dotted marks represent statistically significant values at the 95% confidence level based on a Student's t-test. The contour interval is 2 $\mathrm{gpm\,(mm\,day^{-1})^{-1}}$.

Figure 2.15. (a, c) Observed ENSO-related Z500 anomalies at (a) its maximum and (c) minimum periods. (b, d) Same as (a, c) but for the reconstructed Z500 based on the linear combination of the partial regression coefficients in Fig. 2.14.

Figure 3.12. (a) Regression between the Korean SAT and the QBO. (b) Lagged correlation between the SAT over the Korean Peninsula and the QBO. The white circle indicates the statistically significant coefficient at the 95% confidence level. Units of the regression coefficients in (a) are converted into Kelvin by multiplying the standard deviation of the QBO. The QBO lag month at y-axis in (b) denotes the QBO lag with respect to the SAT over the Korean Peninsula. For instance, MAR-1 lag month (white circle in (b)) indicates the correlation between the March SAT over the Korean Peninsula and the February QBO.

Figure 3.13. (a) Regression between the SAT over the Korean Peninsula and the QBO in March. (b) Same as (a) but for the February QBO. (c) The Granger causality between the SAT over the Korean Peninsula in March and the QBO in February. Blue colored circles indicate the statistically significant regressions at the 95% confidence level. Units of the regression coefficients are converted into Kelvin by multiplying the standard deviation of the QBO.

Figure 3.14. Same as Fig. 3.13c but for the partial Granger causality: (a) the QBO Granger-causes the SAT over the Korean Peninsula when conditioned the ENSO's effect and (b) ENSO Granger-causes the SAT over the Korean Peninsula when conditioned the QBO's effect. Units of the regression coefficients are converted into Kelvin by multiplying the standard deviation of the (a) QBO and (b) ENSO.

Figure 3.15. (a) The lead-lag correlation coefficients between the two-month running averaged QBO wind at each pressure level and the FM WNP SAT anomaly. The vertical profile at lag 0 is separately shown on the right-hand side. (b) The latitude-height section of the FM-mean zonal wind anomaly averaged over the Asian-Pacific jet (APJ) core (120°–150°E) regressed onto the FM-mean QBO index (shading; $\mathrm{m\,s^{-1}}$). The filled dots in (a) and cross-hatched area in (b) denote the statistically significant values at the 95% confidence level. The thick black contour in (b) indicates the climatological

arrows denote the statistically significant regressions at the 95% confidence level based on Student's *t*-test. Units of the regression coefficients are converted into Pa and $\mathrm{m\,s^{-1}}$. by multiplying the standard deviation of the QBO, respectively.

Figure 3.21. (a) 21-year running correlation between the FM-mean WNP SAT anomaly and the FM-mean QBO index, where the x-axis indicates the middle year of the 21-year moving window. Both JRA-55 (red) and JRA-55C (yellow) are used. (b) same as (a) but for the FM-mean APJ shift index and the FM-mean QBO index. The filled dots in (a,b) denote the values which are statistically significant at the 95% confidence level. The dotted lines in (a,b) denote the correlation coefficients over the whole analysis period.

Figure 3.22. Leading hypothesis of the QBO downward coupling suggested in previous studies. (a) schematic diagram and (b) 3D simulation result indicating the role of eddies for the QBO downward coupling. The black contour and color shading in (a) denote the zonal-mean zonal wind and temperature anomalies associated to the WQBO phase. Black thick arrows denote the associated secondary circulations. Red arrows and circles in (a,b) denote the extended QBO downward coupling due to the presence of the eddies in 3D simulations.

Figure 3.23. (a, b) The latitude-height section of the zonal-mean zonal wind (U-wind) response difference between the (a) W-EQBO in observation and (b) WQBO simulation and CTL simulations (WQBO-CTL) (shading; $\mathrm{m\,s^{-1}}$). The thick black contour in (a, b) indicates the climatological APJ. The cross-hatched area in (a) denote the statistically significant values at the 95% confidence level, note that it is same to Fig. 3.15(b) for a direct comparison.

Figure 3.24. The response of the (a, b) U-wind (contour) and EMFC (shading) in (a) CTL and (b) WQBO (c, e) Same as (a, b) but for the at 250hPa where the jet core level in (c) CTL and (e) WQBO. (d, f) The budget analysis of the EMFC in (d) CTL and (f) WQBO. The

vertical black and red lines represent the maximum latitude of the jet and EMFC, respectively. HF, LF, MF denote the high-frequency, low frequency, and mixed frequency components, respectively.

Figure 3.25. Time evolution of WQBO-CTL response of U-wind (a) at 250 hPa and (b) vertical profile of 2-day mean. The contour and vertical line represent the Jet core in CTL. Shading represents the WQBO response. The result is ensemble mean of 100 transient experiments.

Figure 3.26. 2-day mean time evolution of WQBO-CTL response of refractive index (shading) and E-P flux (vector). The vertical line represents the Jet core in CTL. The result is ensemble mean of 100 transient experiments. The zonal-mean quasigeostrophic refractive index is calculated based on the zonal wavenumber: k = 7, zonal phase speed: c = 0m/s.

Figure 3.27. 2-day mean time evolution of WQBO-CTL response of Eddy momentum flux (EMF; contour) and its convergence (EMFC; shading). The vertical line represents the Jet core in CTL. The result is ensemble mean of 100 transient experiments.

Figure 3.28. WQBO-CTL response of (a) refractive index (shading) and meridional gradient of potential vorticity (PV gradient; contour), and (b) U-wind (contour) and temperature (shading) at 1-2-day integration. The result is ensemble mean of 100 transient experiments.

Figure 3.29. Idealized Gaussian-shaped Tibetan Plateau (TB). (a) its spatial distribution, (b) vertical profile, and (c) a variety of height of the TB for the sensitivity test.

Figure 3.30. WQBO-CTL response of U-wind in (a) observation, (b) Notopo experiment, and (c) TB_4km. (lower panels) Same as upper panels but for the spatial distribution at 250hPa. The contour and shading represent the climatological mean jet and WQBO response, respectively. Red thick contour in (lower panel of c) indicates the TB_4km Gaussian-shaped topography.

1. Introduction

1.1. ENSO teleconnections

The El Niño-Southern Oscillation (ENSO) is an ocean-atmosphere coupled large-scale interannual variability, which is characterized by anomalous sea surface temperature (SST) warming, corresponding to the eastward shift of atmospheric deep convection in the equatorial Pacific. Such conditions excite the stationary atmospheric waves referred to as the Rossby wave train (Bjerknes, 1969; Horel and Wallace, 1981; Wallace and Gutzler, 1981), similar to the Pacific North American (PNA) teleconnection patterns (Horel and Wallace, 1981). The resultant anomalous circulations induce the extreme events on the global climate (Ropelewski and Halpert, 1986).

It results in extreme weather events such as heavy rainfall, drought, and temperature extremes over highly populated regions, including East Asia and western North America (e.g., Ropelewski and Halpert, 1986; Wang et al., 2000; Glantz, 2001; Nicholls et al., 2005; Arblaster and Alexander, 2012). For instance, the El Niño of 1997/98 induces 22,000 fatalities and US $36 billion in economic losses (Sponberg, 1999; McPhaden et al. 2006). In order to reduce its socio-economic damage, an improved understanding and a prediction of ENSO teleconnection are necessary.

On East Asia, the ENSO can modulate the winter surface climate via these atmospheric circulation change. The strengthened trade winds, caused by the anomalous SST warming, induce cold SST anomaly over the tropical western Pacific through the enhancement of evaporation. As a part of the Rossby wave response to the cold SST anomaly, the anticyclonic circulation anomaly develops over Philippine Sea region, effectively influencing the East Asian surface climate (Wang et al., 2000). This so-called 'Philippine Sea anticyclonic circulation anomaly' continuously develops throughout the winter season via a positive air-sea feedback (Wang et al., 2000; Xie et al., 2009).

In addition to the atmospheric circulation change in the lower troposphere, the anticyclonic circulation anomaly over Philippine Sea also induce the upper cyclone circulation over the Philippine Sea, resulting in an anticyclonic circulation anomaly over the Kuroshio region (Wang et al., 2000). This so-called 'Kuroshio anticyclonic circulation anomaly' is more responsible for the northern part of the East Asian surface climate than the Philippine Sea anticyclonic circulation anomaly (Son et al., 2014; Kim et al., 2018).

These two El Niño-related anticyclonic circulation anomalies act as a bridge between the tropical anomalous SST warming and East Asian surface climate variability. Thus, the El Niño and the East Asia climate variability have a statistically significant relationship during the winter

season (Kang, 1998).

Since El Niño usually reaches the maximum intensity in the boreal winter and then it decays in late winter and spring (An and Wang, 2001), the El Niño-related atmospheric anomalies are expected to be maintained during the entire winter season. However, previous studies show sub-seasonal variability of ENSO teleconnections in the Pacific basin (Bladé et al., 2008; Jong et al., 2016) In East Asia, the ENSO teleconnection weakens in January, which cannot be explained by the sub-seasonal variation of the central Pacific SST (Kim et al., 2018). Thus, a more detailed analysis is needed to reveal the sub-seasonal variability of the ENSO-East Asia teleconnection.

In addition to the central Pacific (CP), the ENSO-related convection and circulation changes lead to the atmospheric forcing in the Indian Ocean (IO) and Maritime Continent (MC), which can modulate the ENSO teleconnections (Zhang et al., 2005; Annamalai et al., 2007; Seo and Son, 2012). For instance, the suppressed convection in the MC can leads to the ENSO-East Asia teleconnections. Moreover, the enhanced convection in the IO makes the negative PNA-like pattern over mid-latitudes (Moon et al., 2011; Hoell et al., 2014; Seo and Lee, 2017). However, most previous studies have primarily focused on the seasonal-mean effects of the ENSO-related tropical convection anomalies.

This dissertation examines the nature of the sub-seasonal

modulation of ENSO-East Asia teleconnections and suggest the role of ENSO-related tropical convection anomalies in the MC and IO as a possible modulator of the ENSO-East Asia teleconnections in early winter.

1.2. QBO downward coupling

The quasi-biennial oscillation (QBO) is a dominant interannual variability of stratospheric equatorial zonal winds, characterized by an oscillation between the westerly and easterly winds with period of 28 months (e.g., Baldwin et al., 2001). This phenomenon has a distinct effect on the mid-latitude climate variability (Baldwin et al., 2001; Gray et al., 2018).

The QBO-induced meridional circulation and vertical shear anomaly can affect the propagation of mid-latitude planetary waves. When the QBO phase is easterly, planetary wave from mid-latitudes toward the equator are directed toward the polar vortex, weakening the vortex (Holton and Tan, 1980). The resultant weakened polar vortex changes the tropospheric circulation and thus the surface climate variability as a negative Arctic Oscillation (AO) pattern (Thompson et al., 2002).

The QBO-related atmospheric instability affects tropical convective activity (Son et al., 2017), including Madden-Julian Oscillation (MJO; Madden and Julian, 1971). When the QBO is an easterly phase, an

easterly vertical shear is driven in the lower stratosphere. To balance the thermal wind relationship, anomalous upward motion and cold temperature occur in the equator. In the subtropics, anomalous downward motion and warm anomaly form due to the secondary circulation. As a result, the increased atmospheric instability in the equators amplifies not only the tropical convective activity (Collimore et al., 2003) but also the MJO-induced teleconnection to mid-latitude climate variability (Hood et al., 2020).

The QBO also influences the intensity and position of subtropical jets (Ruti et al., 2006). The returning meridional flow near the tropopause in the subtropics generates a weak easterly in the subtropical tropopause through the Coriolis force. The easterly wind anomaly can be extended into the lower troposphere in the form of a horseshoe, in the presence of the transient eddy feedback (Garfinkel and Hartmann, 2011a,b). As a result, the vertical shear around the jet is changed, inducing the meridional displacement of the jet (Simpson et al., 2009, 2010). As this downward arching zonal wind anomaly extends to the mid-to-lower troposphere, it can induce meridional displacement of the subtropical jet and thus influence the Northern Hemisphere surface climate (Gray et al., 2018, Haynes et al., 2021). Since the fluctuations of strength and position of the jet have tightly connected to the East Asian surface climate variability (Luo and Zhang, 2015), the QBO can affect the

East Asian surface climate variability. The above results indicate that QBO may have a strong relationship with East Asian surface air temperature (SAT).

However, previous studies mainly focused on the impacts of the QBO on the Northern Hemisphere, explained by the relationship between the equator and high latitudes known as the Holton-Tan effect (Holton and Tan, 1980, 1982; Baldwin et al., 2001; Chen and Li, 2007). This impact appears mainly on the high latitude regions of the North Atlantic, Europe, and Eurasia, which are downstream regions of the AO's effect (Marshall and Scaife., 2009 Scaife et al., 2014). In addition, a more delicate analysis reveals that the regional QBO impacts, especially on the East Asia, differs from the AO signal associated with QBO-polar vortex downward coupling (Ma et al., 2021).

This dissertation revisits the QBO teleconnection on the sub-seasonal time scale focusing on the East Asia region and investigates a possible key mechanism of QBO-East Asia teleconnection. In addition, the prediction skill and model representation of the QBO-East Asia teleconnections is also evaluated.

1.3. Motivations and aims of the Thesis

As shown in the previous section, during the last decade, the climate community has made remarkable progress in understanding ENSO and QBO's influence on the mid-latitude climate variability. However, it is further needed to revisit the influences of the ENSO and QBO on the East Asian SAT in detail.

While the seasonal-mean ENSO-East Asia teleconnections are well documented, their impacts and predictability on the sub-seasonal time scale remain to be explored. Son et al. (2014) showed that a possibility for a sub-seasonal variability of the ENSO teleconnections. The relationship can be also different depending on the type or season of El Niño (Kug et al., 2010; Yeh et al., 2014) and even the analysis method (McGraw and Barnes, 2018). Such unexpected events on a sub-seasonal time scale can induce socioeconomic damages because they could not be detected in a seasonal-mean time scale analysis and prediction. It indicates a more delicate study about the mechanisms and prediction skill of the ENSO-East Asia teleconnections is needed.

In addition to the ENSO teleconnection, the QBO-East Asia teleconnection is needed to revisit in detail. Since the so-called 'Holton-Tan effect' has been highlighted over decades, the impact and dynamics of the QBO impact has been mainly focused on the Northern Eurasia and

North America region rather East Asia. However, the Holton-Tan effect may be not suitable for the East Asian surface climate because the it is in the marginal region of the Eurasia Continent (see Thompson et al., 2002). Garfinkel and Hartmann (2011a) reported that the QBO teleconnection is stronger in Pacific region than Atlantic region in subtropics where East Asia is located. The associated mechanism is still needed to revisit.

Therefore, the main objective of this dissertation is to improve our understanding of the sub-seasonal and seasonal-mean impacts of ENSO and QBO on East Asian surface climate in detail. To achieve this objective, we are supposed to answer these questions as follows:

What are the relative effects of the ENSO and QBO on East Asian SAT on a sub-seasonal time scale?

What is the possible mechanism, and do state-of-the-art ensemble prediction systems predict the impacts and mechanisms well?

If not, how can we improve it?

To do this, this dissertation is organized as follows. The relationship between the ENSO and East Asian SAT is investigated by using a variety of analysis methods (i.e., composite, correlation, lead-lag regression, and Granger causality test) and time scale (i.e., seasonal-

mean, pentad-mean) in Section 2. Since the ENSO and QBO have a long memory (for instance, the QBO has high autocorrelation coefficient; r = 0.92 at a one-month lag), the relationship is should be investigated by considering the memory. According to McGraw and Barnes (2018), present study uses a more delicate analysis method such as Granger causality and Partial Granger causality tests.

The relationship between the QBO and East Asian SAT is also examined in the same way in Section 3. Summary and Discussion are provided in Section 4. The contents in Section 2 are from Park et al. (2018) and Park et al. (2023), and the contents in Sections 3 and 4 are from Park and Son (2022) and Park et al. (2022).

2. Sub-seasonal variability of ENSO teleconnection

2.1. Data and Methods

2.1.1. Observation and hindcasts

The main datasets used are pentad-mean atmospheric variables obtained from the fifth generation of ECMWF atmospheric reanalysis of the global climate (ERA5; Hersbach et al., 2020), including SAT, geopotential height (Z), horizontal winds (U,V), sea level pressure (SLP), specific humidity, omega, and column relative humidity (CRH) calculated using zonal winds, air temperature, and specific humidity from the surface (1000 hPa) to the top (100 hPa) of the troposphere. The Outgoing Longwave Radiation (OLR) data is obtained from NOAA Interpolated OLR product (Liebmann and Smith, 1996) during 1979/1980–2018/2019 (40 years). The precipitation data is obtained from NOAA CPC Merged Analysis of Precipitation products (Xie and Arkin, 1997) during 1980–2016. We construct 24 pentads per winter (November to February). For instance, the 7th pentad consists of five days from December 2nd to 6th. Anomalies are defined by removing the climatological mean at each pentad and the long-term linear trend for 40 years.

Furthermore, to enhance the confidence of the above results, the

in-situ measurements from the meteorological administrations of Korea (KMA) are also used for the period as 59-year from 1958 to 2016. The 21-day moving average daily temperature and precipitation observation data of the Automatic Synoptic Observing System (ASOS) of the Korea Meteorological Administration were used, and the average of 9 observation points was set as a representative value of the Korean Peninsula. The nine observation points used were Gangneung (105), Seoul (108), Chupungryeong (135), Gwangju (156), Busan (159), Incheon (112), Pohang (138), Daegu (143), and Jeonju (146) and the number in parentheses means the station number.

To ascertain the ability to predict ENSO teleconnection in a climate prediction system, we examine the retrospective predictions (or hindcasts) from the four state-of-the-art ensemble prediction systems, including the European community Earth-System Model (EC-Earth3; Döscher et al., 2021), the Hadley Centre Global Environment Model version 3 (HadGEM3-GC31-MM; Andrews et al., 2020), the sixth version of the Model for Interdisciplinary Research on Climate (MIROC6; Tatebe et al., 2019), and a higher-resolution version of the Max Planck Institute for Meteorology Earth System Model (MPI-ESM1.2-HR; Müller et al., 2018). The datasets follow the guidance of the Decadal Climate Prediction Project contributed to the Coupled Model Intercomparison Project 6 (Boer et al., 2016). A total of 40 ensemble members, initialized every 1

November from 1979 to 2019 with 10 ensemble members of each model, are used in this study. The individual ensemble members are interpolated to a uniform 2.5° × 2.5° grid. To remove the model drift, the forecast lead time-dependent model bias is corrected for individual ensemble members before the analysis. For a direct comparison to ERA5, the daily atmospheric variables are converted from daily into pentad resolutions except for the SST (i.e. monthly-mean modeled SST is used). The multi-model ensemble (MME) is then constructed by averaging 40 ensemble members with an equal weighting.

2.1.2. Correlation, regression, and composite analysis

All the results in this section consist of simple correlation, regression, and composite analysis. To estimate the linear relationship between ENSO and East Asian SAT, Pearson correlation coefficient (R_t) is used. The equation is as follows (Eq. 1).

$$R_t = \frac{\sum_{ii=1}^{n}(SAT_{t,ii}-\overline{SAT}_t)(ENSO_{t,ii}-\overline{ENSO}_t)}{\sqrt{\sum_{ii=1}^{n}(SAT_{t,ii}-\overline{SAT}_t)^2}\sqrt{\sum_{ii=1}^{n}(ENSO_{t,ii}-\overline{ENSO}_t)^2}} \quad (1)$$

where t is the month and ii is the year, n is the total number of years. The overbar indicates the climatological mean.

As the ENSO-related SST anomalies tend to persist throughout the boreal winter, the regression analysis is conducted with the pentad-mean atmospheric variables onto the seasonal-mean Niño 3.4 index (i.e.,

NDJF- or DJF-mean) as Eq. 2:

$$SAT_t = a_0 + a_t\ Niño3.4_t + e_t \quad (2)$$

where a_0 is the intercept, a_t is the regression coefficient, and e_t is the residual of the regression. Here Niño3.4 indicates that the seasonal-mean value.

In addition, the association between ENSO and mid-latitude circulation anomalies is evaluated by regressing atmospheric variables against the Niño 3.4 index or the three tropical precipitation indices (central Pacific (CP), Indian Ocean (IO), and Maritime Continent (MC)). These regional precipitation indices are defined by averaging pentad precipitation anomalies over the CP (160°E–120°W, 10°S–10°N) and IO domains (50°–70°E, 10°S–10°N) and MC (90–150°E, 10°S–10°N), respectively. Here, the IO precipitation corresponds to the western-IO precipitation, reported by Abid et al. (2021), whereas the CP domain is extended by 5° to the north and south from the domain used in Kim et al. (2018). To separate the CP, IO, and MC impacts on mid-latitude atmospheric circulation, a partial regression analysis is applied after removing their relative signals. To determine the IO-convection-induced teleconnections, a linear regression is conducted with the Z500 anomaly filtering out the CP- and MC-convection-related anomaly against the IO precipitation anomaly. Notably, the overall results are not sensitive to slight changes in the indices domains.

For a composite analysis, we use the National Oceanic and Atmospheric Administration (NOAA)'s operational El Niño definition, which is based on the Oceanic Niño Index (ONI). The ONI is calculated by a three-month running mean SST anomaly in the Niño 3.4 region (170°–120°W, 5°S–5°N; Niño3.4 SSTA) from Extended Reconstructed SST data (ERSSTv5; Huang et al., 2017). The El Niño (La Niña) event is defined when the three-month running mean Niño3.4 SSTA exceeds +0.5K (−0.5K) for at least five consecutive months. Any winter not meeting the El Niño or La Niña criteria is defined as a Neutral winter. As a result, 14 El Niño and 14 La Niña years were selected during the last 40 years (1979/1980–2018/2019) summarized in Table 2.1.

Table 2.1. List of selected 14 El Niño and 14 La Niña years for the composite analysis. Here, El Niño and La Niña years are defined when the three-month running mean Niño 3.4 index exceeds +0.5K and −0.5K for at least five consecutive months, respectively.

Events	# of years	List of years
El Niño	14	1979/1980, 1982/1983, 1986/1987, 1987/1988, 1991/1992, 1994/1995, 1997/1998, 2002/2003, 2004/2005, 2006/2007, 2009/2010, 2014/2015, 2015/2016, 2018/2019
La Niña	14	1983/1984, 1984/1985, 1988/1989, 1995/1996, 1998/1999, 1999/2000, 2000/2001, 2005/2006, 2007/2008, 2008/2009, 2010/2011, 2011/2012, 2016/2017, 2017/2018

The statistical significances of the correlation and composite are estimated based on a two-tailed Student's *t*-test. For the composite analysis, a bootstrap method is further used to cover the shortage of the number of observations. During the winter (November to February), the pentad anomalies of 40 years are randomly resampled 1,000 times to produce an estimated distribution. If the composite anomaly of El Niño years is larger than the ranked value from the estimated distribution at a 95 % significance level, the composite anomaly is deemed to be statistically significant.

2.1.3. Causality test

Granger causality test (Granger, 1969) is further conducted to account into the high memory of the ENSO in the causal relationship analysis. The key point is to determine whether the inclusion of ENSO information (Eq. 4) is helpful to the prediction of the SAT than the case using only SAT itself information (Eq. 3) or not. For the comparison, the two time-lagged regressions are constructed as in Barnes and Simpson (2017):

$$SAT_t = a_0 + \sum_{i=1}^{M} a_i \, SAT_{t-i} + e_{1t} \quad (3)$$

$$SAT_t = b_0 + \sum_{i=1}^{M} b_i \, SAT_{t-i} + \sum_{j=1}^{N} c_j ENSO_{t-j} + e_{2t} \quad (4)$$

where the subscript t denotes each month of the year, while i

and j denote the monthly time lag from t. The coefficients a_0 and b_0 are the intercepts, a_i, b_i, and c_j are the regression coefficients, and e_{1t} and e_{2t} are the residuals. M and N are the number of optimal time lags for the SAT and ENSO index, respectively.

Equation (3) represents a lagged auto-regression to estimate SAT_t with the prior values of SAT_{t-i}. Equation (4) estimates SAT_t by considering not only the prior values of SAT_{t-i} but also the prior values of $ENSO_{t-j}$. Not surprisingly, their results are sensitive to the choice of the time lag, M and N. In this study, M and N are chosen to minimize the final prediction error (FPE) (Hsiao, 1981). Here, the FPEs of Equations (3) and (4) are determined by $\frac{O+M+1}{O-M-1} \times \frac{SSE_1}{O}$ and $\frac{O+M+N+1}{O-M-N-1} \times \frac{SSE_2}{O}$, respectively (Hsiao, 1981; Amiri and Linden, 2016).

$$\text{Optimal lag} = \text{argmin FPE}_{\text{restricted}} = \text{argmin } \frac{O+M+1}{O-M-1} \times \frac{SSE_1}{O} \quad (5)$$

$$\text{Optimal lag} = \text{argmin FPE}_{\text{unrestricted}} = \text{argmin } \frac{O+M+N+1}{O-M-N-1} \times \frac{SSE_2}{O} \quad (6)$$

The SSE_1 and SSE_2 denote the sum of squared errors of each regression, and O is the number of years (O = 40). The causal relationship is identified by estimating the usefulness of the prior values of the ENSO. When at least one value of c_j is statistically significant according to a two-tailed Student's t-test and all values of c_j collectively improve the variance explained by the regression according to an F-test, it is considered that the ENSO causes the SAT anomaly. Here, F statistics are defined as follows:

$$\text{F statistics} = \frac{(SSE_1 - SSE_2)/N}{SSE_2/(O-P)} \quad (7)$$

where P is the total number of parameters estimated from Equation (4).

2.1.4. Prediction skill

The MME prediction skill is assessed with the anomaly correlation coefficient (ACC), as shown below:

$$ACC_i = \frac{\sum_{j=1}^{j=40}(MME_{i,j} - \overline{MME_i})(OBS_{i,j} - \overline{OBS_i})}{\sqrt{\sum_{j=1}^{j=40}(MME_{i,j} - \overline{MME_i})^2}\sqrt{\sum_{j=1}^{j=40}(OBS_{i,j} - \overline{OBS_i})^2}} \quad (8)$$

where i and j represent the forecast lead-time and year, respectively. The $MME_{i,j}$ and $OBS_{i,j}$ denote the MME and observation at the ith forecast lead-time and jth year, respectively. The overbar indicates the climatological mean over 40 years.

For statistical significance of ACC is calculated based on a nonparametric bootstrap method (Goddard et al., 2013). At each forecast lead time, the ACC is randomly calculated with a replacement for 1,000 times to produce an estimated distribution. The p-value is obtained from the ratio of negative value from the estimated distribution based on the one-tailed test of the hypothesis that the ACC is greater than 0. If the p-value is smaller than 0.05, the ACC is deemed to be statistically significant at the 95 % significance level.

2.1.5. Linear baroclinic experiments

Statistically significant relationship in early winter. The relative importance of CP, MC, and IO convection on ENSO-East Asia teleconnections is tested by conducting linear baroclinic model experiments. This model solves primitive equations linearized about a given basic state at T42 horizontal resolution with 20 sigma levels (Watanabe and Kimoto, 2000). The horizontal diffusion is set to biharmonic diffusion with an e-folding time scale of 2 h for the largest wavenumber. The Newtonian damping is also utilized at the lowest three levels and the topmost two levels with a time scale of 0.5 days, and at the mid-levels with a time scale of 20 days (Watanabe and Kimoto, 2000).

This model is forced by idealized tropical diabatic heating under the El Niño January background state. The diabatic heating forcing is set to have a latitudinal width of 15°, with a gamma vertical distribution (Fig. 2.1). The maximum heating of 3 K day-1 is placed at the 0.45 sigma level. Two regional heating–one over the IO and the other over the CP–are considered in this study, as shown in Fig. 2.1. A steady-state atmospheric response to each forcing is obtained by investigating the Z500 anomaly field at 20-day. The quality of the results remains the same even when the magnitude and level of tropical heating slightly vary.

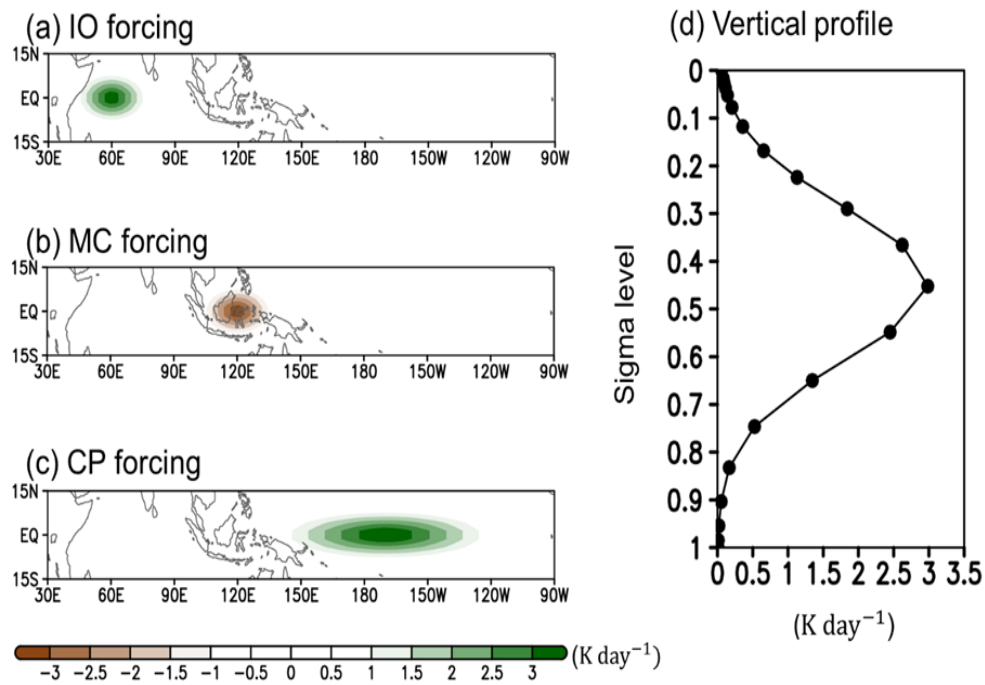

Figure 2.1. Details of linear baroclinic experiments. (a-c) Spatial distribution of idealized heat forcing over the (a) IO, (b) MC (b) CP at 0.45 sigma level. (d) Vertical profile of the heat forcings at 60°E, 120°E, and 160°W where the maximum location of the idealized forcing.

2.2. Impacts and causality

2.2.1. Positive relationship in early winter

On a seasonal time-scale, the warm anomalies are robust over East Asia and western North America, attributable to El Niño-induced atmospheric circulation anomalies in the boreal winter (two boxes in Fig. 2.2a; Wallace and Gutzler, 1981; Ropelewski and Halpert, 1986; Wang et al., 2000). This SAT anomaly pattern has been widely known as the canonical ENSO teleconnections. However, it is not stationary on the sub-seasonal time scale (Son et al., 2014; Kim et al., 2017; Geng et al., 2017). Statistically significant warming appears in December (filled bars in Fig. 2.2b,c).

For emphasizing this early winter of ENSO teleconnections, we defined the peak period, which consists of December 11th to 31st according to the sub-seasonal variation of SAT anomalies, i.e., the consecutive 20 days around the warmest pentad in both East Asia and western North America. The suppression period, which consists of January 1st to 20th, is also defined in the same way. All 14 El Niño winters show this robust warming in early winter, which disappears in early January (Fig. 2.3). Although not presented here, the results are not sensitive to the analysis period and data.

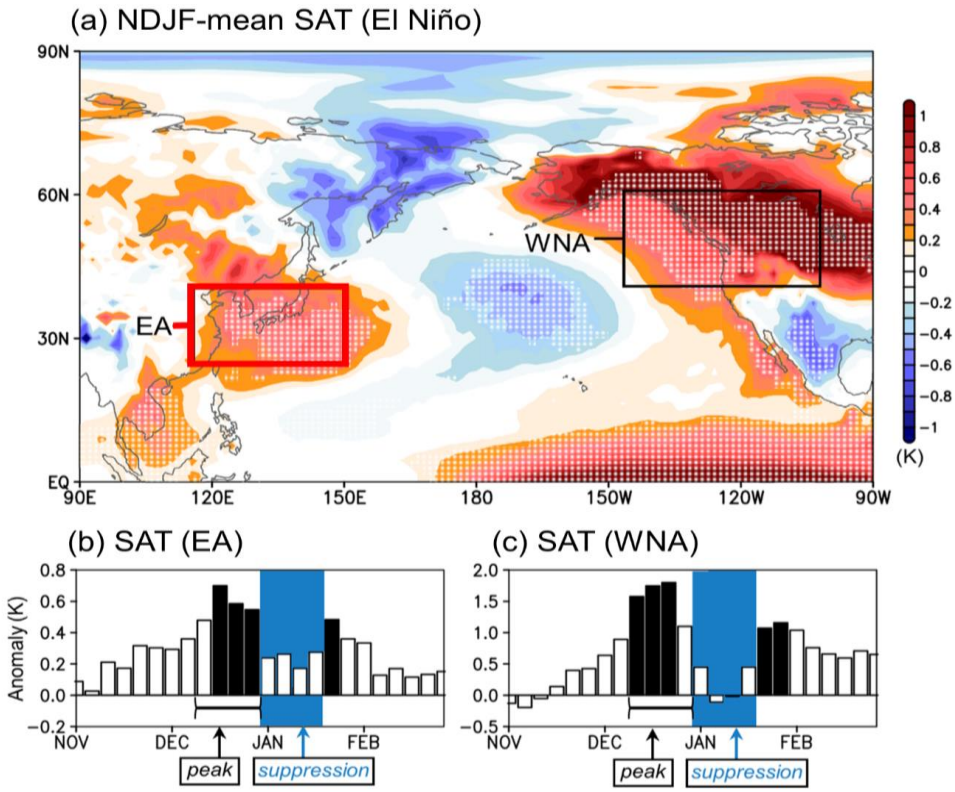

Figure 2.2. (a) November-February mean surface air temperature (SAT) anomaly during El Niño years. (b,c) Temporal evolution of pentad mean SAT anomalies averaged over (b) East Asia (EA; 115–150°E, 25–40°N) and (c) western North America (WNA; 140–100°W, 40–60°N). The dotted area in (a) and filled bars in (b,c) indicate statistically significant values at the 95 % confidence level based on the bootstrap method. The 'peak' and 'suppression' of ENSO teleconnection are defined as the periods that the consecutive 20 days around the warmest and coolest pentad are simultaneously observed in East Asia and WNA.

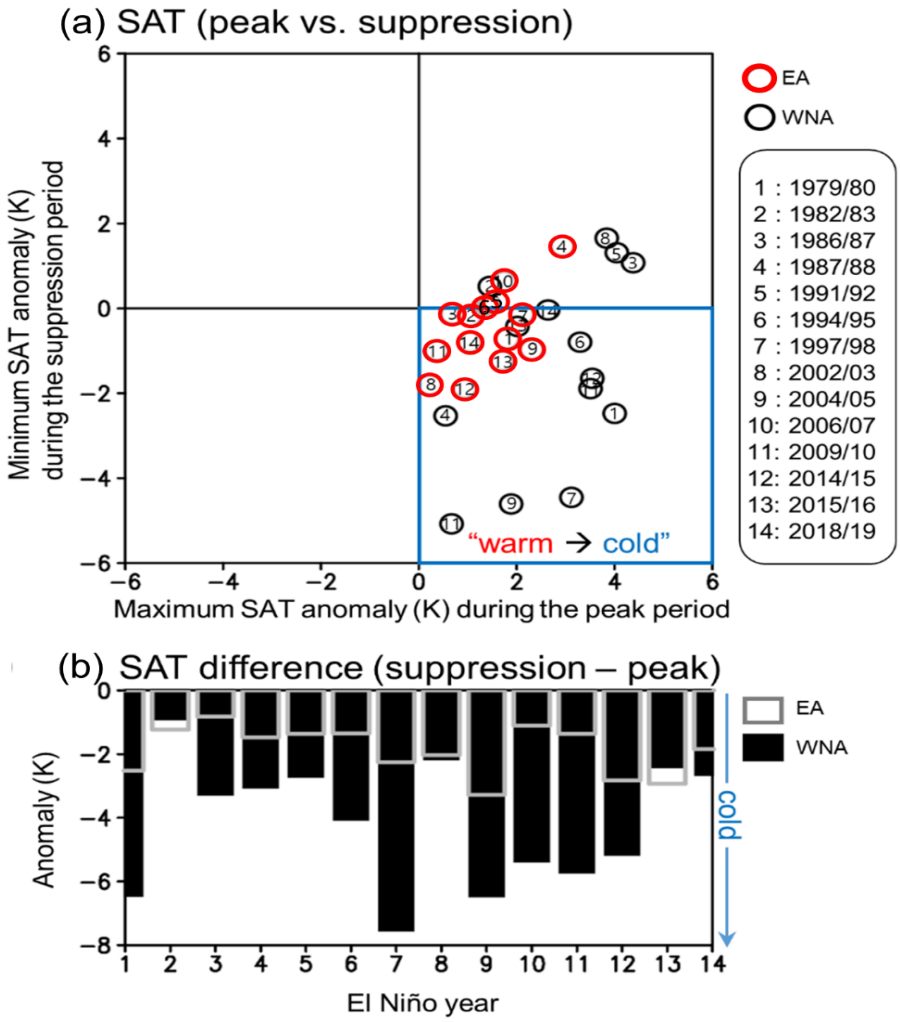

Figure 2.3. (a) Scatter plot of the maximum SAT anomaly during the peak (x-axis) and minimum SAT anomaly during suppression periods (y-axis) over the East Asia (red) and WNA (black). (b) SAT anomaly difference between the suppression and peak periods in each El Niño winter. All the maximum and minimum appear within December 12th to 31st and December 22nd to January 20th except for the early peak and suppression winters (2009/10, 2014/15). The maximum appears in November 22nd to December 1st and the minimum appears in December 7th to 21st in those winters.

Similar result is also seen in In-situ measurements from the KMA (Fig. 2.4). The correlation between the winter season (NDJ) ENSO index and the daily-mean SAT over the Korean Peninsula shows significant relationship during the early winter (red colored bars in Fig. 2.4a), which is consistent with the seasonal-mean relationship.

The Granger causality test reconfirms this sub-seasonal variation of the linear relationship. The auto-regression coefficient of the SAT can explain the SAT variability only confined to the early winter and late winter (a_1; cyan line in Fig. 2.4b), consistent with the auto-regression coefficient of the SAT in Equation (3) (c_1; blue line in Fig. 2.4c). However, the regression coefficient of ENSO (b_1; red line in Fig. 2.4c), corresponding to Equation (4), can account for the SAT variation in the December. This result supports that the relationship between the ENSO and the East Asian SAT is robust in early winter.

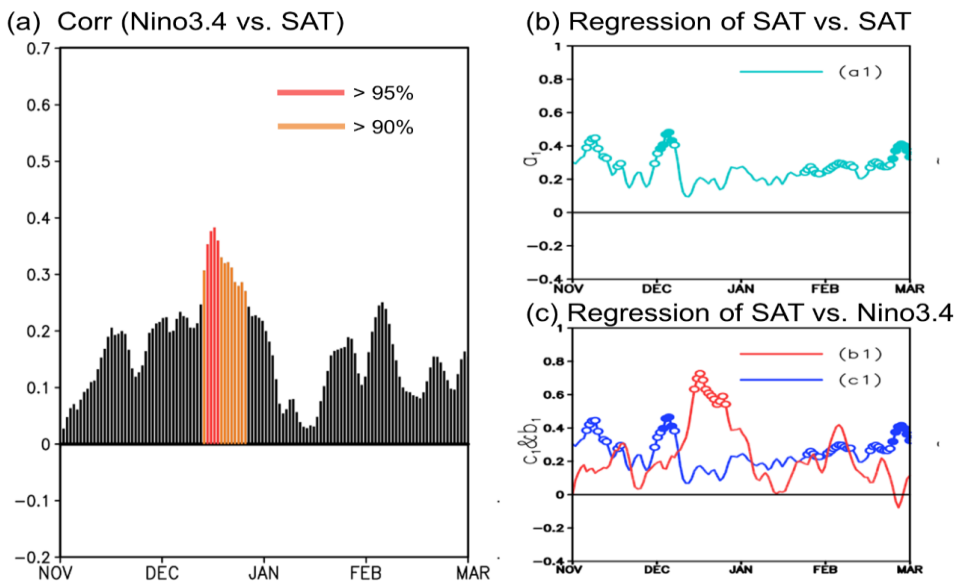

Figure 2.4. (a) Correlation coefficient of the NDJ-mean Niño3.4 and the SAT over the Korean Peninsula. (b) Auto-regression coefficients of Eq. (3) (a_1; cyan line). (c) Regression coefficients of Eq. (4) for the SAT (c_1; blue line) and the ENSO (b_1; red line). The orange (red) colored filled bar and open (closed) circles indicate statistically significant values at the 95 % (99%) confidence level based on a student's t-test.

2.2.2. ENSO-related atmospheric circulation change

Figure 2.5a shows the ENSO-related NDJF SAT anomalies in the East Asia. As seen, a warm anomaly is clearly discerned over the East Asia including coast line of China, Korean Peninsula, and Japan (box in Fig. 2.5a). This warm anomaly is strongly related with the Kuroshio (KU) anti-cyclonic circulation anomaly (boxed in Fig. 2.5b). The KU circulation anomaly primarily determines the spatial distribution and intensity of the SAT anomaly over the East Asia through anomalous temperature advection (Kim et al., 2018).

As ENSO SST anomalies exhibits weak sub-seasonal variability, it is reasonable to suggest that ENSO teleconnections can persist throughout winter. However, the ENSO teleconnections exhibit clear fluctuations on a sub-seasonal timescale (Jong et al., 2016; Kim et al., 2018). Figure 2.5c displays the sub-seasonal evolution of ENSO teleconnections over the East Asia. The pentad East Asian SAT and KU Z500 time series is further regressed against the seasonal-mean Niño 3.4 index (Figs. 2.5c, d). The regression coefficient reveals temporal peak in early winter and a weak signal in mid-winter. The robustness of early winter peak structure in Figs. 2.5c and 2.5d is further tested by counting the number of grid points in each domain that show statistically significant regression coefficients at the 95% confidence level. Its

temporal evolution remarkably resembles Figs. 2.5c and 2.5d with distinct early winter peak and almost zero in mid-winter (not shown). Since such temporal variability is inconspicuous in the monthly- or seasonal-mean analyses (Kim et al., 2018), this result suggests that the sub-seasonal ENSO teleconnections over East Asia is distinguishable from the conventional seasonal-mean ENSO teleconnections.

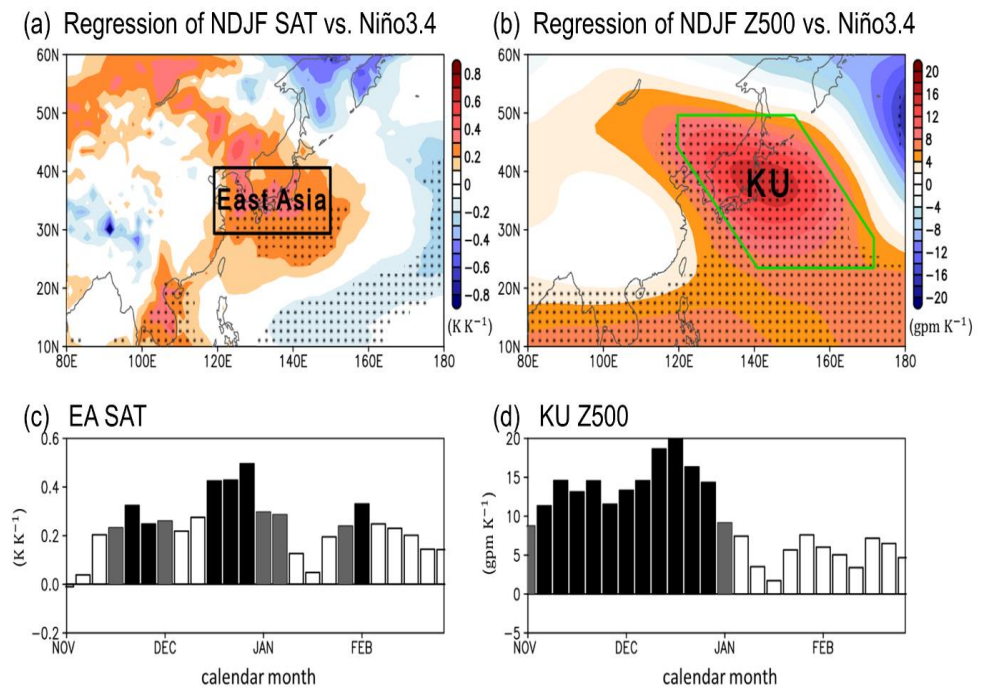

Figure 2.5. (a,b) NDJF-mean (a) SAT and (b) geopotential height at 500 hPa (Z500) regressed onto Niño 3.4 index.. (c,d) As in (a,b) but for the sub-seasonal evolution of the (c) SAT over the East Asia and (d) Z500 over the Kuroshio Extension (KU). The dotted area and black (gray) bar indicate statistically significant values at the 95 % (90%) confidence level based on a student's t-test.

The robust sub-seasonal teleconnection is attributed to the KU circulation change (Fig. 2.6). Figure 2.6a shows that the correlation of the KU Z500 and SAT in December when the ENSO-East Asia teleconnection is robust. A significant interannual correlation between the KU Z500 anomaly and the SAT anomaly over the East Asia region (dotted area). The identified positive relationship between them indicates that warm anomalies over the East Asia are closely associated with the strengthening of the KU circulation because the associated horizontal wind anomalies transport a relatively warm and moist air to the East Asia (Fig. 2.6c). The significant interannual correlation between the KU Z500 anomaly and East Asian SAT anomaly remains almost same in mid-winter (Fig. 2.6b). However, as the KU Z500 anomaly (i.e., key for the ENSO-East Asia teleconnection) weakens, the horizontal wind anomalies also weaken (Fig. 2.6d), resulting in the insignificant relationship in mid-winter.

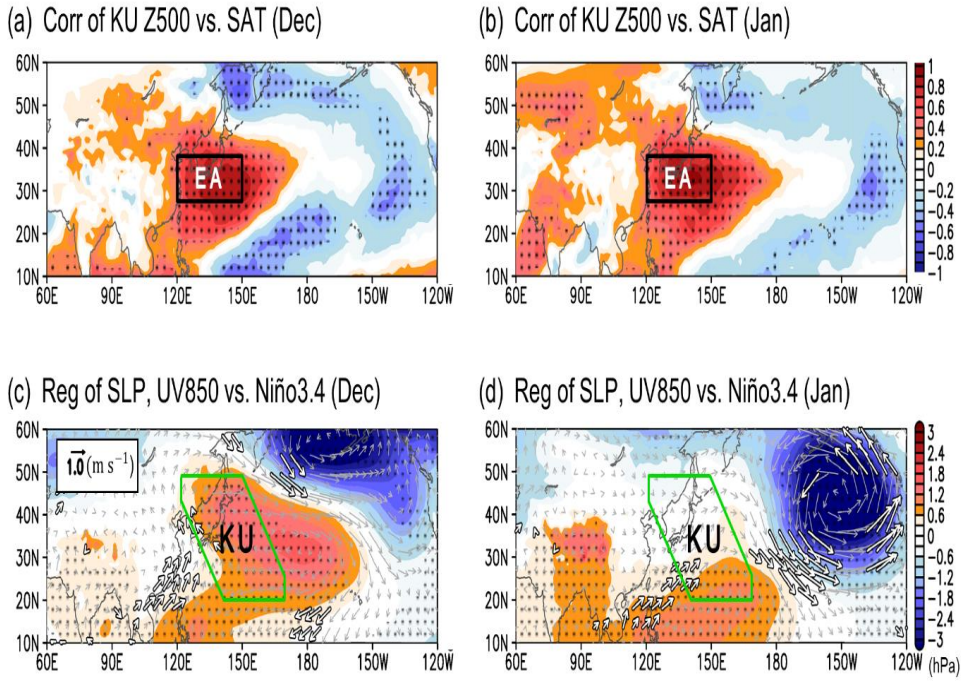

Figure 2.6. (a,b) Correlation between the SAT and KU Z500 in (a) Dec and (b) Jan. (c,d) As in (a,b) but for SLP and UV850 regressed onto the Niño 3.4 index. The dotted area and thick arrows indicate statistically significant values at the 95 % confidence level based on a student's t-test.

2.3. Mechanisms with an idealized model experiment

2.3.1. A hint in tropical convection: Indian Ocean

Since ENSO teleconnection is interpreted as an anomalous Rossby wave propagation resulting from the latent heat release of equatorial deep convection (e.g., Hoskins and Karoly, 1981), the tropical convection changes are examined as a possible cause of the sub-seasonal ENSO teleconnection (Fig. 2.7).

Figure 2.7a shows the NDJF-mean precipitation pattern associated with ENSO events, obtained by regressing the NDJF-mean precipitation anomaly onto the normalized seasonal-mean Niño 3.4 index. During El Niño years, tropical convection is weakened in the Maritime Continent/western Pacific (MC) but strengthened in both CP and Indian Ocean (IO) (Fig. 2.7a). This tripolar pattern results from the anomalous Walker circulation (Bjerknes, 1969), a large-scale circulation in a zonal direction, modulated by ENSO (Philander, 1989). In the El Niño years, the Walker circulation shifts eastward compared to normal, and descending and ascending motions occur in MC and CP, respectively. As a result, an anomalous positive SST, convergence, water vapor, and deep convection are in the CP (Lindzen and Nigam, 1987). Since the Walker circulation is closely connected to both IO and CP (Webster, 1983), the positive precipitation anomaly appears not only in CP but also in IO

(green shading in Fig. 2.7a).

Figure 2.7b shows the pentad-mean precipitation anomaly evolutions regressed onto the ENSO index. The tropical precipitation shows different sub-seasonal evolutions depending on the regions. In the El Niño year, CP precipitation is gradually enhanced until January and tends to be maintained during January and February (gray line in Fig. 2.7b). This is because CP precipitation is directly coupled with SST (Lindzen and Nigam, 1987). Following the SST with a longer memory, the CP precipitation also shows a monotonous sub-seasonal evolution. A similar result is also observed in MC but with the early winter peak (black line in Fig. 2.7b). The negative precipitation anomaly is strongest in early December. The dry precipitation anomaly over the MC is insignificant in January, thereby resonating with the Kim et al. (2018) findings, highlighting its critical role in the sub-seasonal variability of the ENSO teleconnection in East Asia. On the other hand, IO precipitation exhibits a clear enhancement around mid-December, and a little significant anomaly appeared in the rest of the period (green line in Fig. 2.7b). The result is not sensitive to the definition of the domain.

What drives the changes in IO convection in early ENSO years? To figure out the physical mechanism of the enhanced IO convection in early El Niño winter, the upward motion and its associated horizontal wind, and specific humidity is investigated (Fig. 2.8).

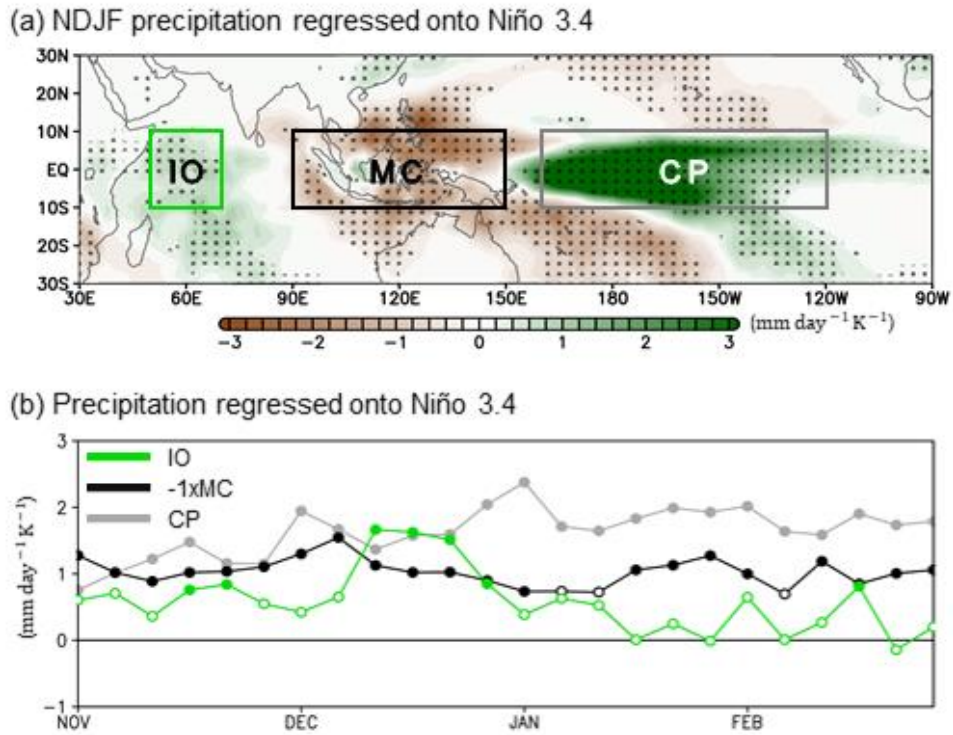

Figure 2.7. (a) NDJF-mean precipitation regressed onto Niño 3.4 index. (b) Sub-seasonal evolution of the area-mean precipitation over the Central Pacific (CP), Maritime Continent (MC), and Indian Ocean (IO). The dotted area and lines indicate statistically significant values at the 95 % confidence level based on a student's t-test.

Figure 2.8a shows the NDJF-mean upward motion, horizontal winds, specific humidity pattern associated with ENSO events, obtained by regressing the NDJF-mean anomalies onto the normalized seasonal-mean Niño 3.4 index. During El Niño years, an anomalous downward motion is robust in MC region (orange contour in Fig. 2.8a). The associated easterly wind anomalies are observed in IO and MC region

(arrows in Fig. 2.8a), leading to the spatial distribution of the moisture anomalies (shading in Fig. 2.8a).

As the anomalous downward motion becomes stronger around mid-December (orange and black lines in Fig. 2.8b), they supply a significant level of moisture anomaly to the IO (green line in Fig. 2.8b). Because the MC is climatologically moisture-rich, the statistically significant horizontal wind anomalies, together with the climatologically plentiful moisture in MC, can bring moist air to the IO.

Since moisture plays an important role in the growth (Brown and Zhang, 1997; Holloway and Neelin, 2009) and onset (Sherwood, 1999; Takayabu et al., 2006) of the convection, a scatter plot between the column integrated relative humidity (CRH) and OLR is examined during the December 2nd to 26th (Fig. 2.9). As the moisture increases, the convection becomes strong nonlinearly. Here it is important to note that the CRH-OLR relationship is nonlinear like the CRH-precipitation relationship (Bretherton et al., 2004; Rushley et al., 2018). Under moist condition, a small increase of moisture can efficiently enhance the convection. This result indicates that the moisture supply during early winter (Fig. 2.8b) can efficiently boost the enhanced convection over the IO (Fig. 2.7).

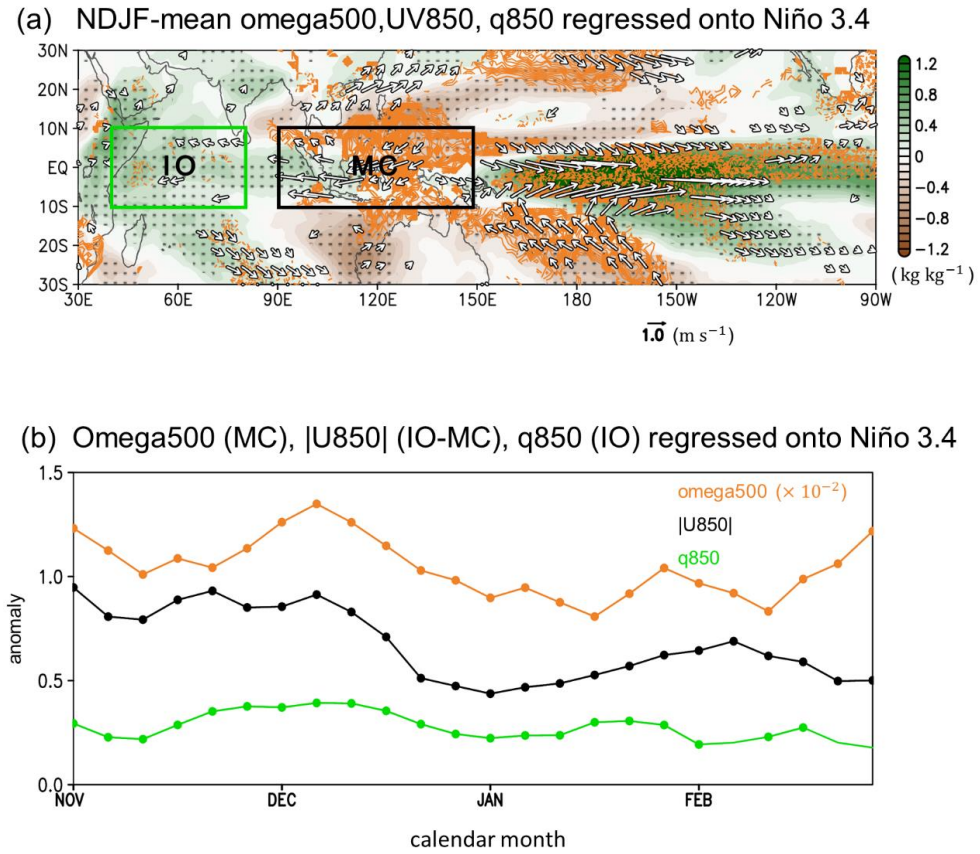

Figure 2.8. (a) NDJF-mean 500 hPa vertical velocity (omega500; orange contour; only significant values are presented), horizontal winds at 850hPa (UV850; white arrows; only significant values are presented), 850 hPa specific humidity (q850; shading) regressed onto the Niño 3.4 index. (b) Sub-seasonal evolutions of the pentad-mean omega500 over the MC (orange), q850 over the IO (green), and |U850| (black) averaged from the IO to the MC, respectively. All results are derived from the observation. The dotted marks and thick arrows indicate statistically significant values at the 95 % confidence level based on a Student's t-test.

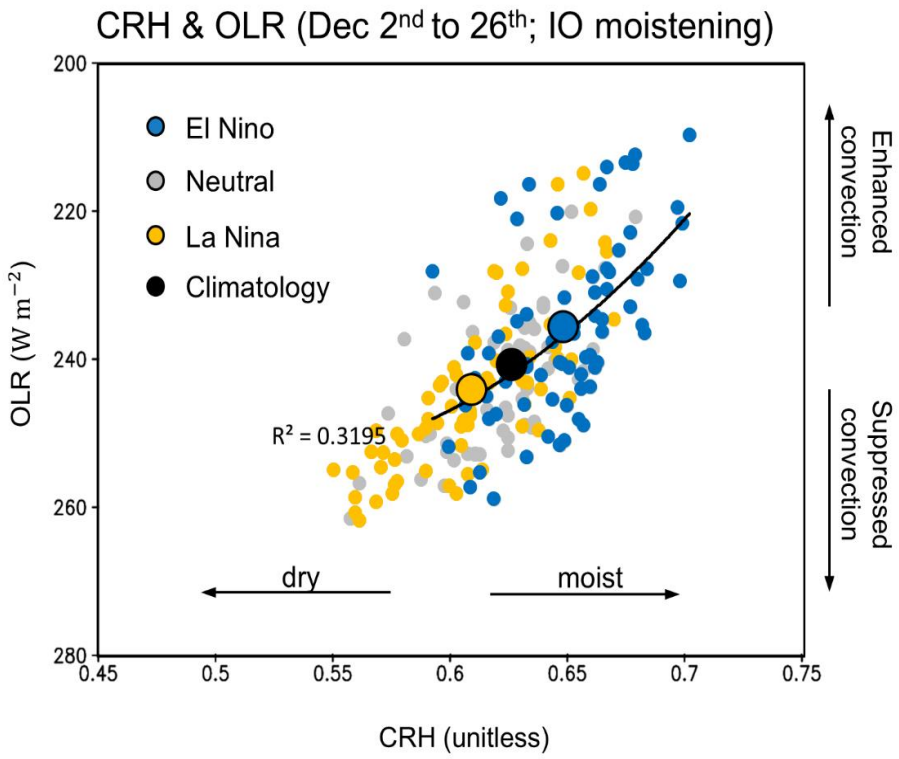

Figure 2.9. Nonlinear column integrated relative humidity (CRH)-OLR relationship over the IO between El Niño versus La Niña years.

The positive humidity tendency in early winter is tightly connected to the horizontal advection term (Fig. 2.10). Figure 2.10 shows the moisture budget analysis over the IO domain. Before the IO convection peak, the strong positive IO moisture tendency peak appears in advance (black line). This positive peak of moisture tendency is closely related to the horizontal moisture advection term (cf. black and blue lines). The relatively high pattern correlation between the moisture tendency and the horizontal advection term over the IO (r = 0.5), indicating that the moistening is mainly driven by this horizontal

moisture advection. The enhanced IO convection indeed peaks in one-pentad later than the peak of moisture, indicating that the moistening leads to the enhanced convection in early winter.

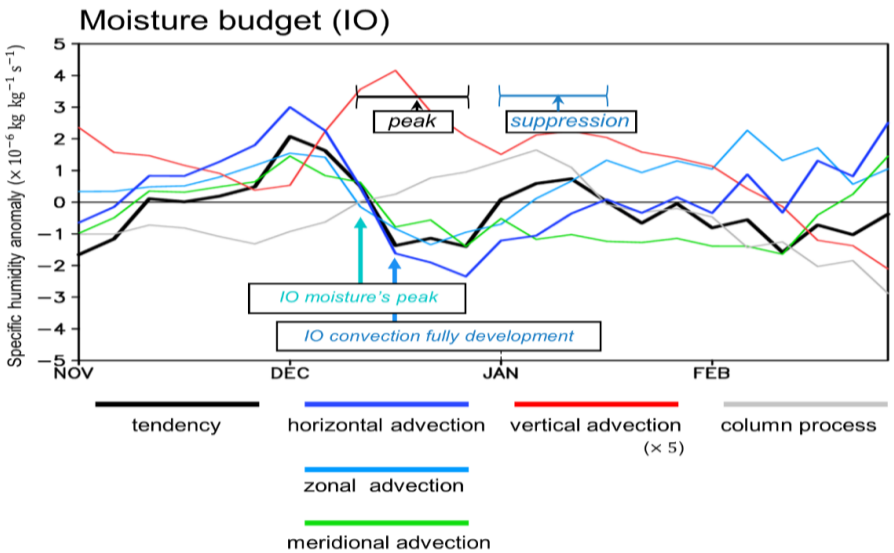

Figure 2.10. Moisture budget analysis over the IO during El Niño years.

A qualitatively similar result can be found in a composite analysis (Fig. 2.11) and each El Niño winter case (Fig. 2.12). The enhanced IO convection in early ENSO winter also appears when non-linear relationships are included (Fig. 2.11) Moreover, each 14 El Niño winter is accompanied by the enhanced IO convection in early winter (Fig. 2.12) due to the horizontal moisture advection (not shown). Interestingly, the number of MJO events, which is the dominant sub-seasonal variation of the tropical convection, increases in the phase 1-3,

indicating that the enhanced convection is located in the IO (Fig. 2.13). The above results re-confirm the IO convection enhancement is robust in early ENSO winters.

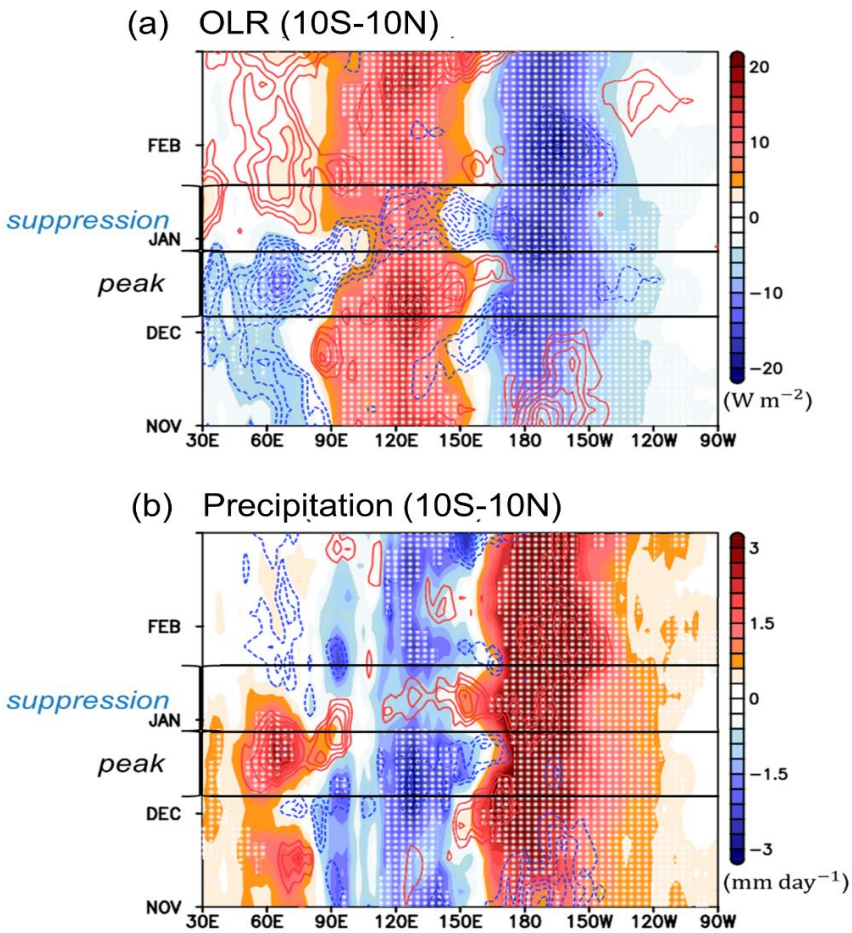

Figure 2.11. (a,b) Hovomoller diagram of the (a) OLR and (b) precipitation anomalies over the tropics in El Niño years. The dotted area indicate the statistically significant values at the 95 % confidence level. The red contour indicates the intraseasonal positive anomaly by subtracting the seasonal-mean anomaly from the pentad anomaly. The blue contour also indicates the intraseasonal negative anomaly. The contour interval is 1 $\mathrm{W\,m^{-2}}$ starting from 1 $\mathrm{W\,m^{-2}}$ in (a), and 0.3 $\mathrm{mm\,day^{-1}}$ starting from 0.3 $\mathrm{mm\,day^{-1}}$ in (b).

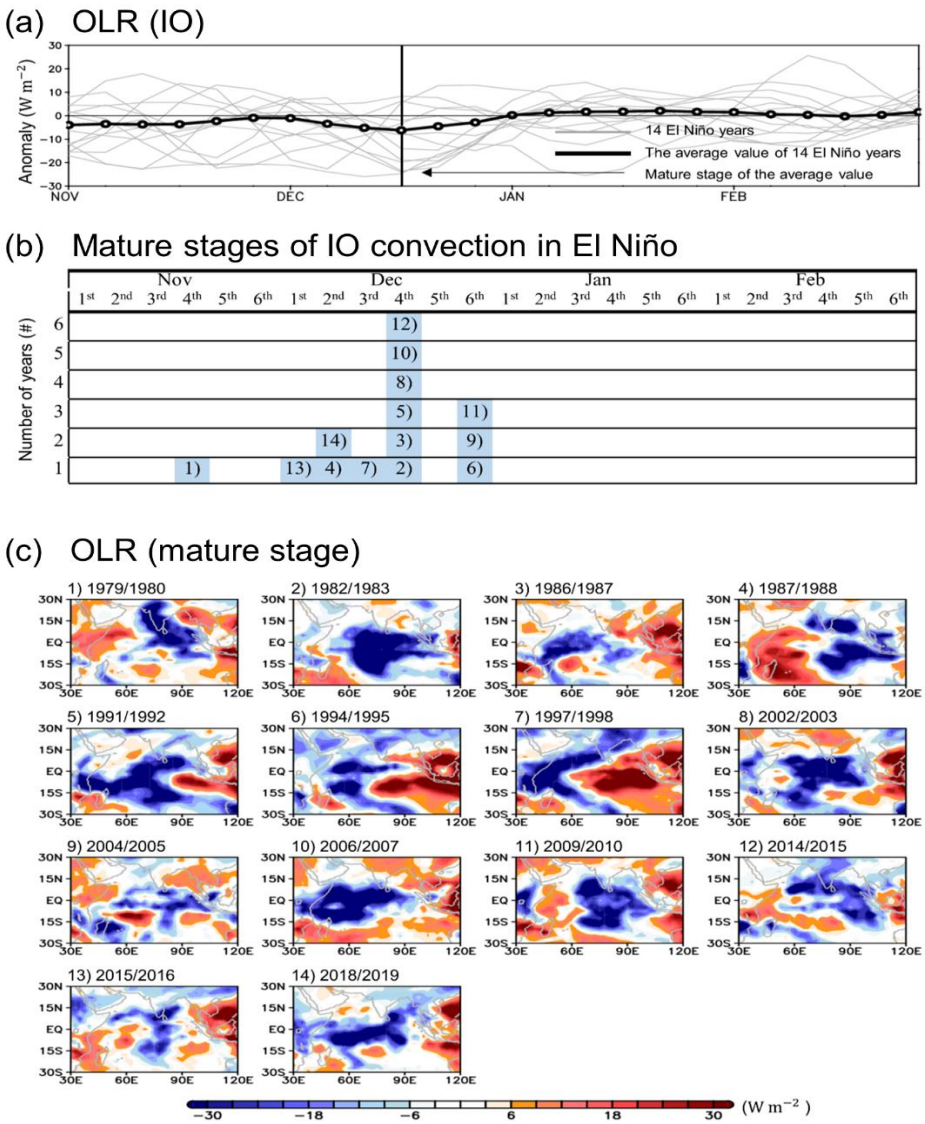

Figure 2.12. (a) Temporal evolutions of outgoing longwave radiation (OLR) anomalies over the IO in each El Niño year (gray), their average value (black), and the mature stage of the IO convection based on the average value (vertical line). (b) Mature stages of IO convections in each El Niño year. (c) The OLR anomaly map at the mature stage of each El Niño year, defined in b. The longitudinal ranges of the IO domain in (a) are defined as 70°–90°E in 4),12) cases and 40°–60°E in 6),7),14) cases to pick up the enhanced convection (blue shading in c).

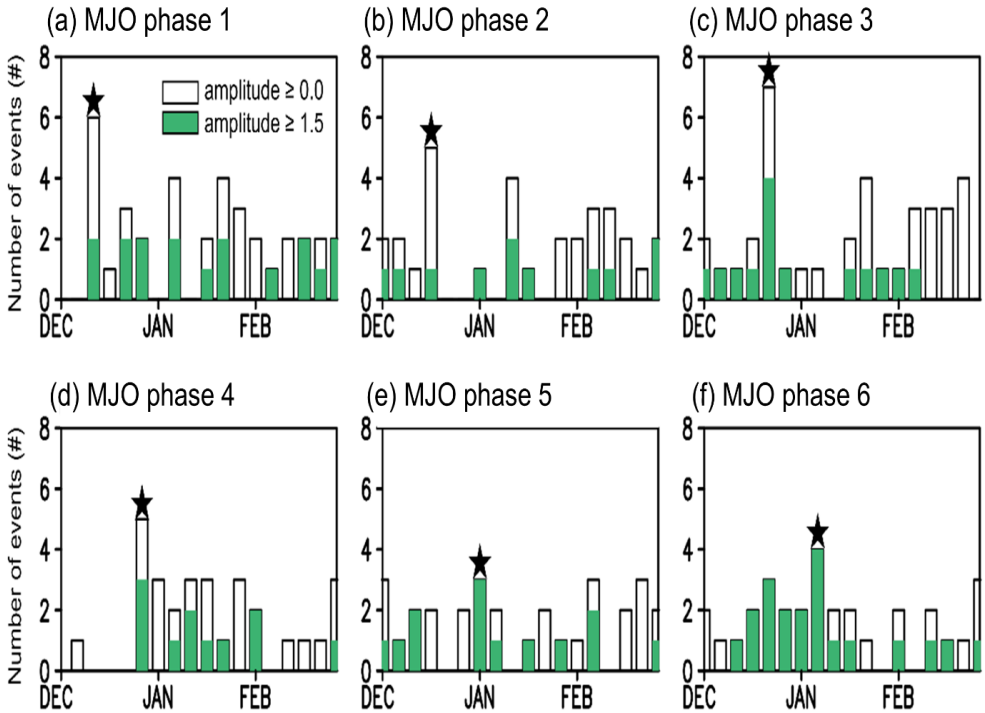

Figure 2.13. (a-f) Number of MJO events in El Niño years from phases 1 to 6 (from IO to MC and western Pacific). The outline bar indicates all the MJO cases and green filled bar indicates strong MJO cases (amplitude $\geq$ 1.5). Star denotes the period of the highest MJO frequency for each phase (from phase 1 to 6) is observed. The MJO phases are defined by using the OLR based MJO index (i.e., OMI index).

To reveal the association between the sub-seasonal variability of the ENSO teleconnections and these tropical convection anomalies, the partial regression of atmospheric variables against the Niño 3.4 index or the CP, MC, IO precipitation anomalies are conducted (Fig. 2.14). To separate the IO, MC, and CP impacts on mid-latitude atmospheric circulation, a regression is applied after removing their relative signals.

Figure 2.14 shows the partial lagged regression of the Z500 anomaly on the IO, MC, and CP precipitation anomalies. Here, the MC dry anomaly is multiplied by -1 for a direct comparison with IO and CP precipitation. A yearly time series of the area-averaged precipitation anomalies at their maximum periods are regressed onto the Z500 anomaly with +2 pentad lags. For instance, Figure 2.14a shows the Z500 anomaly related to the IO precipitation anomaly at the 9th pentad, when the IO precipitation anomaly is at the maximum (green line in Fig. 2.7b). The same partial regression analysis is also carried out with respect to MC- and CP-convection-induced teleconnection, as indicated shadings in Figs. 2.14b and 2.14c. A comparison between the figs. 2.14a-c clearly shows that the KU Z500 responses to the CP convection are opposite to that of MC and IO. While CP convection governed the development and maintenance of the cyclonic anomaly over the North Pacific region during El Niño winters (Fig. 2.14c), IO and MC convection induces an anticyclonic anomaly over the KU region (Figs. 2.14a and b). The IO-convection-related NP Z500 anomaly is roughly similar to the MC-related anomaly in magnitude (values in the left boxes in Figs. 2.14a and b).

Based on its sub-seasonal evolution and the associated teleconnections (Figs. 2.7 and 2.14), the observed sub-seasonal variability of ENSO teleconnections shown in Fig. 2.5 can be attributed to the tropical convections. The above results further indicate that the mid-

winter weakening of ENSO teleconnections is likely caused by the weakening of the IO-, and MC-convection-induced teleconnection in late December and early January as IO and MC convection is anomalously weakened in mid-December during El Niño winters. Although destructive interference of the MC- and CP-convection-induced teleconnections has been previously reported in East Asia (Son et al., 2014; Kim et al., 2018), the possible role of the IO- and MC-convection-induced teleconnections has not been studied yet.

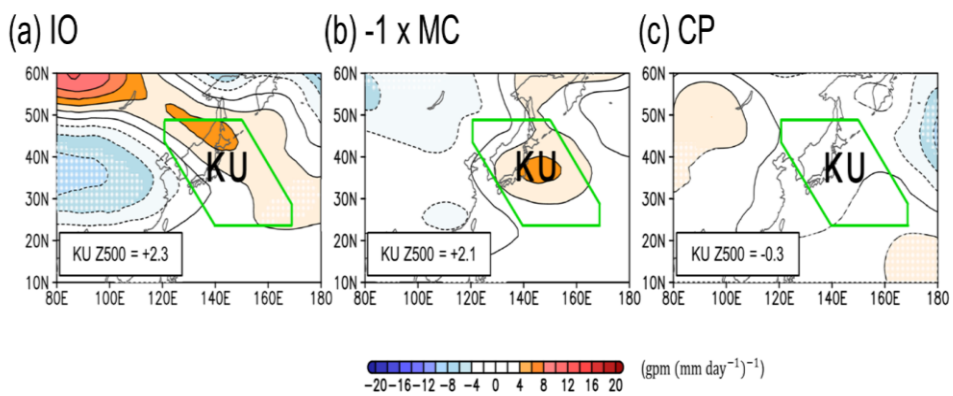

Figure 2.14. 2-pentad lagged partial regression of a yearly time series of Z500 anomaly onto the yearly time series of (a) IO, (b) MC, (c) CP precipitation anomalies from the convection's maximum period. The dotted marks represent statistically significant values at the 95% confidence level based on a Student's t-test. The contour interval is 2 $\text{gpm } (\text{mm day}^{-1})^{-1}$.

This assumption is explicitly tested by comparing the ENSO-related Z500 anomalies in the observation and those reconstructed by combining Z500 anomalies regressed onto IO, MC, and CP precipitation. The linear combination of CP, MC, and IO influences resembles the observed ENSO teleconnection pattern in both its maximum period (r=0.91 btw. Figs. 2.15a and b) and minimum period (r=0.92 btw. Figs. 2.15c and d). These results indicate that sub-seasonal variability of ENSO teleconnections in the East Asian surface climate can be qualitatively understood as arising from the tropical convection not only CP but also MC and IO.

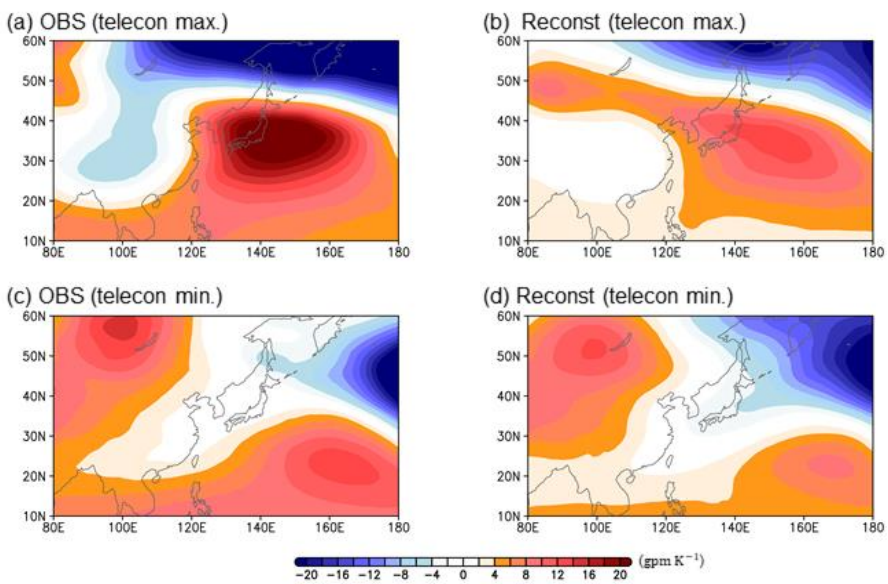

Figure 2.15. (a, c) Observed ENSO-related Z500 anomalies at (a) its maximum and (c) minimum periods. (b, d) Same as (a, c) but for the reconstructed Z500 based on the linear combination of the partial regression coefficients in Fig. 2.14.

2.3.2. Evidence in linear baroclinic experiments

To investigate the causality between tropical convection and KU Z500 response, the atmospheric response to the idealized heat forcing is re-examined in the linear baroclinic model experiment (Fig. 2.16). Similar to observation (cf. Figs. 2.14 and 2.16), three equatorial forcings (i.e., IO, MC, and CP convective heating) are prescribed under the January mean background of the El Niño year (Figs. 2.16a-c) and then a composite analysis is performed. The steady-state atmospheric response is obtained based on the Z500 anomaly at 2-pentad lag-time (i.e., 10-day). It shows a KU Z500 response of IO and MC is an opposite sign to that of CP forcing experiment, consistent with observation. Although the KU Z500 response to the CP forcing shows a marginal effect in this experiment, the result is qualitatively the same as the observed sign. It re-confirms the relative role of IO and MC precipitation on the ENSO-East Asia teleconnections in early winter.

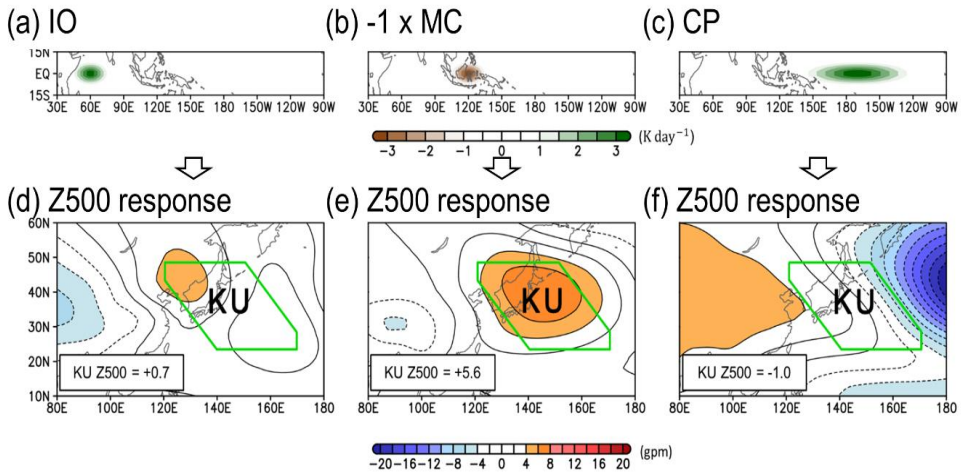

Figure 2.16. (a-c) Idealized thermal forcing, (d-f) The steady-state atmospheric circulation response at 500-hPa in mid-latitudes. 2-pentad lagged Z500 response to the forcings. The contour interval is 2 gpm.

2.4. State-of-the-art multi-model ensemble systems

2.4.1. Prediction skill

To examine the whether the observed sub-seasonal variations of the ENSO teleconnections and its association with the tropical convection is well reproduced in the state-of-the-art hindcast systems, the ACC skill scores of MME SAT and Z500 are investigated (Fig. 2.17). Figure 2.17a shows the ACC of Z500 anomaly over the East Asia region at the 5th pentad. Since the sub-seasonal prediction skill of Z500 in the Northern Hemisphere mid-latitudes is only three pentads (Son et al., 2020), it is expected to observe a small ACC in this period. However, a

high skill appears particularly in the KU region where the ENSO-related Z500 anomalies are persistent in both MME and observation. The skill disappears in later forecast lead time (Fig. 2.17b). Although the area-averaged Z500 skill over the KU appears the statistically significant skill at this period, the relatively high skill disappears around the 9th pentad when the observed IO convection is enhanced but MC convection is weakened. The KU Z500 skill change is also reflected in East Asian SAT prediction skill (cf. Fig. 2.17c and d). These results emphasize the KU Z500 prediction skill is closely tied to the sub-seasonal variation of the ENSO teleconnections associated with the sub-seasonal variations of the tropical convection.

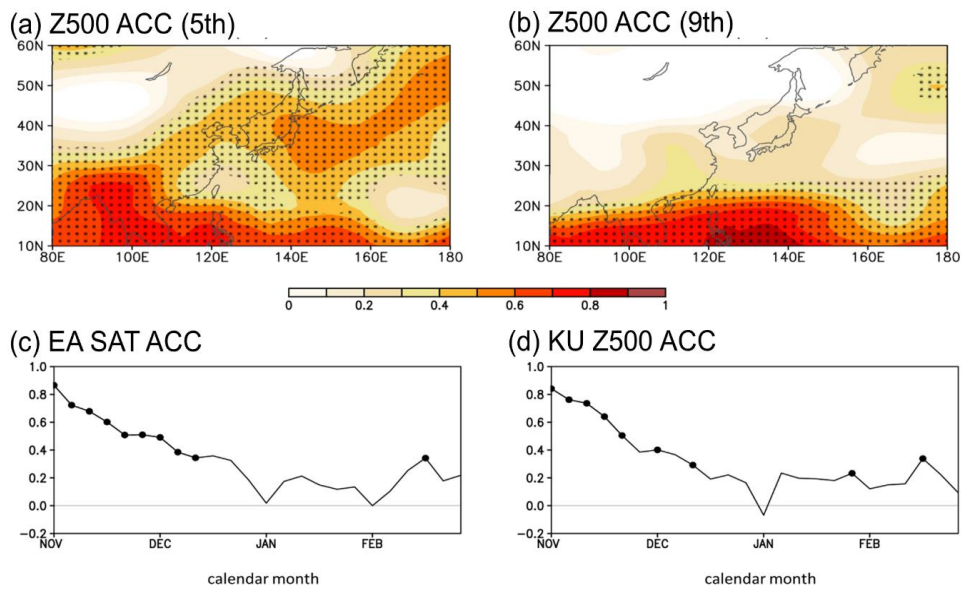

Figure 2.17. (a,b) Anomaly correlation coefficient (ACC) of the Z500 at (a) 5th pentad and (b) 9th pentad. (c-d) ACC of (c) East Asian SAT and (d) KU Z500. The dotted area and lines indicate the statistically significant values at the 95 % confidence level based on the bootstrap method.

2.4.2. Incomplete representation of the tropical convection

To understand the cause of the poor skill in mid-winter, the sub-seasonal variations of the ENSO teleconnections are investigated in the model predictions. Figure 2.18 shows the same regression coefficients as in Fig. 2.5 but for the MME. Similar to the observation, a statistically significant warm anomaly is observed in the East Asia during the seasonal-mean El Niño winters (Fig. 2.18a). In addition, the anomalous anti-cyclonic circulation anomaly in the KU is also well predicted (box in Fig. 2.18b). However, the MME does not reproduce the sub-seasonal variation of ENSO teleconnections (Figs. 2.18c, d). Amplitudes of KU Z500 and East Asian SAT are under-estimated compared to observation. In addition, the sub-seasonal evolution of the East Asian SAT and KU Z500 shows a monotonous increase throughout the winter season. Although the observed responses of East Asian SAT and KU Z500 weaken in mid-winter (Figs. 2.5c, d), their temporal evolution is not found in the MME. This discrepancy between the observation and MME leads to poor prediction skill, especially from mid-December to early January (Fig. 2.17c, d).

Figure 2.19 shows the ENSO-related tropical convection in the MME. The MME simulates similarly a spatial distribution of the NDJF-mean precipitation anomaly (Fig. 2.19a). In the El Niño winters, the

tropical convection is suppressed near the MC and enhanced near the IO and CP. Although the amplitude of the precipitation is under-estimated (cf. Figs. 2.7a and 2.19a), a well-reproduced spatial distribution of the tropical convection leads to a similar seasonal-mean teleconnection pattern in MME compared to that in observation (cf. Figs. 2.5a and 2.18a).

As can be expected from the seasonal-mean precipitation anomaly, the sub-seasonal tropical convection response to ENSO in MME is generally weaker than the observed one (Fig. 2.19b). In terms of the sub-seasonal temporal evolution, the peak of IO precipitation tends to be predicted earlier than the observation. The enhancement of IO precipitation is evident in November, and it becomes weaker in mid-December (green line in Fig. 2.19b). As a result, the response of KU Z500 to the IO convection is not properly predicted in the MME.

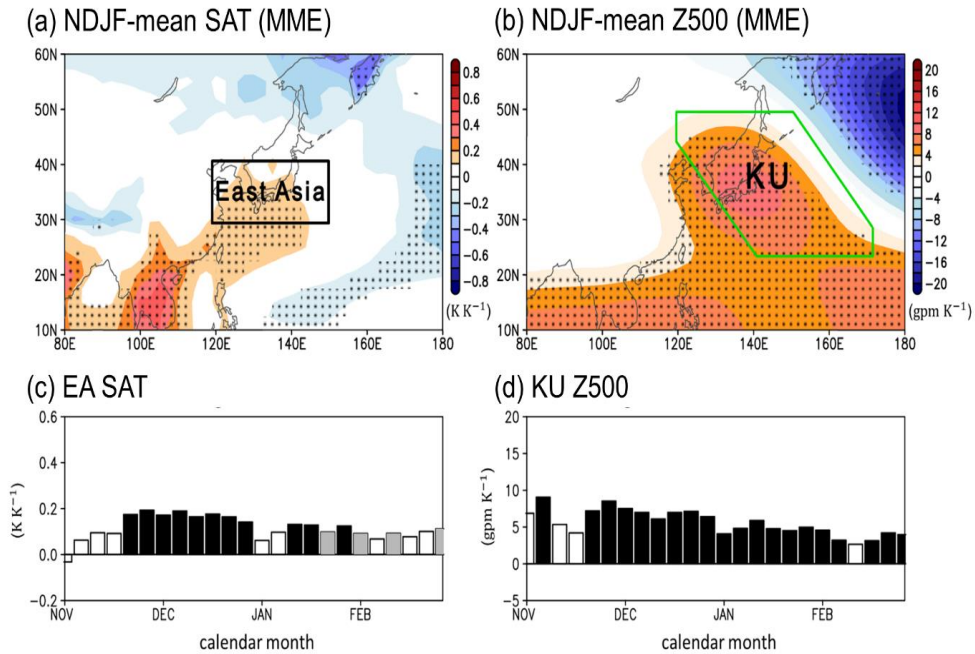

Figure 2.18. Same as in Fig. 2.5 but for the MME.

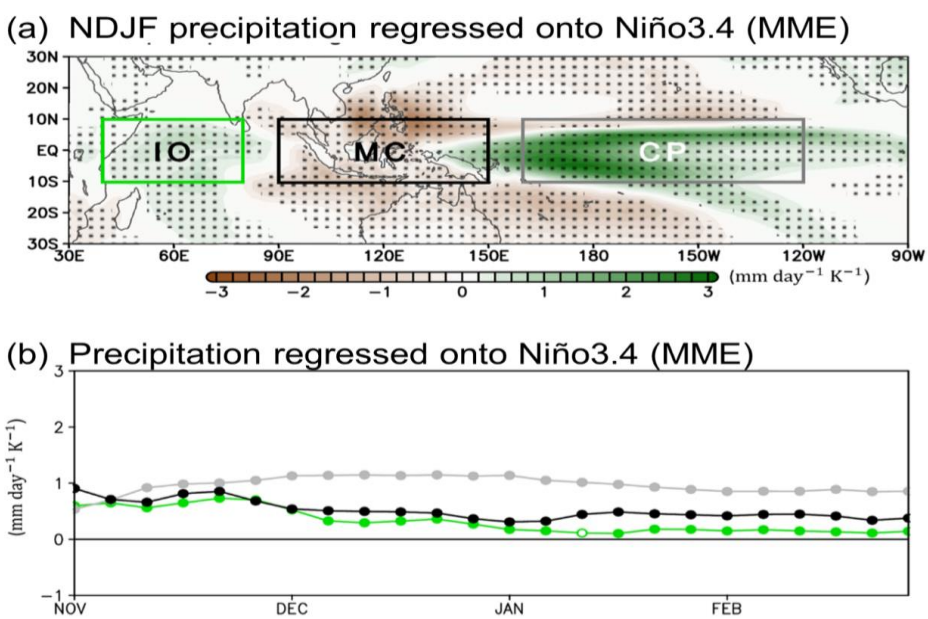

Figure 2.19. Same as in Fig. 2.7 but for the MME.

3. Sub-seasonal variability of QBO downward coupling

3.1. Data and Methods

3.1.1. Observation and climate model simulations

The QBO index is defined as the two-month running mean zonal wind, obtained from the radiosonde observations archived at the Freie Universität of Berlin (Naujokat, 1986). For the analysis, the monthly mean zonal winds at equatorial stations (Canton Island, Gan/Maledive Islands, and Singapore) are merged as one QBO index (Fig. 3.1). Among a variety of QBO indices (as summarized in Table 3.1), the zonal wind at 70 hPa (U70) is primarily used, since the overall results are not sensitive to the choice of the QBO index.

To examine the influence of QBO on atmospheric circulation and surface climate, two-month running mean fields are also constructed from the Japanese 55-year reanalysis (JRA-55; Kobayashi et al., 2015) for 61 years from August 1958 to July 2019. To figure out the effect of the artifact of satellite data assimilation, JRA-55 conventional reanalysis (JRA-55C; Kobayashi et al., 2014) from August 1973 to July 2012 is also used. In-situ measurements from the East Asia meteorological administrations including KMA are also used to enhance the confidence of the reanalysis data results.

To achieve our goals, 'evaluation of the relative importance of the QBO to ENSO', we define ENSO index as the two-month running mean SST over the Niño 3.4 region (170°–120°W, 5°S–5°N), obtained from NOAA Extended Reconstructed SST data version 5 (ERSSTv5; Huang et al., 2017). The QBO impact has been further tested after removing AO-related signal from the SAT. The AO index is obtained from NOAA website and then two-month running mean index is defined in the same way as other indices. All the results are with detrended anomalies and the anomaly is defined as the deviation from the monthly climatology.

To evaluate whether the observed surface impacts and the combined effect of ENSO and QBO are well simulated in current climate models, 8 QBO-resolving multi-model data participating in QBOi Exp2 and QBOi-ENSO experiment are used. The two experiments are one of experiments of QBOi, a new activity coordinated under SPARC to evaluate the QBO presentations in different general circulation models, and to quantify the uncertainty of the models (Bushell et al., 2022; Anstey et al., 2022). The QBOi Exp2 experiment is a timeslice experiment that uses climatological SST and sea ice conditions as a boundary conditions and forcings based on the 1988–2007 period. Since all interannual variability in Exp2 arises from internal atmospheric dynamics, it excludes a potential impact of the ENSO on the interannual variability through the SST boundary conditions. QBOi-ENSO

experiment is designed to figure out the modulations of QBO and its teleconnection by ENSO phase by prescribing perpetual El Niño and La Niña SST anomalies. The details of the QBOi model and QBO definition are summarized in Table 3.2.

To evaluate the prediction skill of the QBO downward coupling and QBO-East Asia teleconnection, the KMA Global Seasonal Forecasting System (GloSea6) is also used (Kim et al., 2021).

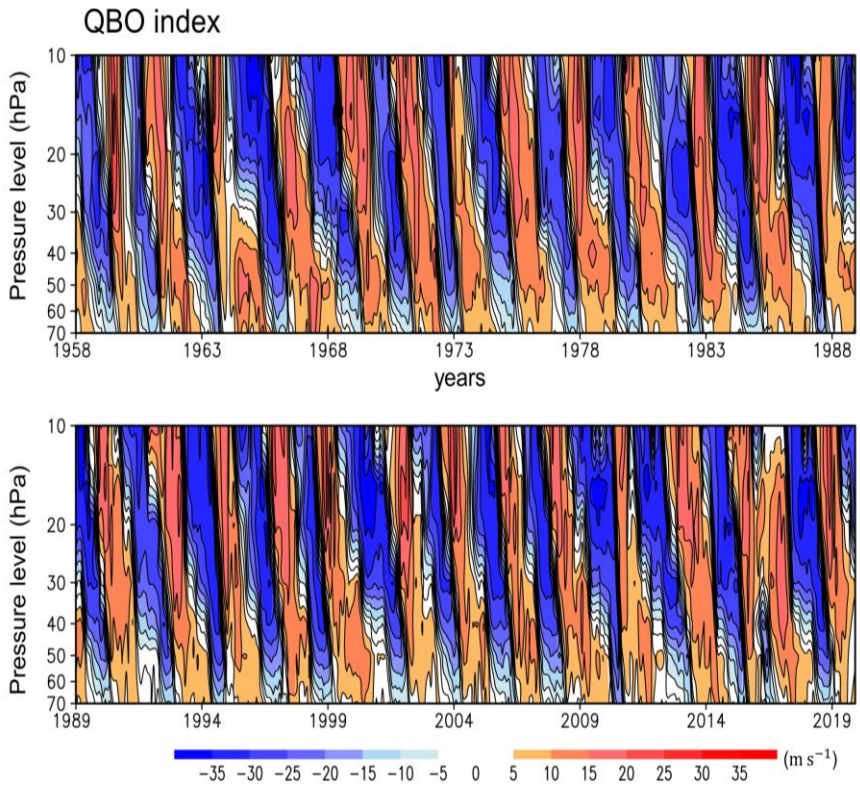

Figure 3.1. Time evolution of the monthly mean zonal winds at equatorial stations (Canton Island, Gan/Maledive Islands, and Singapore). Red and blue shadings denote westerlies and easterlies, respectively.

Table 3.1. The list of QBO definitions.

QBO phase	Definition
Direction at a specific single level	U50 QBO [U] 5S-5N > +/- 0 m/s U30 station data QBO [U] at eq. > +/- 0 m/s U50 DJFM QBO [U] at eq. > +/- 0 m/s U30 DJF QBO [U] at eq. > +/- 10 m/s U70 monthly QBO [U] 10S-10N > +/- 2m/s U30 DJF averaged QBO [U] 2S-2N > +/- 2.5 m/s U40-50 QBO [U] 2.8S-2.8N > + 5m/s (W), - 2.5 m/s (E) U50 QBO [U] at eq. > +/- 0.5 std. U50 QBO [U] at eq. > +/- 0.5 std.
Vertical shear btw. two levels	Vertical shear btw. [U]10-20, 20-30, 30-50, 50-70 [U]50-70 at eq. > +/- 0.5 std. DJF-averaged [U]50-70 5S-5N > +/- 0 m/s
Vertical structure based on two dominant modes	The phase angle is 45 degree (W), 225 degree (E) based on the phase diagram of EOF1 and EOF 2 of U10-70 (+ 5-month running mean, Anstey et al. 2010)

Table 3.2. Details of the QBOi models and QBO definition.

Models	Dimensions (lon×lat×lev×time)	QBO definition	Std. of FM QBO (EXP2, El, La)
MRI-ESM2.0	320×160×80×50 yrs		5.4, 4.3, 5.4
EC-EARTH	512×256×91×100 yrs	WQBO:	5.1, 4.5, 4.6
ECHAM5sh	192×96×95×40 yrs	FM-mean [U] 70 hPa (2°S–2°N)	2.6, 1.8, 2.5
MIROC-ESM	128×64×80×100 yrs	> 0.5 std.	1.6, 2.1, 1.3
LMDz	144×143×79×82 yrs	EQBO: FM-mean [U] 70 hPa (2°S–2°N)	1.4, 1.8, 1.4
GISS-E2-2-G	144×143×102×30 yrs	< -0.5 std.	3.3, 1.3, 2.1
WACCM	288×192×110×100 yrs		2.4, 1.9, 2.8

3.1.2. Correlation, regression, and composite analysis

The results in this section consist of simple correlation, regression, and composite analysis as in Section 2. To make comparisons easier, the regression coefficients are multiplied by the two standard deviations of the QBO index. The resultant values show a similar magnitude to composite results.

To estimate the linear relationship between QBO and East Asian SAT, Pearson correlation coefficient (R_t) is used. The equation is as follows (Eq. 1).

$$R_t = \frac{\sum_{ii=1}^{n}(SAT_{t,ii}-\overline{SAT}_t)(QBO_{t,ii}-\overline{QBO}_t)}{\sqrt{\sum_{ii=1}^{n}(SAT_{t,ii}-\overline{SAT}_t)^2}\sqrt{\sum_{ii=1}^{n}(QBO_{t,ii}-\overline{QBO}_t)^2}} \quad (1)$$

where t is the month and ii is the year, n is the total number of years. The overbar indicates the climatological mean.

In the same way, the following regression (Eq. 2) was also constructed to quantitatively check the effect of QBO on the SAT,

$$SAT_t = a_0 + a_t\, QBO_t + e_t \quad (2)$$

where a_0 is the intercept, a_t is the regression coefficient, and e_t is the residual of the regression. The lead-lag correlation is also computed to identify the possible causal relationship (Eq. 3) by delaying the QBO index from the Eq. 2 up to i-month in order to check how long the QBO had a relationship with the SAT,

$$SAT_t = b_0 + b_t\, QBO_{t-i} + e_t \quad (3)$$

where i was considered up to 5 months. For instance, in the case of the December SAT, the relationship between SAT_{12} and QBO_{11} to the relationship between SAT_{12} and QBO_7 are considered. Even if i was delayed more than 5 months, the results do not change significantly.

For the composite analysis, the westerly QBO phase (WQBO) and easterly QBO phase (EQBO) are defined based on the QBO index. When the positive QBO index exceeds +0.5 standard deviation then the month is defined as WQBO, and the negative QBO index exceeds -0.5 standard deviation then the month is defined as EQBO. The resultant QBO months are denoted as red and blue colored marks, respectively (Fig. 3.2). The classification of the WQBO and EQBO is not sensitive to the QBO definition (compare Figs. 3.2 and 3.3). To eliminate the ENSO effect, these WQBO and EQBO events are further classified as six cases according to the ENSO phases such as neutral (NENSO), El Niño (WENSO), and La Niña (CENSO) cases as depicted in Fig. 3.2.

The statistical significances of the composite, correlation, and regression coefficients are estimated based on a two-tailed Student's *t*-test.

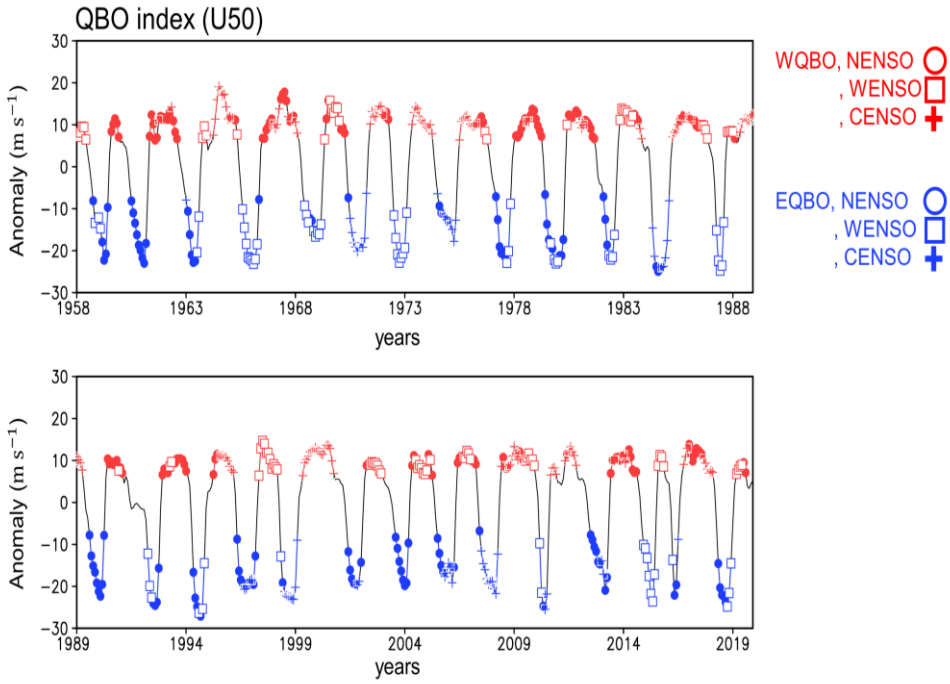

Figure 3.2. Time evolution of the monthly QBO U50 index. Red and blue shadings denote westerlies and easterlies, respectively.

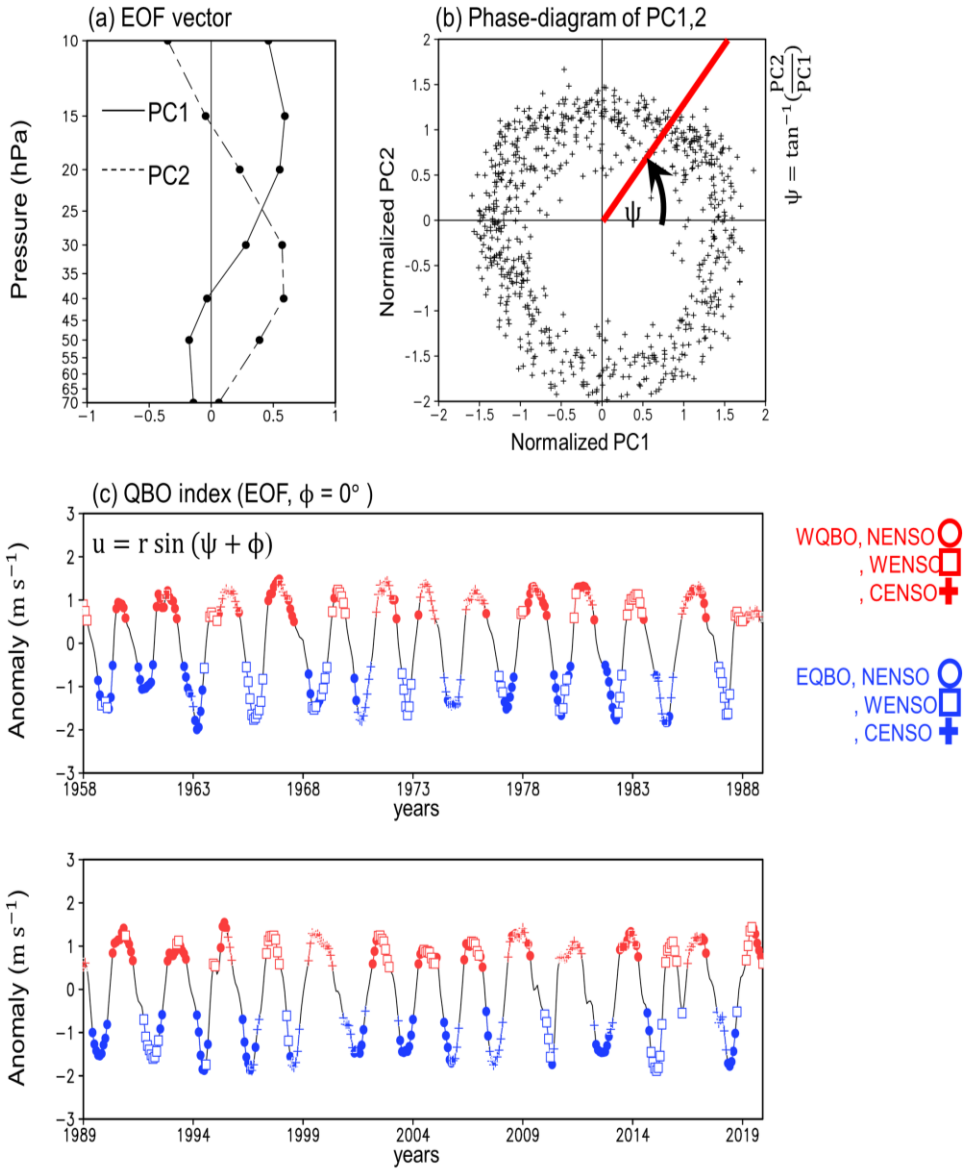

Figure 3.3. Time evolution of the monthly QBO index based on the EOF analysis. Red and blue shadings denote westerlies and easterlies, respectively.

3.1.3. Causality test

Since the QBO has a long-term memory (r = 0.92 at a one-month lag for the QBO-index autocorrelation), it is needed to carefully evaluate the causal relationship. Granger causality test can account into the high memory of the climate variability (Granger, 1969). The key hypothesis of the Granger causality test is to determine whether the inclusion of QBO information (Eq. 5) is helpful to the prediction of the SAT than the case using only SAT itself information (Eq. 4) or not. For the comparison, the two time-lagged regressions are constructed as below:

$$SAT_t = a_0 + \sum_{i=1}^{M} a_i \, SAT_{t-i} + e_{1t} \quad (4)$$

$$SAT_t = b_0 + \sum_{i=1}^{M} b_i \, SAT_{t-i} + \sum_{j=1}^{N} c_j QBO_{t-j} + e_{2t} \quad (5)$$

where the subscript t denotes each month of the year, while i and j denote the monthly time lag from t. The coefficients a_0 and b_0 are the intercepts, a_i, b_i, and c_j are the regression coefficients, and e_{1t} and e_{2t} are the residuals. M and N are the number of optimal time lags for the SAT and QBO index, respectively. The above equations are same as in Section 2.1.3 except for replacing the ENSO to QBO.

Equation (4) represents a lagged auto-regression to estimate SAT_t with the prior values of SAT_{t-i}. Equation (5) estimates SAT_t by considering not only the prior values of SAT_{t-i} but also the prior values of QBO_{t-j}. Here, the FPEs of Equations (4) and (5) are determined by

$\frac{O+M+1}{O-M-1} \times \frac{SSE_1}{O}$ and $\frac{O+M+N+1}{O-M-N-1} \times \frac{SSE_2}{O}$, respectively.

$$\text{Optimal lag} = \text{argmin FPE}_{\text{restricted}} = \text{argmin } \frac{O+M+1}{O-M-1} \times \frac{SSE_1}{O} \quad (6)$$

$$\text{Optimal lag} = \text{argmin FPE}_{\text{unrestricted}} = \text{argmin } \frac{O+M+N+1}{O-M-N-1} \times \frac{SSE_2}{O} \quad (7)$$

The SSE_1 and SSE_2 denote the sum of squared errors of each regression, and O is the number of years (O = 61). An example of FPE is presented in Fig. 3.4. In the case of February–March, both M and N are set to 1.

The selected M and N for each month are listed in Table 3.3. Equation (5) is also applied to the ENSO by replacing the QBO index with the ENSO index. The N*, N substitute for the ENSO, is listed in Table 3.3.

The causal relationship is identified by estimating the usefulness of the prior values of the QBO (or ENSO). When at least one value of c_j is statistically significant according to a two-tailed Student's t-test and all values of c_j collectively improve the variance explained by the regression according to an F-test, it is considered that the QBO (or ENSO) causes the SAT anomaly. Here, F statistics are defined as follows:

$$\text{F statistics} = \frac{(SSE_1 - SSE_2)/N}{SSE_2/(O-P)} \quad (8)$$

where P is the total number of parameters estimated from Equation (5) (e.g., P=1+M+N=1+1+1=3 for February–March; see Table 3.3). The critical values for F statistics are 2.5 in November–December and 4.0 in other months at the 5% significance level, respectively.

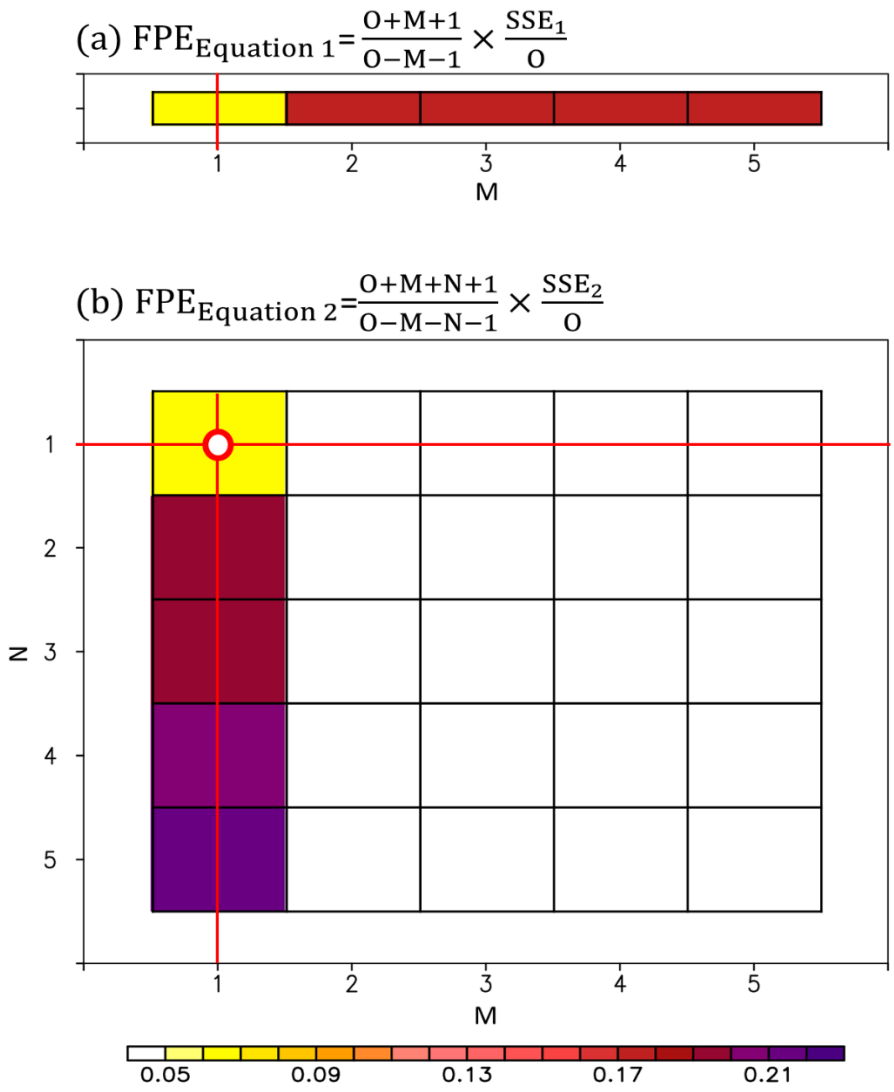

Figure 3.4. Final prediction errors (FPEs; shading) of (a) Eq. 6 and (b) Eq. 7 for East Asia SAT in February–March. O is the number of years at each month (O = 61). M and N are the total numbers of parameters used in Eqs. 6 and 7, respectively. SSE is the sum of squared errors of each regression.

Table 3.3. The optimal time lags for the WNP SAT (M), QBO index (N), and ENSO index (N*), which are derived from the final prediction errors (FPEs; Hsiao, 1981). The first row denotes the abbreviation of the calendar months from AS (August–September) to JA (July–August).

	AS	SO	ON	ND	DJ	JF	FM	MA	AM	MJ	JJ	JA
M	3	5	3	2	3	3	1	2	3	3	4	5
N	1	1	1	4	1	1	1	1	1	1	1	1
N*	1	1	1	1	1	1	1	2	2	2	2	1

The East Asian SAT is known to be affected by ENSO. Therefore, partial Granger causality test considering ENSO is further performed by constructing the following regression equations. The core of the test is to determine whether considering QBO predicts the SAT better than not, and it is the same as the conventional Granger causality test. However, it is different in that it considers ENSO at the same time.

$$SAT_i = a_0 + \sum_{g=1}^{0g} a_g SAT_{i-g} + \sum_{g*=1}^{0g*} b_{g*} ENSO_{i-g*} + e_{1i} \quad (9)$$

$$ENSO_i = c_0 + \sum_{g=1}^{0g} c_g SAT_{i-g} + \sum_{g*=1}^{0g*} d_{g*} ENSO_{i-g*} + e_{2i} \quad (10)$$

$$SAT_i = f_0 + \sum_{g=1}^{0g} f_g SAT_{i-g} + \sum_{g*=1}^{0g*} g_{g*} ENSO_{i-g*} + (\sum_{g**=1}^{0g**} h_{g**} QBO_{i-g**}) + e_{3i} \quad (11)$$

$$ENSO_i = k_0 + \sum_{g=1}^{0g} k_g SAT_{i-g} + \sum_{g*=1}^{0g*} l_{g*} ENSO_{i-g*} + (\sum_{g**=1}^{0g**} o_{g**} QBO_{i-g**}) + e_{4i} \quad (12)$$

Equations 9 and 10 are constrained regression models constructed with the limited effect of QBO. On the other hand, Equations 11 and 12 are unconstrained regression models constructed by

considering the effects of QBO together without limitation.

The criteria for evaluating whether there is a partial Granger causal relationship are: 1) Among g**=1,2,⋯,Og**, there is a significant regression coefficient h_{g**} that passes Student's t-test, 2) whether SSE_1 is significantly improved when adding the QBO information. The significance test for the improvement of SSE was evaluated at 95% confidence level through the F test for the test statistic below (Eq. 13).

$$F = \ln\left(\frac{var(e_{1i})-cov(e_{1i},e_{2i})var(e_{2i})^{-1}cov(e_{2i},e_{1i})}{var(e_{3i})-cov(e_{3i},e_{4i})var(e_{4i})^{-1}cov(e_{4i},e_{3i})}\right) \quad (13)$$

where var and cov denote variance and covariance, respectively. These test statistics indicate the partial effect of the QBO on the East Asian SAT as subtracting ENSO-related $cov(e_{1i}, e_{2i})var(e_{2i})^{-1}cov(e_{2i}, e_{1i})$ and $cov(e_{3i}, e_{4i})var(e_{4i})^{-1}cov(e_{4i}, e_{3i})$ from the total $F = \ln(\frac{var(e_{1i})}{var(e_{3i})})$. Thus, the test statistic indicates that the partial causal relationship between the QBO and the East Asian SAT.

3.1.4. Dry dynamical core model

To understand the QBO downward mechanisms, we employ the dry GFDL. The model consists of a horizontal resolution (T85) of about 1.4° and an even sigma coordinate system (L40) of vertically 40 layers. The model is relaxed to a given radiative equilibrium temperature profile

(T_{eq}; Eq. 14). The T_{eq} mainly follows the original version of Held and Suarez (1994) but with minor modifications to mimic the boreal winter season (contours in Fig. 3.5a):

$$T_{eq}(\phi,p) = \max\left\{200\ \text{K},\ [T_0 - \Delta_h(\sin^2\phi - 2\sin\phi_0\sin\phi) - \Delta_v\log(\frac{p}{p_0})\cos^2\phi](\frac{p}{p_0})^{Rc_p{}^{-1}}\right\} \quad (14)$$

where ϕ is the latitude, ϕ_0 is the thermal equator (= 6°S), p is the pressure, p_0 is the reference surface pressure (= 1000 hPa), T_0 is the surface temperature at the equator (= 315 K), Δ_h is the equator-to-pole temperature difference (= 60 K), Δ_v is the static stability parameter (= 10 K), R is the gas constant of the air, and c_p is the specific heat capacity at constant pressure ($Rc_p{}^{-1}$= 2/7). A small spherical harmonic function of about 0.1 days that occurs during integration is set to attenuate through ∇^8 hyperdiffusion (Garfinkel and Hartmann, 2011a). All experiments were integrated for 5000 days, and the data averaged for 4850 days (151-5000 days) after reaching equilibrium during the total 5000 days of integration period were used for analysis. The simulation without any QBO forcing is referred to 'CTL' run.

3.1.5. QBO nudging experiment

To examine the key mechanism for the QBO downward coupling, the nudging experiment is conducted. The WQBO nudging experiment is conducted by applying an idealized elliptical shape WQBO-like zonal

wind momentum forcing in the lower stratosphere of the CTL run. The shape and magnitude of zonal wind momentum forcing is designed to mimic the observational data based on the Eq. 15:

$$U(p,\phi) = \alpha_0 \exp\left(-\frac{(\phi-\phi_0)^2{\phi_1}^2}{2} - \frac{(p-p_0)^2{p_1}^2}{2}\right) \quad (15)$$

Here, ϕ_0 and p_0 denote reference latitude and altitude, and ϕ_1 and p_1 denote coefficients in latitudinal and vertical directions. The reference latitude and altitude of the forcing are adjusted to the lower part of the stratosphere (70 hPa) of the equator (0°N), and the coefficients in the latitudinal and vertical directions are set to 0.25 and 0.9. In addition, α_0 is set to 10. The given wind forging has a speed of up to 15 m/s similar to the observations (Park et al., 2022). In the same way, the counterpart of the lower stratospheric forcing is set in the upper stratosphere. As a result, two-fold structure of the QBO forcing is applied to the nudging experiment (Fig. 3.5b).

The relaxation time scale $\tau(p,\phi)$ of the nudging is set to 5-day according to the criteria as suggested in QBOi protocol (see black line in Fig. 3.5c):

$$\tau(p) = \frac{\alpha}{4}\left(1 - \tanh\left(\frac{p-p_0}{\Delta p_0}\right)\right)\left(1 + \tanh\left(\frac{p-p_1}{\Delta p_1}\right)\right) \quad (16)$$

$$\tau(\phi) = \frac{\alpha}{4}\left(1 - \tanh\left(\frac{\phi-\phi_0}{\Delta \phi_0}\right)\right)\left(1 + \tanh\left(\frac{\phi-\phi_1}{\Delta \phi_1}\right)\right) \quad (17)$$

Here, p_0 and p_1 represents the reference altitudes and Δp_0 and Δp_1 represents the vertical radius coefficient, and ϕ_0 and ϕ_1 represents the reference latitudes and $\Delta\phi_0$ and $\Delta\phi_1$ represents the horizontal radius

coefficient, respectively. The above coefficients are set to $p_0 = 80$, $p_1 = 8$, $\Delta p_0 = 5$, $\Delta p_1 = 0.5$, $\phi_0 = -12$, $\phi_1 = 12$, $\Delta\phi_0 = 2$, $\Delta\phi_1 = 2$, $\alpha = \frac{1}{4}$. The simulation is referred to 'WQBO' run.

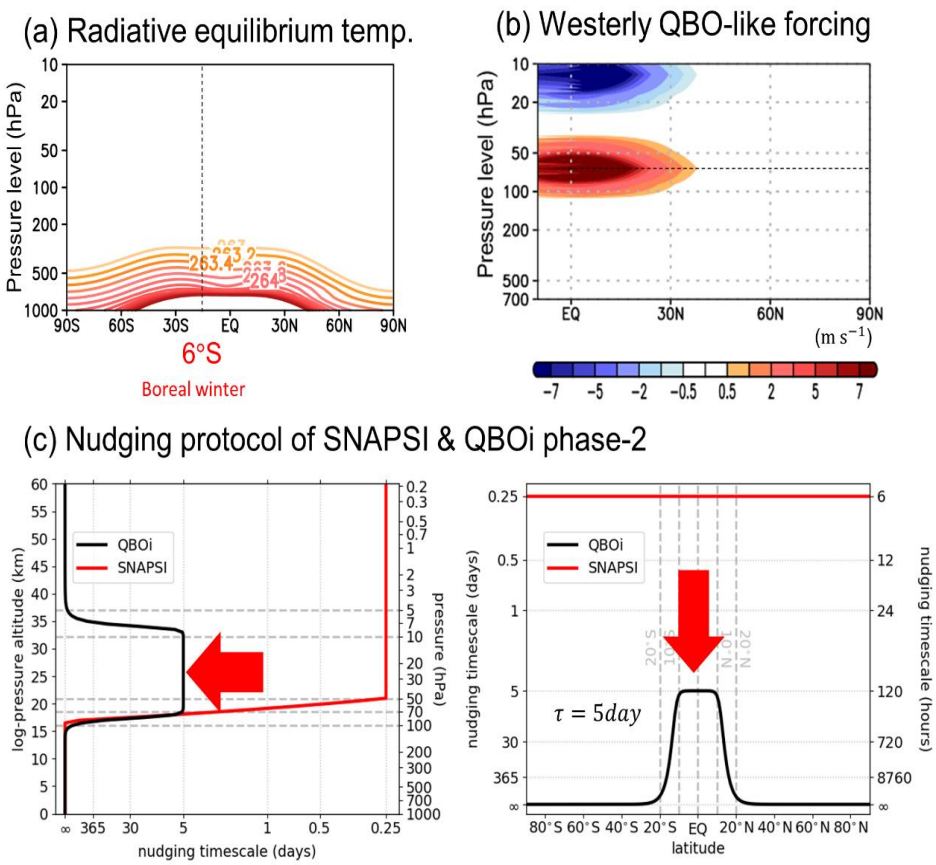

Figure 3.5. Details of control (CTL) and westerly QBO (WQBO) nudging experiments. (a) vertical profile of the radiative equilibrium temperature (b) WQBO-like forcing for the nudging. (c) Vertical and latitudinal profile of the nudging relaxation time adapted from the Stratospheric Nudging And Predictable Surface Impacts (SNAPSI) and QBO initiative (QBOi).

3.2. Impacts and causality

3.2.1. Negative relationship in late winter

Figure 3.6 shows the SAT anomaly regressed onto the QBO index. Although not statistically significant, a positive relationship is observed over northern Eurasia in early winter (Fig. 3.6c–e). This high-latitude signal, which becomes stronger when the mid-stratosphere QBO index is used (e.g., U50), resembles the SAT anomaly associated with the positive AO (e.g., Thompson and Wallace, 1998).

In mid-latitudes, a statistically significant relationship appears over the East Asia and western North Pacific region (110°–170°E, 15°–40°N; red box in Fig. 3.6g) in early and late winter. A significant negative relationship is confined to a small region over East Asia in November–January (Fig. 3.6d, e), as reported in Ma et al. (2021). However, it is more widely distributed in February–March (FM) (Fig. 3.6g). In addition to this negative relationship, a positive relationship appears over western North America, forming east-west dipolar SAT anomalies across the North Pacific. This result indicates that the QBO-SAT relationship is not a local phenomenon but a part of large-scale circulation changes in the North Pacific. The same SAT response is obtained when the composite analysis is conducted (Fig. 3.7).

Figure 3.6g shows that the QBO affects the East Asian SAT in FM.

The QBO westerly phase is particularly related with anomalously cold East Asian SAT. The composite analysis further shows a slight asymmetry in SAT response to the QBO phase. Although the reason is not clear, the East Asian SAT anomaly is slightly stronger in the QBO easterly phase than in the westerly phase (Fig. 3.8).

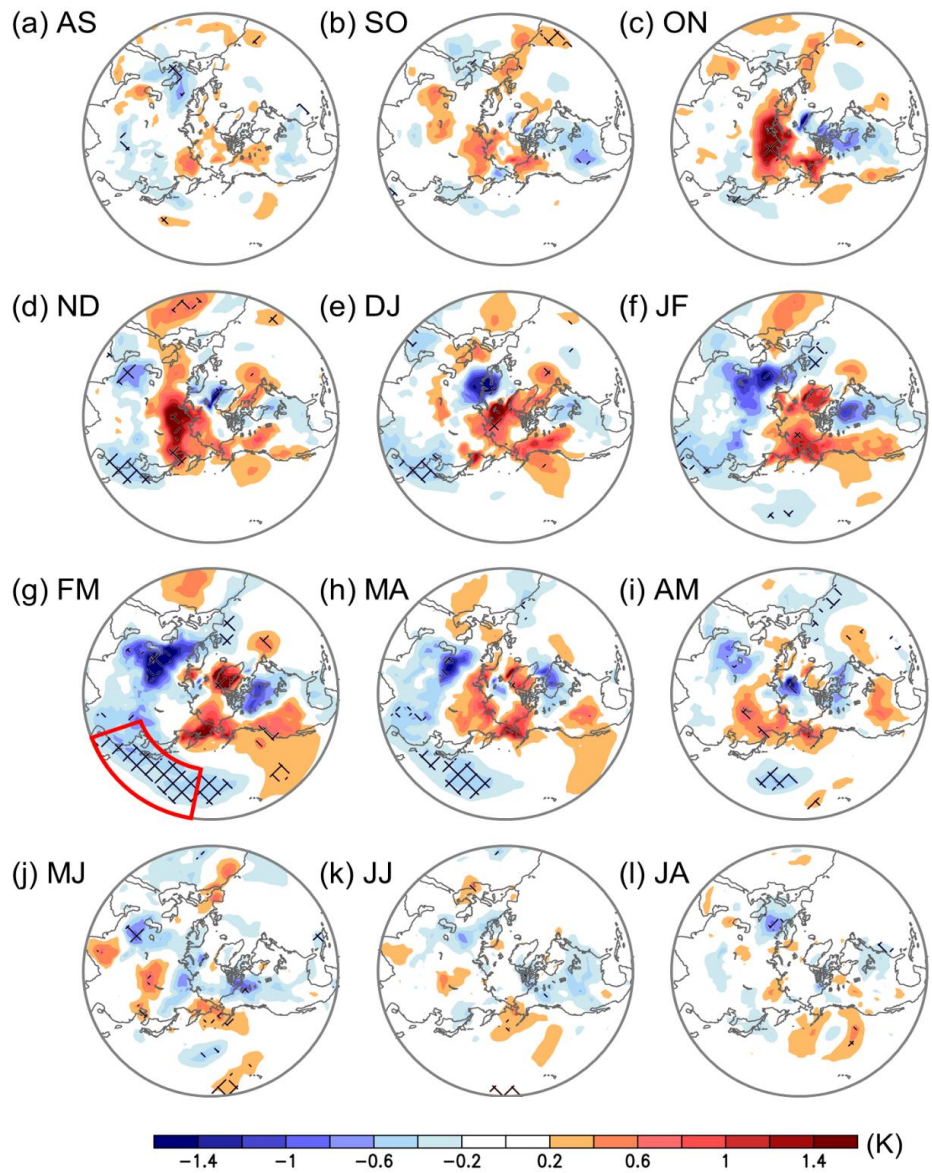

Figure 3.6. The two-month averaged SAT anomaly regressed onto the QBO index (shading; K). The values which are statistically significant at the 95% confidence level are cross-hatched. The red box in Fig. 3.6g denotes the East Asia and western North Pacific region (110°–170°E, 15°–40°N).

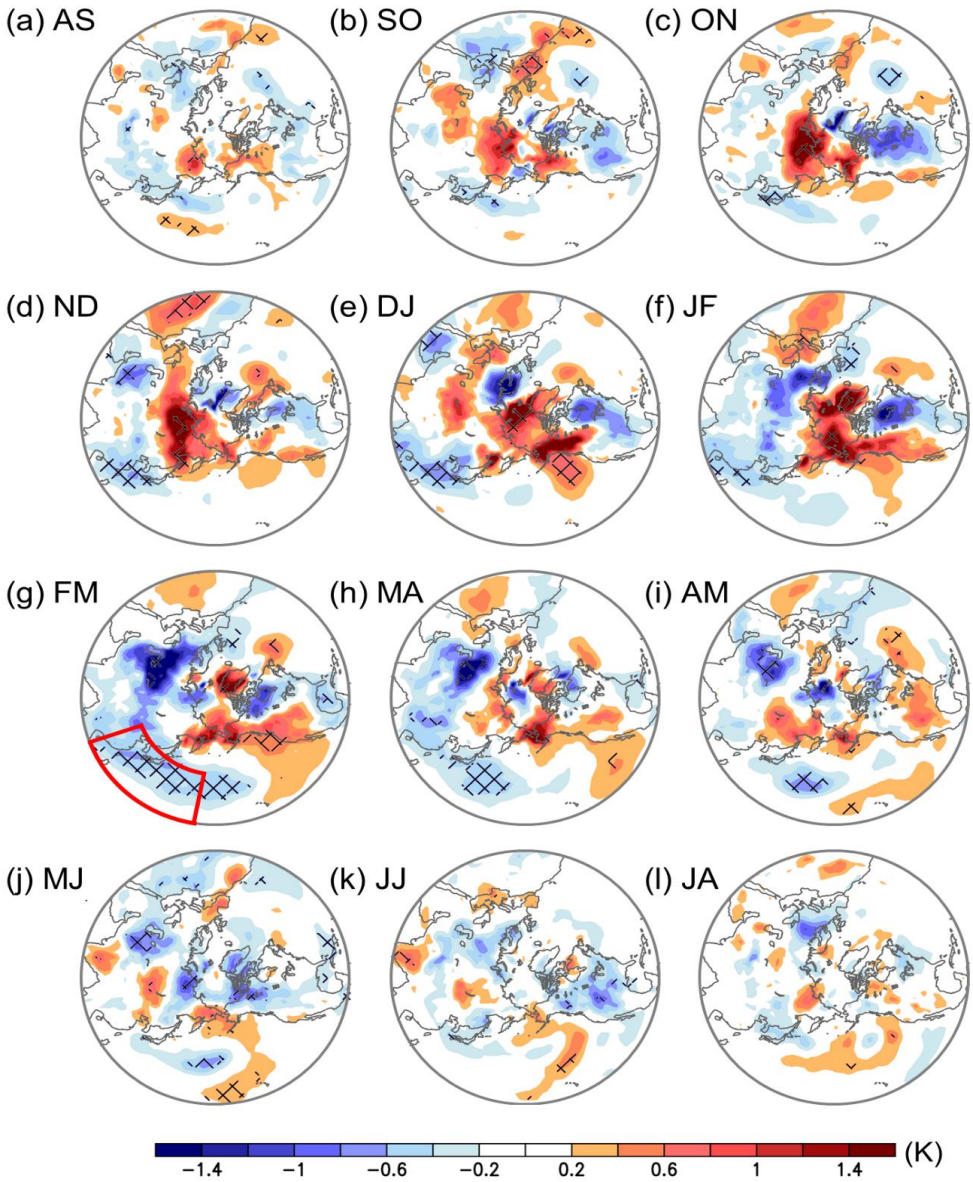

Figure 3.7. Same as Fig.3.6 but for the composite difference between the WQBO and easterly phases (EQBO) (shading; K). Here the WQBO months are defined as the months when the QBO index at 70 hPa is greater than a 0.5 standard deviation. Likewise, the EQBO months are defined as the months when the QBO index at 70 hPa is less than a −0.5 standard deviation. The cross-hatched area denotes the statistically significant difference at the 95% confidence level. Welch's t-test is used.

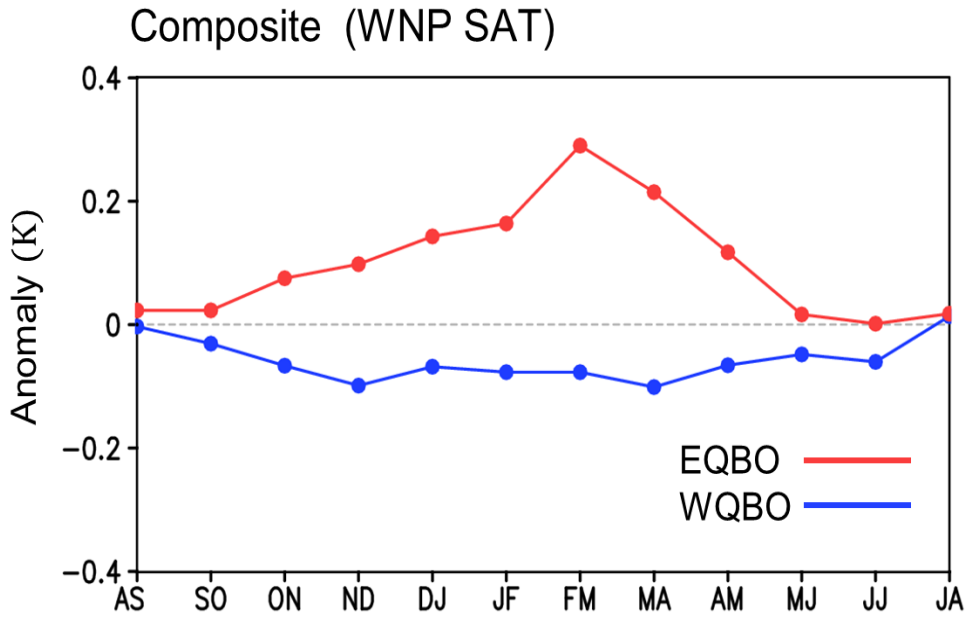

Figure 3.8. The composite of the area-averaged SAT anomaly over the East Asia and western North Pacific (WNP) for the EQBO (red line) and WQBO (blue line) phases.

What causes the QBO-East Asia teleconnection in FM? As addressed earlier, the QBO impact on SAT anomaly can be mediated by the AO induced by the polar vortex change (e.g., Gray et al. 2018; Haynes et al. 2021). Figure 3.9b presents the February-March (FM)-mean SAT anomaly regressed onto the FM-mean QBO index but removing AO signal. The overall regression pattern is quite similar to Fig. 3.9a, which is identical to Fig. 3.6g, even the AO-related SAT anomaly is linearly removed. Here the AO-related SAT anomaly is defined by regressing SAT

anomaly onto the two-month running averaged AO index. The first two figures are almost identical in East Asia. A discernible difference, resembling the SAT anomaly associated with negative AO, is observed only in northern Eurasia and eastern North America (Fig. 3.8c). This result indicates that the QBO-related SAT anomaly shown in Fig. 3.9a (or Fig. 3.6g) is not due to the polar vortex response.

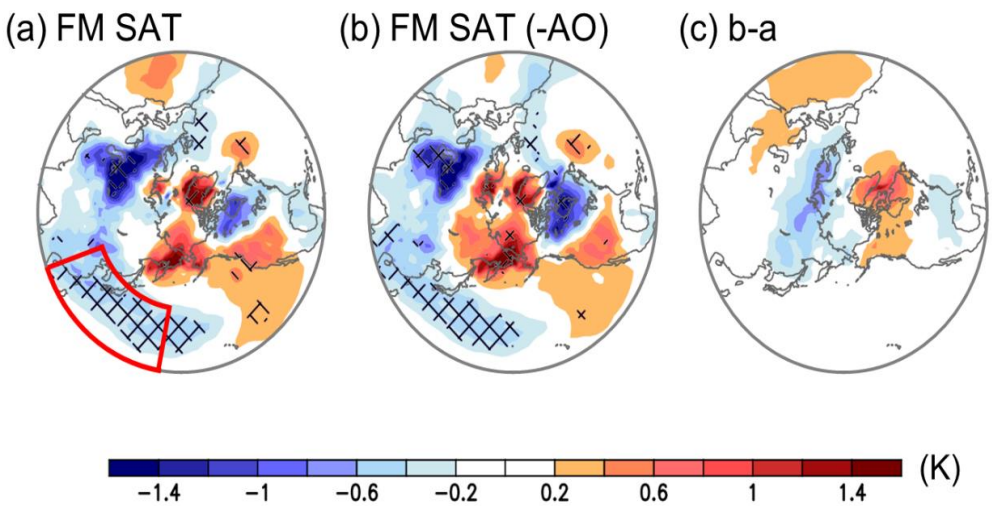

Figure 3.9. (a) The FM-mean SAT anomaly regressed onto the FM-mean QBO index (shading; K), (b) same as (a) but after removing arctic oscillation (AO)-related SAT anomaly, (c) its difference from (a). The values which are statistically significant at the 95% confidence level are cross-hatched. The red box in (a) denotes the WNP region. Note that (a) is identical to Fig. 3.6g, and shown here for a direct comparison.

The similar results are found when only the satellite era (since 1979) is considered. Figure 3.10a presents the SAT anomaly over East Asia regressed onto the QBO index in FM. Here, the maximum/minimum values of the color bar are only the half of Fig. 3.6. Statistically significant values are observed from the east coast of China to the western Japan. The in-situ measurements show even larger values than reanalysis data (Fig. 3.10a) with a higher significance level (Fig. 3.10b), revealing a robust QBO-SAT relationship. The QBO-East Asia teleconnection, shown in Figs. 3.6g, 3.9a, and 3.10, is not sensitive to the choice of the QBO index.

Because the East Asian SAT is influenced by the ENSO (Wang et al., 2000), the relative importance of the QBO-induced East Asian SAT change to the ENSO-induced change is further quantified. Figure 3.11a shows the correlation coefficients of the East Asian SAT with the ENSO and QBO indices. A statistically significant correlation with the ENSO (black filled dots) appears in autumn and winter (August–October and December–February). A maximum positive correlation is found in December–January with a correlation coefficient (r) of 0.31. As winter turns into spring, the ENSO impact weakens whereas the QBO impact gradually increases (cf. black and red filled dots). A significant negative QBO-East Asian SAT correlation is observed in late winter and early

spring (January–April). This result indicates that the QBO plays a more important role in modulating the late-winter East Asian SAT anomaly than the ENSO.

Here it should be stated that the QBO and ENSO have essentially no correlation in cold season ($r = -0.08$ in DJ and $r = -0.05$ in FM). Whether the ENSO signal is linearly removed or not, the FM and March–April (MA) correlation coefficients of the QBO-East Asian SAT remain high ($r = -0.41$).

The above results do not necessarily indicate a causal relationship. To examine a possible causality, a lead-lag correlation of the two-month running mean QBO index to the FM-mean East Asian SAT anomaly is computed in Fig. 3.11b. Statistically significant correlations are observed from lag −2 (DJ) to 1 month (MA). The extended correlations over three months result from the long-term memory of the QBO wind (see 70 hPa wind in Fig. 3.15a). This makes it difficult to determine the optimal time lag of the lead-lag relationship. A significant causal relationship is identified in January–February (JF; cross in Fig. 3.11b). It indicates that the JF-mean QBO index has a causal relationship with the East Asian SAT anomaly in FM at a one-month lag.

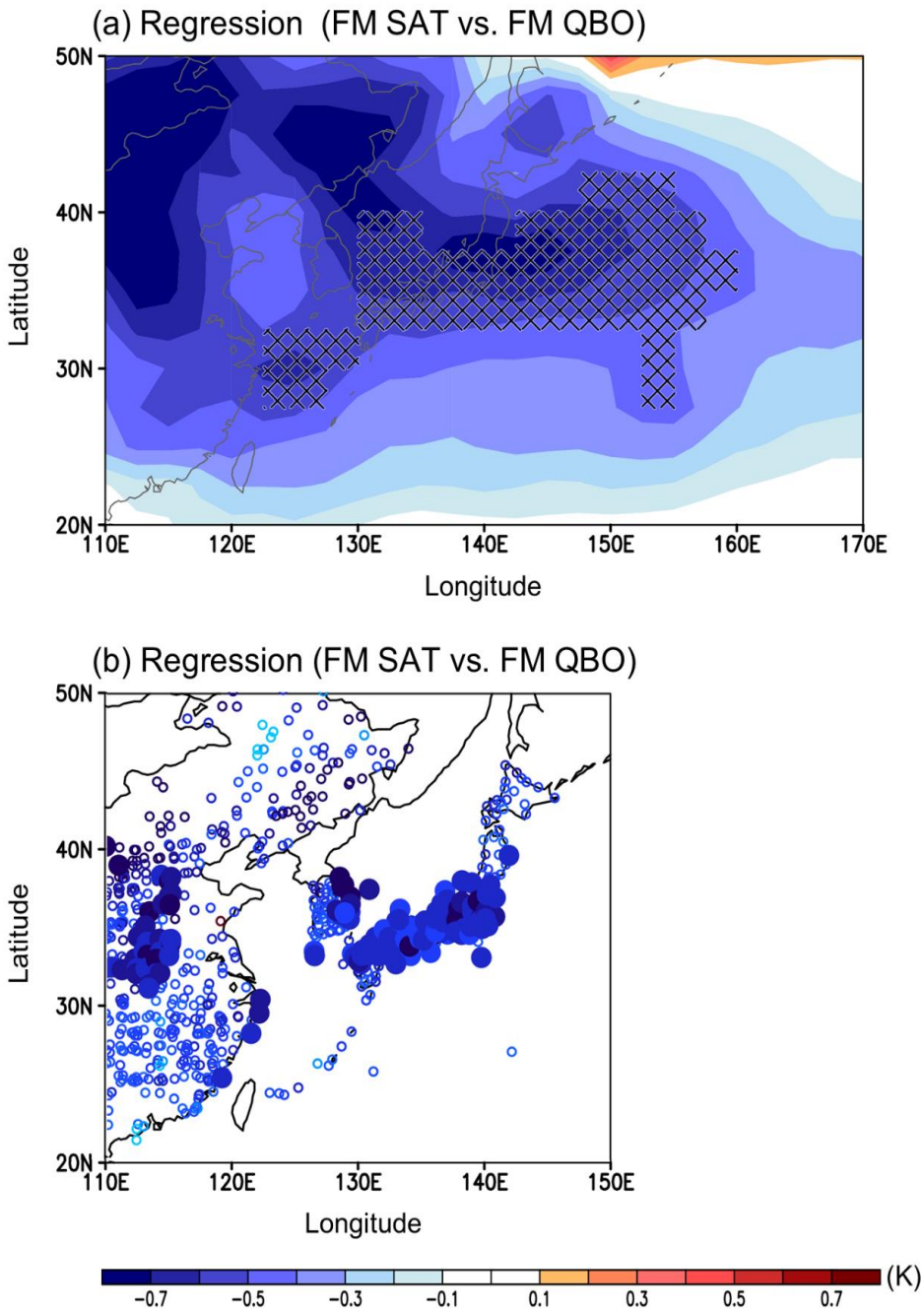

Figure 3.10. (a) The FM-mean SAT anomaly in East Asia regressed onto the FM-mean QBO index during the satellite era (August 1979 – July 2016; 37 years). (b) same as (a) but for the in-situ measurements over East Asia. The cross-hatched area in (a) and the filled dots in (b) denote the values which are statistically significant at the 95% confidence level.

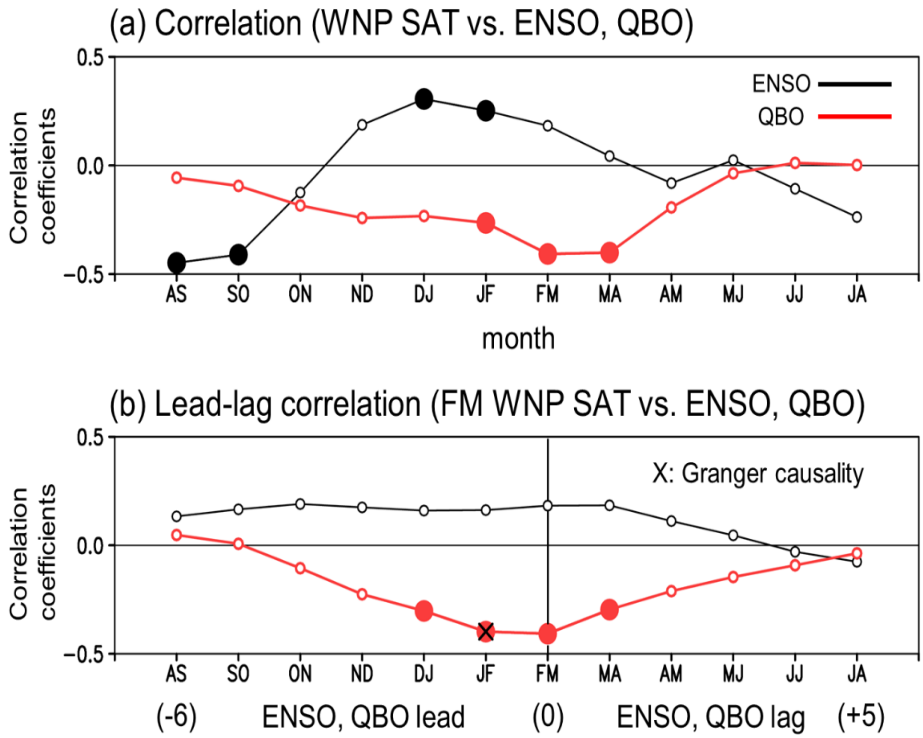

Figure 3.11. (a) Correlations between the East Asian and western North Pacific (WNP) SAT anomaly and the two dominant modes of tropical climate variability, QBO (red) and ENSO (black). (b) Lead-lag correlations of the FM-mean WNP SAT anomaly against the QBO and ENSO indices. The filled dots in (a,b) denote the values which are statistically significant at the 95% confidence level. Cross in (b) indicates the statistically significant Granger causality at the 95% confidence level.

Figure 3.12a shows the simultaneous regression values between QBO and SAT over the Korean Peninsula for all months. Here, white circles indicate statistically significant relationships. The QBO and Korean SAT have a significant negative relationship in March. This means that if the QBO index is positive (WQBO), the SAT over the Korean Peninsula becomes colder than normal, and when the QBO index is

negative (EQBO), the SAT becomes warmer than the normal years. This relationship is unique to March. The distribution of the relationship between QBO and SAT in March is evident in most regions except for the west side and some island regions (Fig. 3.13a). A distinct negative relationship is mainly distributed in the southeast of the Korean Peninsula.

In order to investigate the extent to how much the QBO precedes the relationship with the Korean SAT, a lagged correlation is investigated from each month up to 5 months (Fig. 3.12b). MAR-1 lag month represents the correlation coefficient of February QBO and March SAT. QBO shows a significant lagged relationship with the Korean SAT in March from one month ago. On the other hand, there is no significant relationship in any lagged relationship in the rest seasons. The Korean SAT in March has a significant negative relationship not only with the QBO of March (Fig. 3.12a) but also with the QBO of February (Fig. 3.12b).

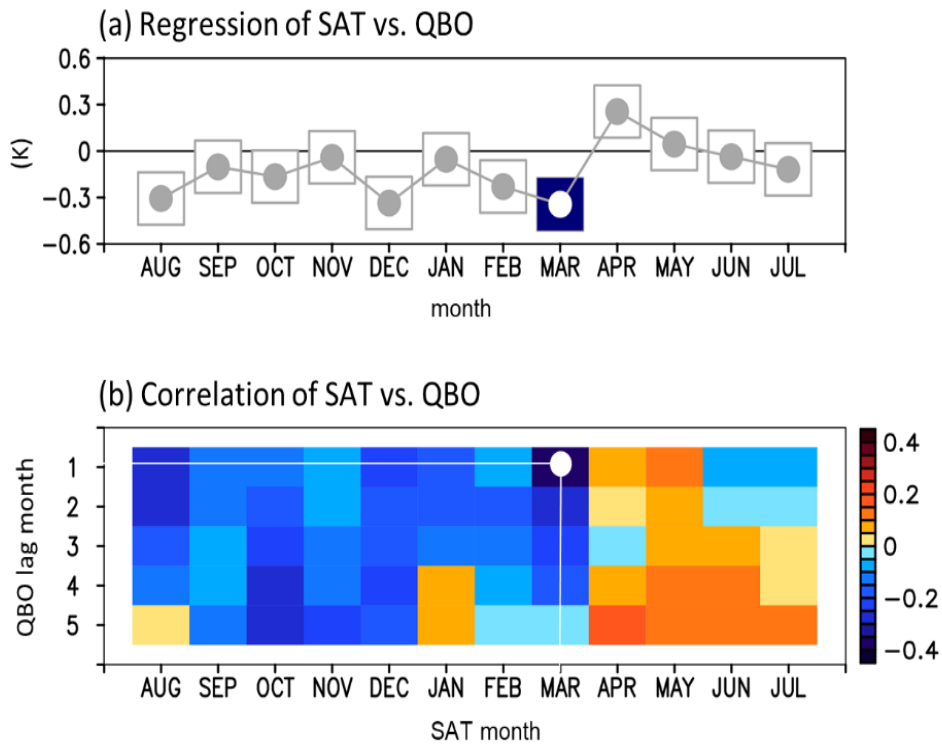

Figure 3.12. (a) Regression between the Korean SAT and the QBO. (b) Lagged correlation between the SAT over the Korean Peninsula and the QBO. The white circle indicates the statistically significant coefficient at the 95% confidence level. Units of the regression coefficients in (a) are converted into Kelvin by multiplying the standard deviation of the QBO. The QBO lag month at y-axis in (b) denotes the QBO lag with respect to the SAT over the Korean Peninsula. For instance, MAR-1 lag month (white circle in (b)) indicates the correlation between the March SAT over the Korean Peninsula and the February QBO.

It can be seen that the distribution of the delay relationship is also very similar to the result of simultaneous regression analysis (Fig. 3.13a). A distinct negative relationship is mainly distributed in the southeast of the Korean Peninsula.

The causality of the simultaneous and lagged relationships

shown in the simple regression analysis was estimated through the Granger causality test (Fig. 3.13c). As a result of considering the delay period of up to 5 months (Mg*=5), the Granger causal relationship appears only between the QBO in February and the Korean SAT in March, indicating that QBO may play an important role in predicting the Korean SAT in March.

In addition, the spatial distribution of the significant causal relationship is mainly confined to the southeast of the Korean Peninsula (Fig. 3.13c). This is somewhat different from the fact that QBO's influence on the early winter SAT is concentrated in the northern regions of the Eurasian continent (Thompson et al., 2002), implying that the QBO may influence the Korean SAT in March through different pathway.

The Korean SAT is known to be also influenced by ENSO (Wang et al., 2000; Park et al., 2018). Thus, the above results may include the effect of ENSO as a third factor (Geweke, 1984). In order to exclude the ENSO’s effect, the causal relationship between the QBO and the Korean SAT is re-confirmed by using the partial Granger causality test.

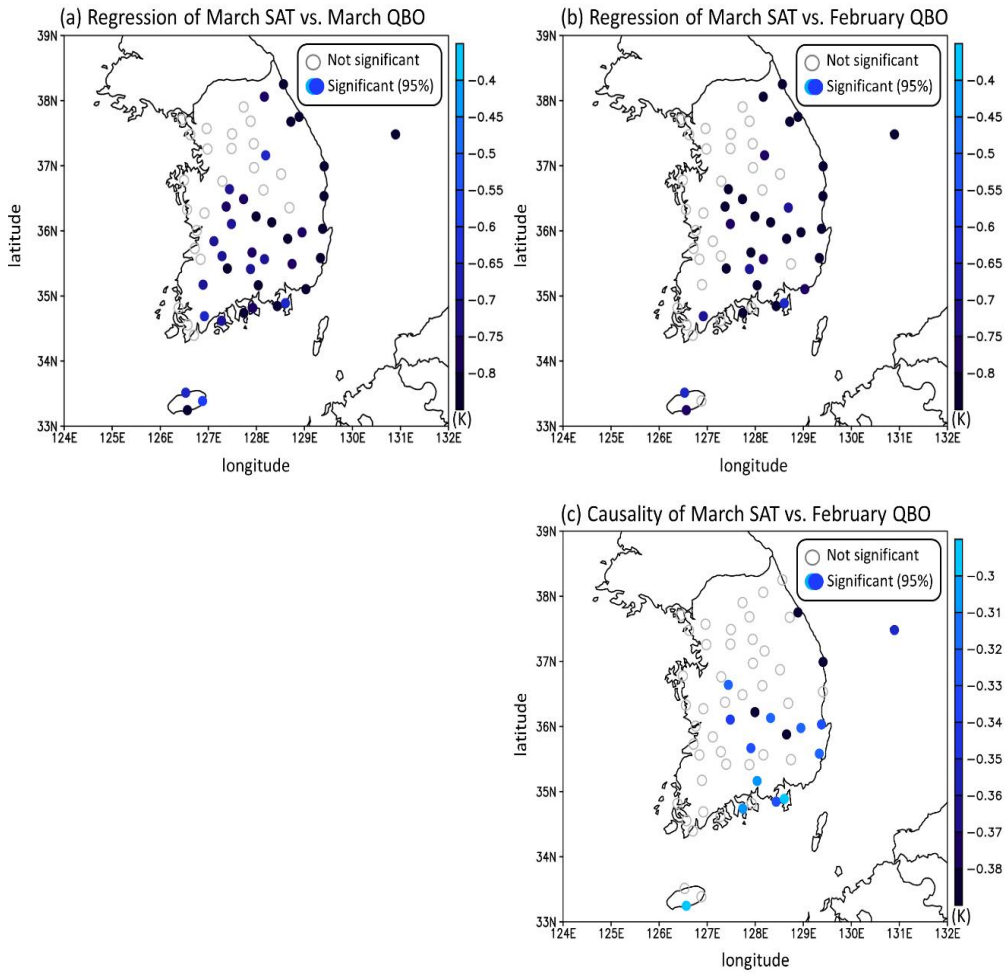

Figure 3.13. (a) Regression between the SAT over the Korean Peninsula and the QBO in March. (b) Same as (a) but for the February QBO. (c) The Granger causality between the SAT over the Korean Peninsula in March and the QBO in February. Blue colored circles indicate the statistically significant regressions at the 95% confidence level. Units of the regression coefficients are converted into Kelvin by multiplying the standard deviation of the QBO.

Figure 3.14a shows the distribution of partial Granger causality between QBO and Korean SAT. in late winter. The distribution is similar to the conventional causal relationship results mentioned above (cf. Fig. 3.13c and Fig. 3.14a), and the number of KMA stations showing the causality slightly increased from 17 (Fig. 3.13c) to 22 (Fig. 3.14a). It was found that the additional explained variance of the regression model including QBO (Eq. 11) has improved by about 10% compared to the regression model (Eq. 9), explaining the SAT with the SAT and ENSO information. Furthermore, the number 22 showing the causality is the same number as when ENSO is not taken into account. It means that QBO's influence on the Korean SAT in March is robust regardless of ENSO.

Figure 3.14b shows the partial Granger causal relationship between ENSO and Korean SAT in late winter. Compared to QBO, the effect of the ENSO is relatively weak. The number of KMA stations showing the causality slightly is only 6, and the additional explained variance of the regression is only 1%. This is to less robust than the additional explained variance of the regression of the ENSO regression in December, which could provide 22.18% additional explained variance (Park et al., 2018). These above results suggest that ENSO is a relatively important in early winter (Park et al., 2018) but the QBO is relatively important in late winter.

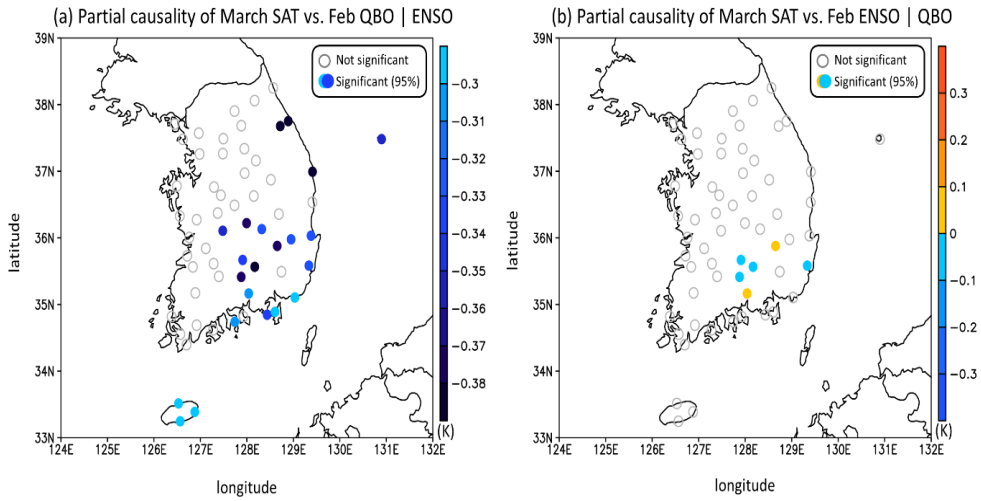

Figure 3.14. Same as Fig. 3.13c but for the partial Granger causality: (a) the QBO Granger-causes the SAT over the Korean Peninsula when conditioned the ENSO's effect and (b) ENSO Granger-causes the SAT over the Korean Peninsula when conditioned the QBO's effect. Units of the regression coefficients are converted into Kelvin by multiplying the standard deviation of the (a) QBO and (b) ENSO.

3.2.2. Subtropical route on East Asia

It is confirmed that the distribution of causality between QBO and SAT of the Korean Peninsula was mainly concentrated in the southeast of the Korean Peninsula (Figs. 3.13-3.14). In this section, we investigate the QBO-induced tropospheric large-scale circulation changes from stratosphere to the surface around the East Asia.

Figure 3.15a presents the lead-lag correlation coefficients between the two-month running averaged QBO wind at each pressure

level and the FM-mean East Asia and western North Pacific (WNP) SAT anomaly. At lag 0, a statistically significant positive correlation is found at 15-hPa and 20-hPa pressure levels (see the filled dots in the right panel). Such positive correlations at and above 20 hPa, opposing the negative correlations at and below 50 hPa, are consistent with the downward propagation of the QBO wind. When considering time lag from −6 to 5 months, a downward propagation of a pair of positive and negative values is clearly captured. Owing to the slow descent of the QBO wind, the earlier QBO phase lingers in the lower stratosphere when the new QBO phase appears in the upper stratosphere.

The sector-mean circulation response to the QBO is illustrated in Fig. 3.15b. Specifically, the FM-mean zonal wind anomaly averaged over the APJ longitudes (120°–150°E) is regressed onto the FM-mean QBO index. In the tropics, a two-fold structure is evident, which reveals the QBO structure as shown in Fig. 3.15a. A statistically significant positive relationship also appears in high latitudes. This high-latitude response with a stronger polar vortex during the QBO westerly phase is similar to the Holton-Tan effect (Holton and Tan, 1980). However, the polar vortex change does not extend into the troposphere in FM. This differs from the Holton-Tan effect in early winter, which is well connected to the troposphere (Gray et al., 2018).

Figure 3.15b shows that a significant zonal wind anomaly in the

subtropics extends to the mid-troposphere. This downward arching of the zonal wind anomaly is connected to the APJ and the tropospheric circulation anomalies (Garfinkel and Hartmann, 2011a, b; Rao et al., 2020). When the QBO wind is westerly, anomalous westerly and easterly winds appear on the southern and northern flanks of the APJ (black contours), indicating an equatorward shift of the APJ during the QBO westerly phase. Although not presented here, this APJ change is weaker in other seasons. When the FM-mean APJ wind anomaly is regressed onto the QBO index with a time lag, the horseshoe-shaped wind anomaly is also found at a one-month lag to the JF-mean QBO index as well as at a one-month lead to the MA-mean QBO index (Fig. 3.16). This result indicates that the FM-mean APJ wind anomaly is likely influenced by the QBO within one-month time lag.

Both the latitudinal displacement and the intensity change of the APJ are closely related to the WNP SAT change (e.g., Yang et al., 2002; Luo and Zhang, 2015). Yang et al. (2002) proposed that a stronger APJ is related to a colder WNP SAT anomaly via an intensification of the regional circulations over eastern Eurasia and WNP such as the deepening of the East Asian trough and the Aleutian low. Luo and Zhang (2015) further showed that the APJ equatorward shift is closely related to the colder East Asian SAT anomaly on the interannual time scale. These studies suggested that the QBO-East Asian SAT relationship is

likely mediated by the APJ shift. Earlier studies have separately examined the QBO-APJ and APJ-East Asian SAT relationships in winter. Here, we combine these two relationships and extend them to the late winter and early spring.

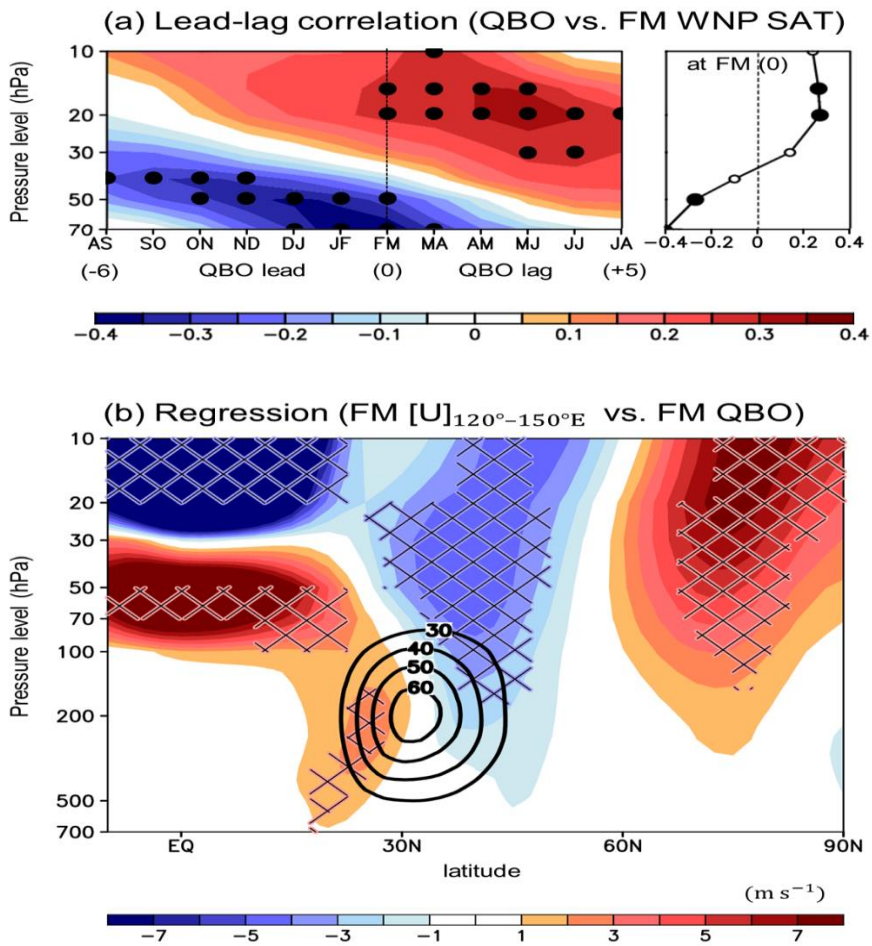

Figure 3.15. (a) The lead-lag correlation coefficients between the two-month running averaged QBO wind at each pressure level and the FM WNP SAT anomaly. The vertical profile at lag 0 is separately shown on the right-hand side. (b) The latitude-height section of the FM-mean zonal wind anomaly averaged over the Asian-Pacific jet (APJ) core (120°–150°E) regressed onto the FM-mean QBO index (shading; $\mathrm{m\ s^{-1}}$). The filled dots in (a) and cross-hatched area in (b) denote the statistically significant values at the 95% confidence level. The thick black contour in (b) indicates the climatological APJ.

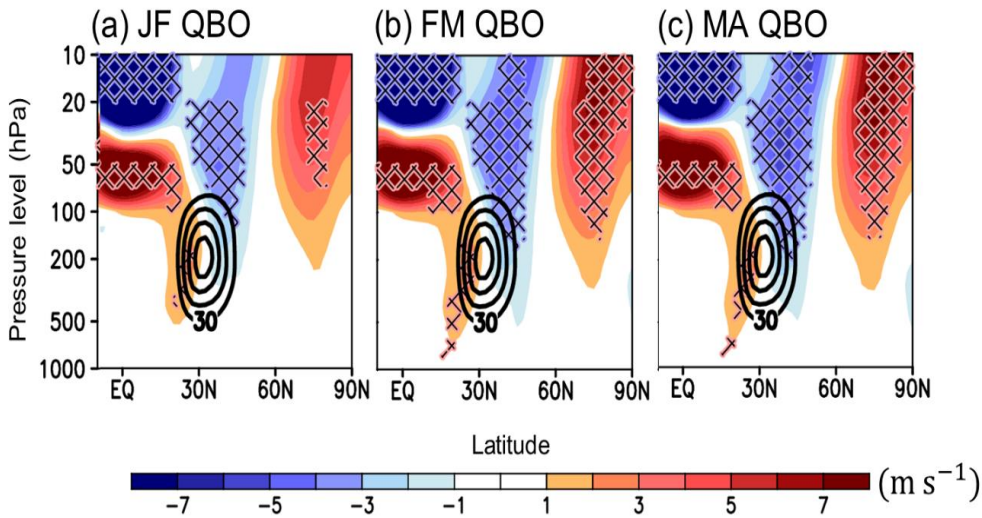

Figure 3.16. The latitude-height section of the FM-mean zonal wind anomaly averaged over the APJ core (120°–150°E) regressed onto the two-month running averaged QBO index from lag -1 to +1 month (shading; $\mathrm{m\,s^{-1}}$). The values which are statistically significant at the 95% confidence level are cross-hatched. The thick black contour indicates the climatological FM-mean APJ.

Figure 3.17a shows the regression of the 250-hPa zonal wind anomaly onto the QBO index in FM. The thick black contours indicate the climatological APJ (see also black contours in Fig. 3.15b). A dipole pattern appears around the jet core. When the QBO wind is westerly, the zonal wind is enhanced on the equatorward side of the APJ from upstream to downstream regions. Such a zonally elongated and equatorward-shifted APJ in the QBO westerly phase is consistent with that of Garfinkel and Hartmann (2011a, b). The causality in Figs. 3.11-14 is closely related to the horseshoe-shaped downward-arching QBO wind anomaly. Figure 3.18 shows the Granger causality of the FM-mean

Asian-Pacific jet (APJ) wind against the JF-mean QBO index. A causality is again found in the subtropical troposphere. This result confirms that the downward-arching wind anomaly shown in Fig. 3.15b is caused by the QBO with a one-month lag. It supports that the QBO westerly in the equatorial lower stratosphere drives cold SAT anomaly over East Asia and WNP via the APJ change in FM.

To examine the SAT and near-surface circulation anomalies associated with the latitudinal displacement of the APJ, the SAT and 1000-hPa horizontal wind anomalies are regressed onto the APJ-shift index in FM (Fig. 3.17b). Since the 250-hPa zonal wind anomaly related to the QBO index is statistically significant only in the southern part of the climatological APJ center (Figs. 3.15b and 3.17a), the APJ-shift index is defined as the area-averaged 250-hPa zonal wind over the southern part of the climatological APJ (120°–150°E, 22°–32°N). The positive APJ shift index indicates an equatorward shift of the APJ. Figure 3.17b shows a robust cyclonic circulation anomaly in the subtropical North Pacific and an anticyclonic circulation anomaly in northern Eurasia when the APJ moves to the south (Lee et al., 2020). Similar circulation anomalies are also evident in the sea-level pressure anomalies (not shown), as shown in Gray et al. (2018).

The associated SAT anomaly shown in Fig. 3.17b closely resembles Fig. 3.6g over the North Pacific basin. This resemblance can

be explained by the temperature advection. The northwesterly winds in the subtropics and northeasterly winds in the mid-latitudes (see arrows) transport cold air from the continent or the high-latitude ocean to the East Asia and WNP region (red box). The regression of the temperature advection at 975 hPa is indeed qualitatively similar to the SAT regression onto the APJ-shift index (not shown).

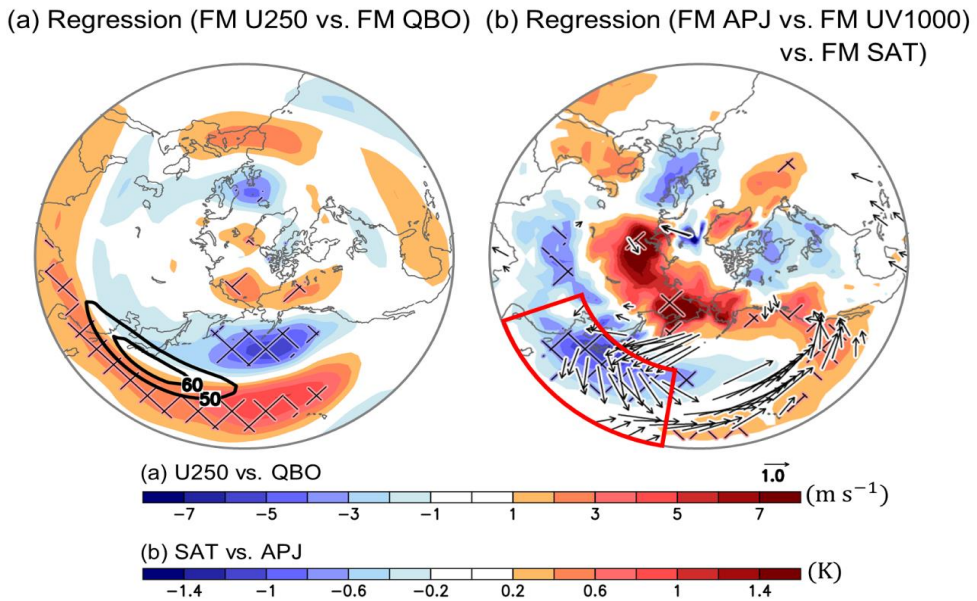

Figure 3.17. (a) The FM-mean zonal wind anomaly at 250 hPa regressed onto the FM-mean QBO index (shading; $\mathrm{m\,s^{-1}}$). (b) The FM-mean SAT (shading; K) and horizontal wind anomalies at 1000 hPa (arrows; $\mathrm{m\,s^{-1}}$, only significant values are displayed) regressed onto the FM-mean APJ-shift index. Here, the APJ-shift index is defined as the area-averaged 250-hPa zonal wind over the equatorward side of the climatological APJ (120°–150°E, 22°–32°N). The cross-hatched area denotes the statistically significant value at the 95% confidence level. The thick black contour in (a) and red box in (b) indicate the climatological APJ and WNP region, respectively.

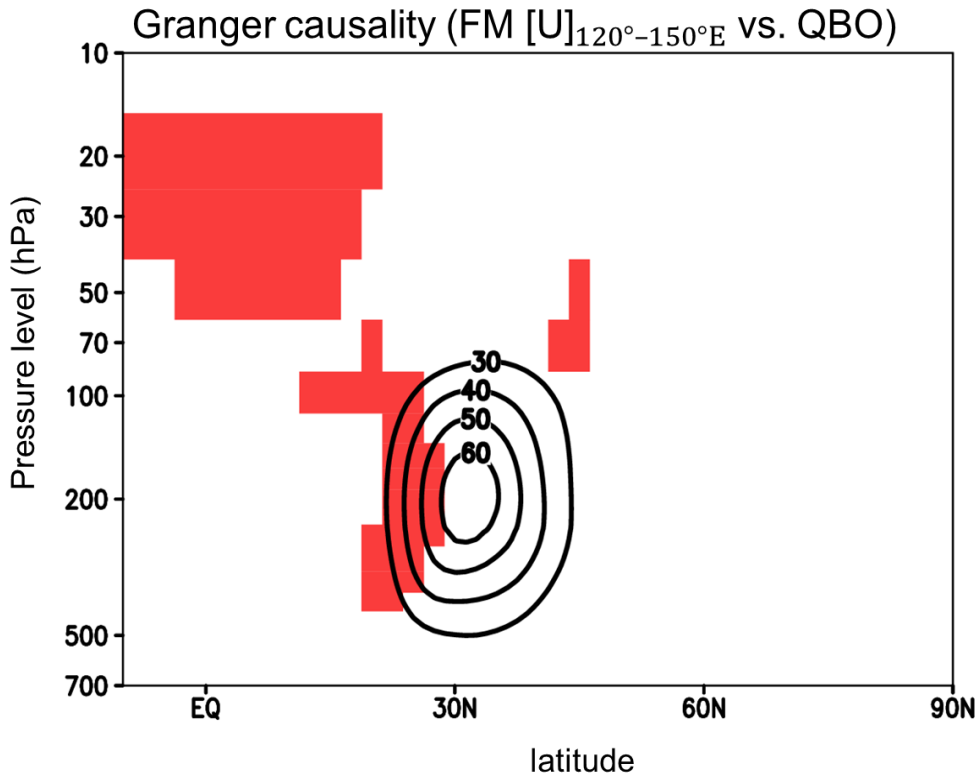

Figure 3.18. Granger causality between the FM-mean zonal wind anomaly averaged over the APJ core and the JF-mean QBO index at the 95% confidence level (red shaded area). The thick black contour indicates the climatological FM-mean APJ.

The Granger causality test confirms that the QBO downward coupling is mainly connected to the subtropical route among three possible routes, i.e., polar, subtropical, and tropical route (Fig. 3.18). Figure 3.18 shows that only the statistically significant signal is observed in tropics, not tropics and polar region. It indicates the subtropical zonal wind change shown in Fig. 3.17b is caused by the QBO.

Figure 3.19a shows the linear regression values between February QBO and March sea level pressure (SLP). The significant SLP

anomaly appears in the eastern Eurasia and the North Pacific regions. In the case of WQBO, the atmospheric circulation anomalies consist of a positive (+) SLP anomaly in eastern Eurasia and a negative (-) SLP anomaly in the south of the Aleutian Low region. The negative SLP anomaly south of the center of the Aleutian Low is consistent with the North Pacific circulation response to the QBO (Ruti et al., 2006; Garfinkel and Hartmann, 2011a, b). The mean value of the center of this anomaly is -112 Pa (160°E–150°W, 30°–60°N). It becomes the largest value around December and January (not shown).

Rao et al. (2020) also showed that this circulation response to the QBO is evident over the North Pacific region by comparison of the climate models, which is driven by the descending QBO momentum anomaly from the stratosphere to the troposphere near 20°–40°N.

Figure 3.19b shows the linear regression between the QBO in February and UV1000 (arrow) and SAT (color) in March. The significant zonal wind anomaly and thus the SAT anomaly appear near the Korean Peninsula, which is the region between the significant circulation anomalies over the Aleutian Low and the eastern part of Eurasia. This means that the significant temperature advection is induced by the large-scale circulation anomalies around the Korean Peninsula. For instance, during the WQBO, a strong northeasterly wind anomaly blows into the Korean Peninsula, bringing a relatively cold SAT anomaly from

the high-latitude. Although no results were shown, the budget analysis of the temperature at 975 hPa confirms that the horizontal temperature advection significantly contributes to the SAT change in the Korean Peninsula.

During EQBO, a strong southwesterly wind anomaly blows into the Korean Peninsula and thus induces anomalous warming over the Korean Peninsula. In other words, the QBO in February-March affects the Korean Peninsula SAT by inducing the large-scale circulation change around the Korean Peninsula. Thus, the significant relationship between the QBO and the Korean SAT can be seen in the southeastern side of the Korean Peninsula (Figs. 3.13, 3.14).

To reconfirm whether the above-mentioned physical process is closely related to SAT fluctuations in the Korean Peninsula, the same analysis is conducted in all seasons, which did not show any significant relationship between QBO and Korean SAT (Fig. 3.20). In December and February, large-scale circulation changes are also observed around the Korean Peninsula, but the horizontal wind anomaly is more confined to the coastal area of China rather than the Korean Peninsula, resulting in no temperature advection to the Korean Peninsula. In the other months, the similar reason leads to the no causality between the QBO and Korean SAT. In other words, The FM-mean QBO influences the Korean SAT by modulating the large-scale circulation field around the Korean Peninsula,

but in other months, the QBO has little effect in causing large-scale circulation fluctuations that can directly affect the Korean SAT.

The spatial distribution of the large-scale circulation and zonal wind anomalies also show that the evident anomalies are located mainly in the southeastern part of the Korean Peninsula (not shown in the figure). This distribution is consistent with the distribution of the causal relationship between QBO and the Korean SAT (Figs. 3.13, 3.14), re-confirming that the large-scale circulation anomaly induced by the QBO plays an important role in the relationship between the QBO and the Korean SAT. All the above analyses showed qualitatively consistent results even when the average period is changed to from one-month to three-month.

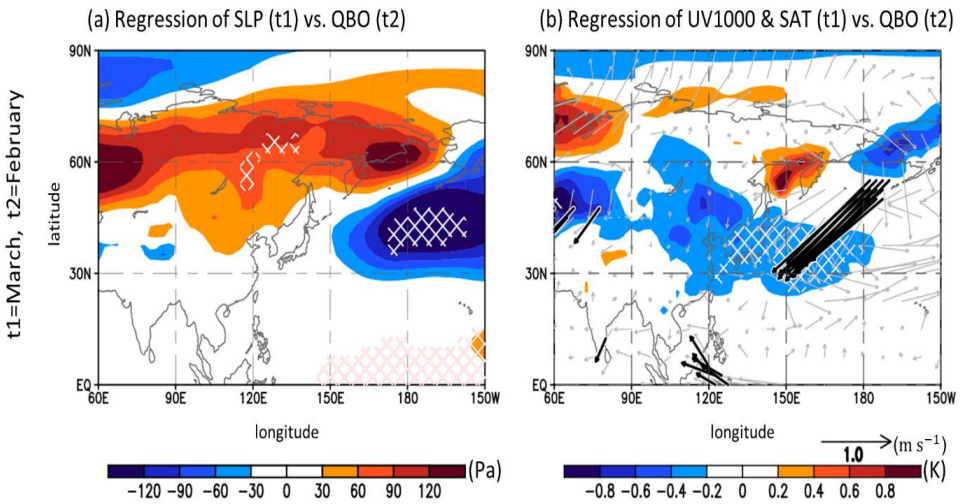

Figure 3.19. (a) March sea level pressure (SLP), (b) March horizontal wind at 1000hPa (UV1000) (arrows) and March SAT (shaded) regressed onto the February QBO index. The hatched areas in (a, b) and thick black arrows in (b) denote the statistically significant regressions at the 95% confidence level based on Student's t-test. Units of the regression coefficients are converted into Pa in (a), Kelvin and $\mathrm{m\ s^{-1}}$in (b) by multiplying the standard deviation of the QBO, respectively.

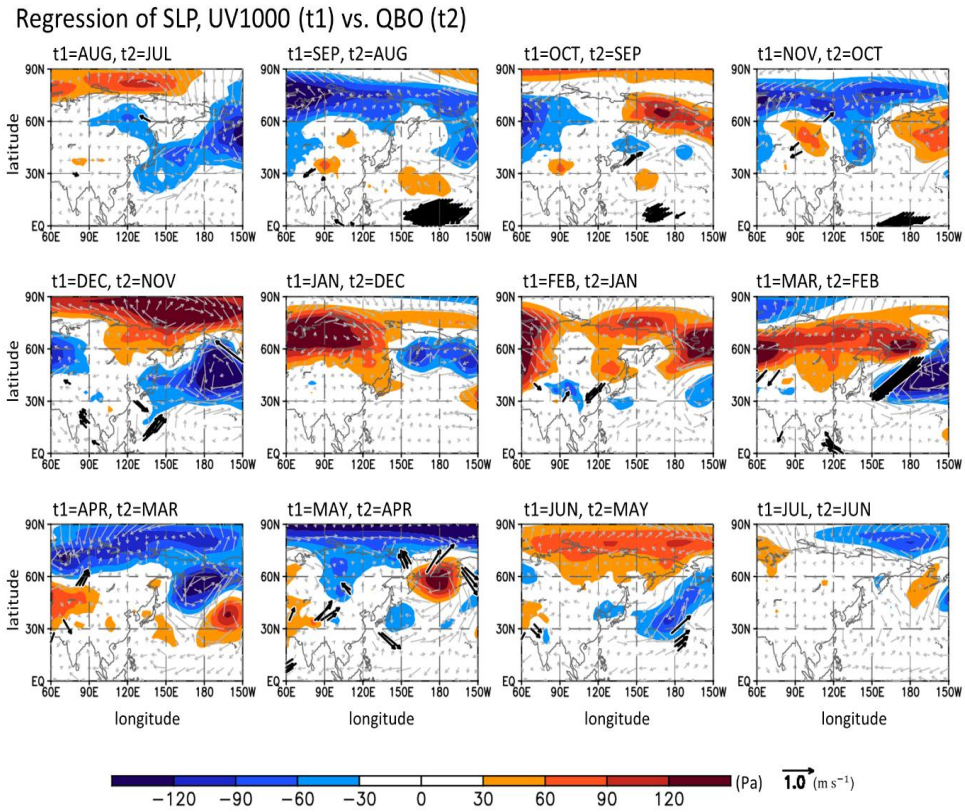

Figure 3.20. SLP (shaded), UV1000 (arrows) regressed onto the -1 lag month QBO index. For instance, the upper left panel indicates the SLP and UV1000 in August regressed on QBO index in July. Thick black arrows denote the statistically significant regressions at the 95% confidence level based on Student's t-test. Units of the regression coefficients are converted into Pa and $\mathrm{m\ s^{-1}}$. by multiplying the standard deviation of the QBO, respectively.

This strong QBO downward coupling shows a robust decadal variation (Fig. 3.21). Previous studies have shown that the QBO influence on the organized tropical convection (e.g., MJO) has a decadal variation (Klotzbach et al., 2019; Martin et al., 2021) and its influence has emerged only in recent decades. A similar decadal variation has also been reported for the Holton-Tan effect (Lu et al., 2014). Similar to these, the QBO-East Asian SAT relationship has emerged only in the last three decades. Figure 3.21a shows the 21-year running correlation between the QBO index and the East Asian SAT anomaly in February–March. A statistically significant correlation appears only since the 1990s. The same result is also found in JRA-55C (yellow line), indicating that this decadal variation is not an artifact of satellite data assimilation. In addition, the QBO-APJ relationship (Fig. 3.21b) shows a similar decadal change to the QBO-East Asian SAT relationship. A consistent decadal change supports the SAT response. This result suggests that the QBO downward coupling through the subtropical jet is not static but varies in time, possibly due to background flow change.

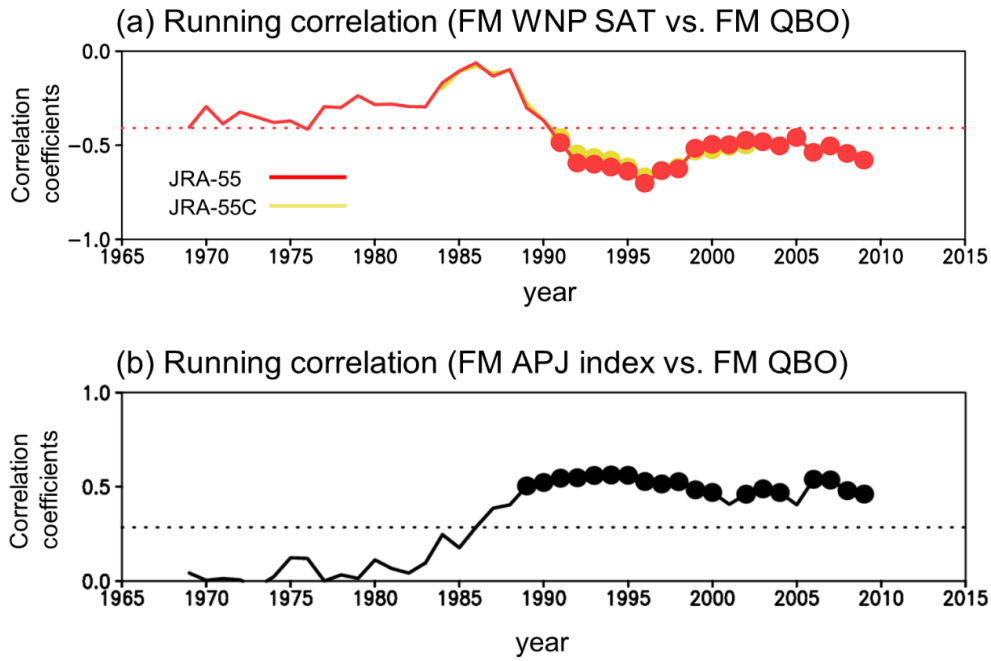

Figure 3.21. (a) 21-year running correlation between the FM-mean WNP SAT anomaly and the FM-mean QBO index, where the x-axis indicates the middle year of the 21-year moving window. Both JRA-55 (red) and JRA-55C (yellow) are used. (b) same as (a) but for the FM-mean APJ shift index and the FM-mean QBO index. The filled dots in (a,b) denote the values which are statistically significant at the 95% confidence level. The dotted lines in (a,b) denote the correlation coefficients over the whole analysis period.

3.3. Mechanisms with an idealized model experiment

3.3.1. Eddy changes in the downward coupling

As the role of eddies has been suggested (summarized in Fig. 3.22; Garfinkel and Hartmann, 2011a, b), the QBO-East Asia coupling observed in previous section can be attributed to the eddy-mean flow interaction. To examine a possible mechanism in more detail, the WQBO nudging and CTL experiment are conducted which are the simulations with and without the QBO-like zonal wind forcing (Section 3.1.5).

Although the model has no temperature profile in the stratosphere in the polar region, i.e., a poor representation of the atmospheric variability in the high latitudes, the downward arching zonal wind anomaly is qualitatively well reproduced by this simple dry dynamic core model (Fig. 3. 23). It implies that the QBO downward coupling is directly connected to the East Asian surface climate via the subtropical jet rather than through a high latitude (e.g., Holton-Tan effect). It is interesting point that this result is consistent with the Granger causality test showing the statistically significant causal relationship only appears in subtropics (cf. Fig. 3.23 and 3.18).

To confirm a possible role of eddy momentum flux convergence (EMFC) on such zonal wind anomaly, their vertical profile and budget analysis are investigated on each CTL and WQBO experiment (Fig. 3.24).

According to the time-mean of zonal-mean zonal momentum equation, EMFC can derive the westerly wind together with Coriolis force acting on the anomalous mean meridional wind. The role of eddies is confirmed in both cases (Figs. 3.24a and b). The center of the positive EMFC coincides with the jet core (cf. black contours and red shadings in Figs. 3.24a and b). The result becomes more pronounced at the core level of the jet (i.e., 250 hPa; red and black lines in Figs. 3.24c). This EMFC change is mainly attributed to the change of the high-frequency eddies (orange line in Fig. 3.24d). The change of eddies having a frequency higher than 7-day, shows a close relationship with the change of the jet, while that of the low frequency or mixed frequency eddies has little contribution to the change of the jet (cf. orange, blue, and gray lines). Similar results are also shown in the WQBO case (Figs. 3.24e and f). Furthermore, the shift of the jet (cf. black lines) can be explained by the eddies (cf. red lines). The above results indicate that eddies, particularly high-frequency eddies, have a key role on the QBO downward coupling.

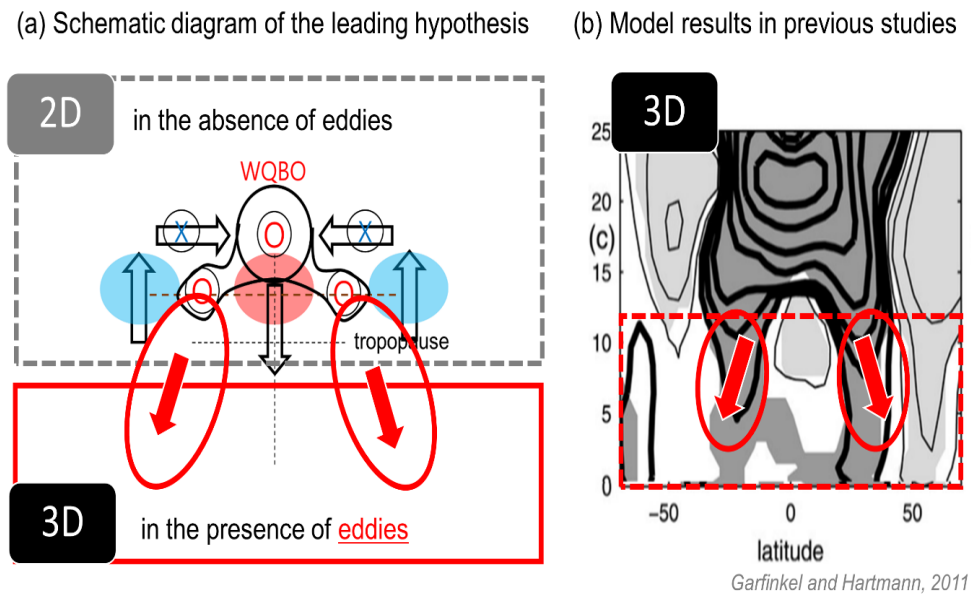

Figure 3.22. Leading hypothesis of the QBO downward coupling suggested in previous studies. (a) schematic diagram and (b) 3D simulation result indicating the role of eddies for the QBO downward coupling. The black contour and color shading in (a) denote the zonal-mean zonal wind and temperature anomalies associated to the WQBO phase. Black thick arrows denote the associated secondary circulations. Red arrows and circles in (a,b) denote the extended QBO downward coupling due to the presence of the eddies in 3D simulations.

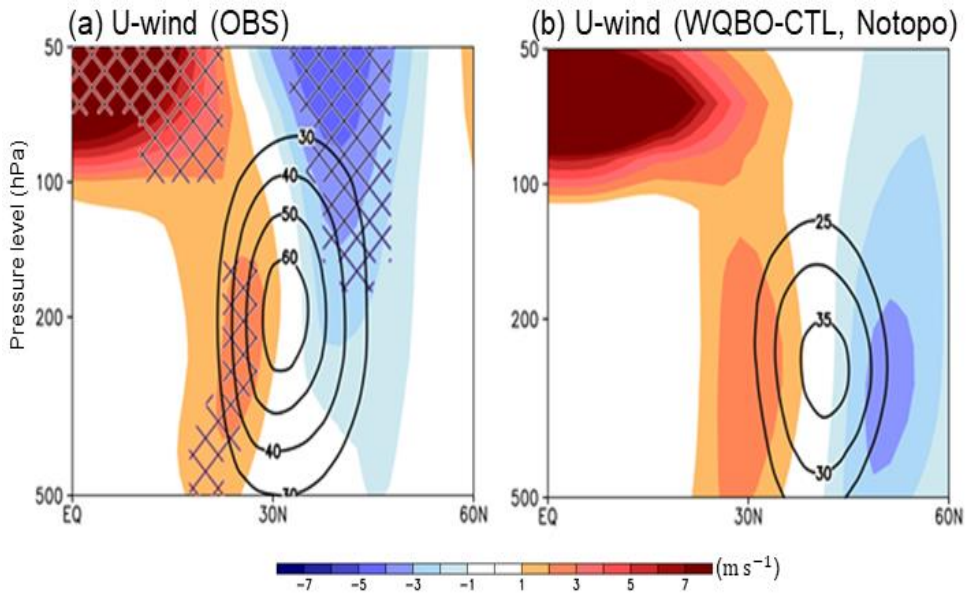

Figure 3.23. (a, b) The latitude-height section of the zonal-mean zonal wind (U-wind) response difference between the (a) W-EQBO in observation and (b) WQBO simulation and CTL simulations (WQBO-CTL) (shading; $\mathrm{m\,s^{-1}}$). The thick black contour in (a, b) indicates the climatological APJ. The cross-hatched area in (a) denote the statistically significant values at the 95% confidence level, note that it is same to Fig. 3.15(b) for a direct comparison.

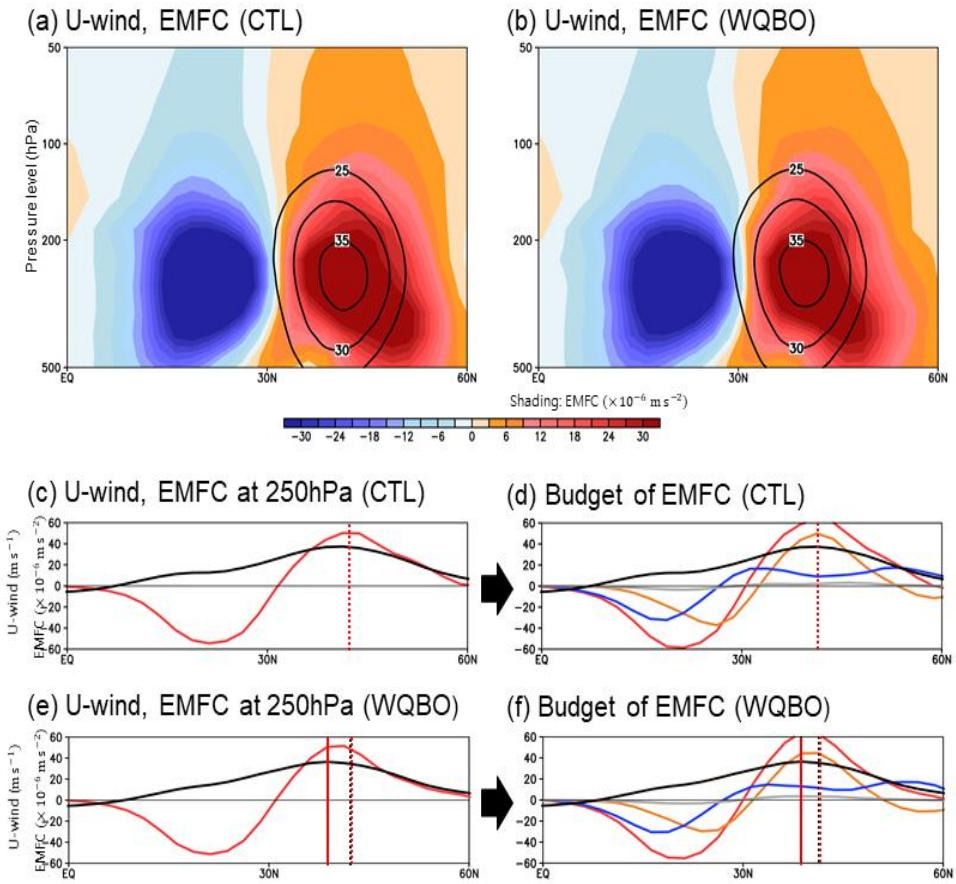

Figure 3.24. The response of the (a, b) U-wind (contour) and EMFC (shading) in (a) CTL and (b) WQBO (c, e) Same as (a, b) but for the at 250hPa where the jet core level in (c) CTL and (e) WQBO. (d, f) The budget analysis of the EMFC in (d) CTL and (f) WQBO. The vertical black and red lines represent the maximum latitude of the jet and EMFC, respectively. Orange, blue, and gray lines denote the high-frequency, low frequency, and mixed frequency components, respectively.

3.3.2. QBO-related stratospheric mean state change

How does QBO drive the downward coupling? To examine how the WQBO-related atmospheric background changes make the eddies, the time-evolution of the downward coupling is further investigated. 100-ensemble transient experiments are performed for 22 days at 50-day intervals from both CTL and WQBO. Thus, the dynamical processes in early stage of the QBO downward coupling, which are not seen in the time-averaged pattern (Section 3.3.1), can be obtained under the various initial conditions. Figure 3.25 shows the ensemble mean time evolution of the zonal wind difference between the WQBO-CTL. At an early stage of the time evolution, the zonal wind response is observed confined in the lower stratosphere and upper troposphere (shading). However, the zonal wind anomaly becomes stronger and extends downward to the troposphere.

The time-mean of zonal-mean zonal momentum equation in terms of the Euler mean represents that this zonal wind anomaly can be derived by the EMFC, which can be modulated by the refractive index. Figure 3.26 shows the refractive index (shading) and E-P flux (vector). During the downward coupling, the WQBO-related positive refractive index is robust in the equatorial lower stratosphere-upper troposphere (red shading in Fig. 3.26). Since eddies propagate to the regions of high

refractive index (Karoly and Hoskins, 1982), it leads to the equatorward and upward eddy propagation (vector in Fig. 3.26). At early stage, this eddy propagation is robust only in the upper troposphere, but the propagation becomes stronger and extends to the troposphere.

Such eddy propagation induces a horizontal eddy momentum and its convergence to the region. Figure 3.27 shows the time evolution of the eddy momentum flux (EMF; contour) and its convergence (EMFC). As expected, the positive EMF is observed in the upper troposphere at the early stage, leading to the positive EMFC to the poleward side of the maximum latitude. As the eddy propagation becomes stronger (Fig. 3.26), the resultant horizontal EMF and EMFC also becomes stronger (Fig. 3.27). The positive EMFC contribute to the westerly wind anomaly on the equatorward side of the jet (cf. red shadings in Figs. 3.27 and 3.25), and thus the downward zonal wind anomalies as the WQBO-related eddy propagation becomes strong.

Figure 3.28 explains how QBO-related stratospheric background state induces a positive refractive index in the lower subtropical stratosphere as depicted in Fig. 3.26. Since zonal wind is too weak in the early stage of the downward coupling, the positive refractive index (shading in Fig. 3.28a) is induced mainly by the positive meridional gradient of potential vorticity (i.e., PV gradient; contour in Fig. 3.28a), which is derived the westerly vertical wind shear and warm anomalies

associated with the WQBO (Fig. 3.28b). During the WQBO phase, the WQBO-related wind causes warm temperature anomaly just below the westerly wind shear level to maintain the thermal wind balance. This process is well reproduced in the idealized model experiment (Fig. 3.28). The changes of wind and temperature leads to the change of PV gradient as well as refractive index, resulting in the Rossby wave propagation change (Fig. 3.26). The anomalous equatorward and upward propagation of the Rossby waves derive the convergence of the E-P flux in the southern flank of the jet. The resultant EMFC induces the westerly wind anomaly in the southern flank of the jet.

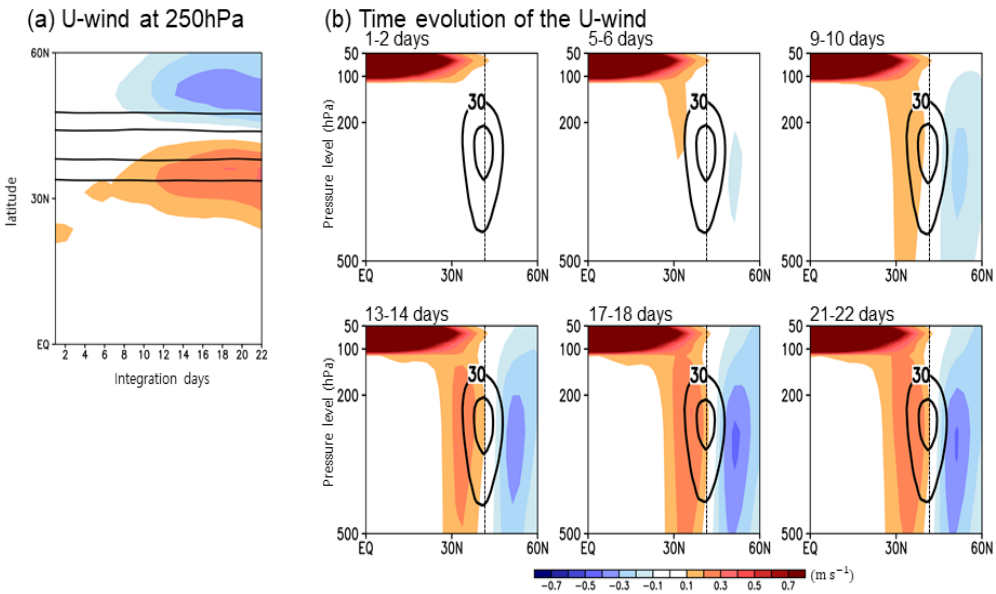

Figure 3.25. Time evolution of WQBO-CTL response of U-wind (a) at 250 hPa and (b) vertical profile of 2-day mean. The contour and vertical line represent the Jet core in CTL. Shading represents the WQBO response. The result is ensemble mean of 100 transient experiments.

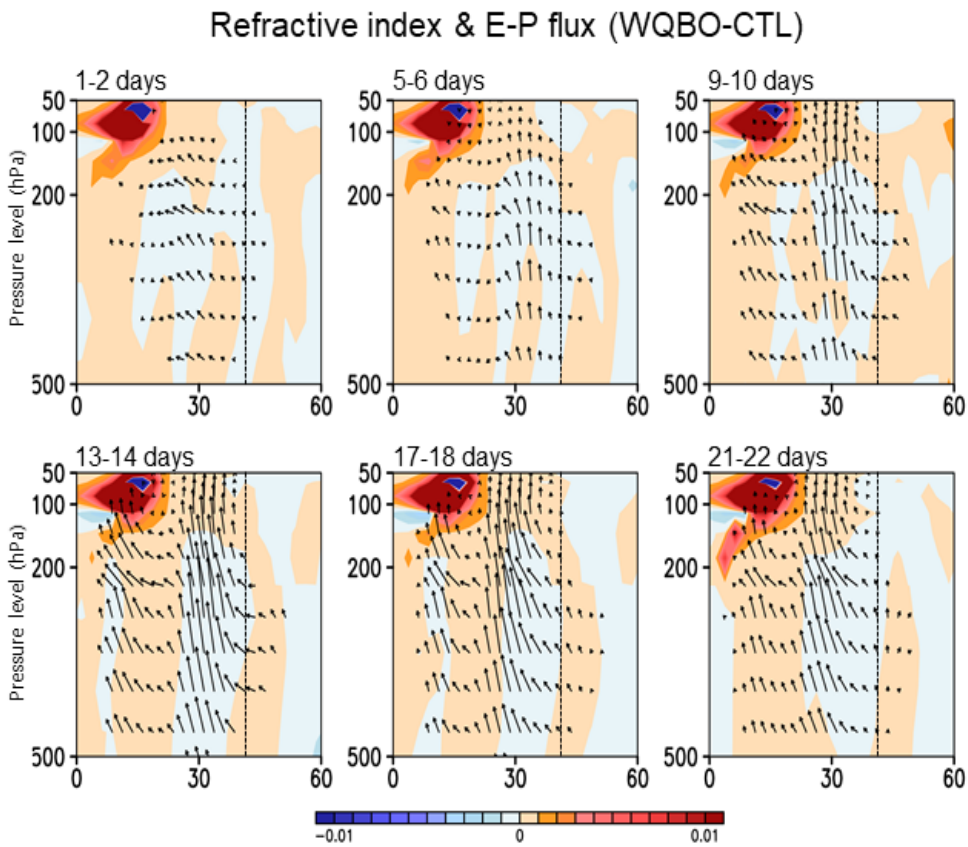

Figure 3.26. 2-day mean time evolution of WQBO-CTL response of refractive index (shading) and E-P flux (vector). The vertical line represents the Jet core in CTL. The result is ensemble mean of 100 transient experiments. The zonal-mean quasigeostrophic refractive index is calculated based on the zonal wavenumber: k = 7, zonal phase speed: c = 0m/s.

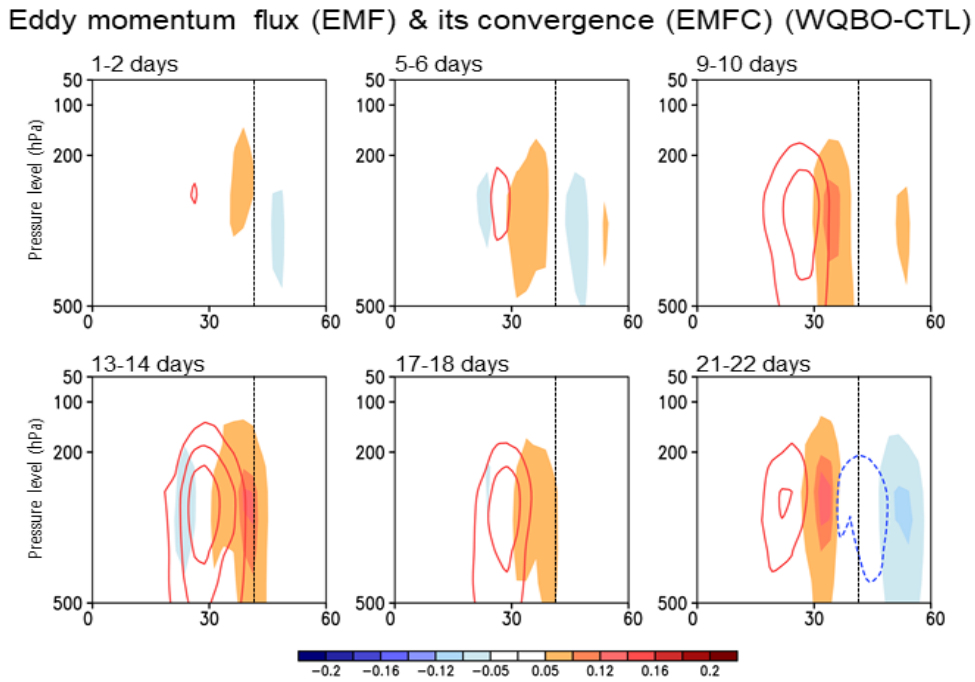

Figure 3.27. 2-day mean time evolution of WQBO-CTL response of Eddy momentum flux (EMF; contour) and its convergence (EMFC; shading). The vertical line represents the Jet core in CTL. The result is ensemble mean of 100 transient experiments.

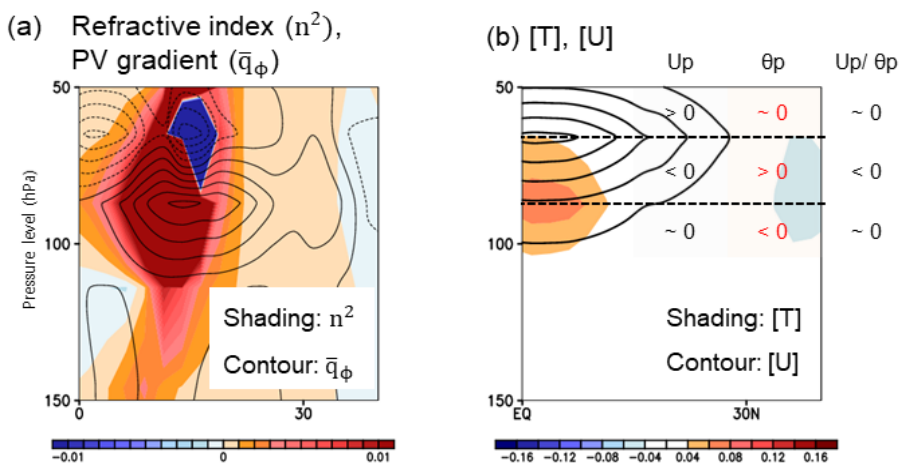

Figure 3.28. WQBO-CTL response of (a) refractive index (shading) and meridional gradient of potential vorticity (PV gradient; contour), and (b) U-wind (contour) and temperature (shading) at 1-2-day integration. The result is ensemble mean of 100 transient experiments.

3.3.3. Zonal asymmetry induced by topography

To investigate why this downward coupling is strong in East Asia, a possible role of the Tibetan Plateau (TB) is investigated. Since East Asia is the downstream region of the TB and jet, it is expected to the topography-induced stationary waves may enhance the eddies as well as the QBO response to the East Asia.

The idealized Gaussian-shape topography is introduced in the model with a variety of the height. From flat (0km) to realistic (4km), the CTL and WQBO simulations are conducted with this topography set (Fig. 3.29). It is different point with previous studies having no consideration of the topographically-induced stationary planetary waves (Garfinkel and Hartmann, 2011a, b).

The spatial distribution of the WQBO response shows that the strong downward coupling in East Asia could come from the presence of topography such as the Tibetan Plateau. Figures 3.30b and c represent the simulated downward arching zonal wind anomalies are qualitatively similar to the observation. The equatorward shift of the jet during the WQBO phase is observed regardless of the presence of the topography. However, the equatorward shift of the jet becomes stronger in the realistic TB case. The spatial distribution of 250 hPa U-wind response becomes stronger and zonally asymmetric in TB_4km, particularly in the

downstream regions of the topography (lower panel of the Fig. 3.30c). The TB_4km experiment shows a more qualitatively similar WQBO response to the observed one than the Notopo. Both climatological mean jet (contour) and wind response to the QBO (shading) are robust in the East Asia where the downstream region of the topography. However, the response is zonally symmetric in the Notopo experiment (lower panel of the Fig. 3.30b).

The magnitude of the zonal asymmetric response is also controlled by the height of the TB (Fig. 3. 31). As the TB height increases (from 2km to 4km), the U-wind response to the QBO becomes stronger (cf. Figs. 3.31a and b). The response is strongest in the 4km case, which is almost similar with the realistic height of the TB. The eddies also become stronger in the TB_4km. The EMFC are stronger in the TB_4km than Notopo (Fig. 3.32). Similar result is also seen in the wave cospectra (Fig. 3.33). The stronger high-frequency eddies mainly contribute to the stronger total EMFC and thus the zonal wind response. Based on the momentum balance in the Eulerian mean, the zonal wind can be modulated by not only the EMFC but also Coriolis force acting on the anomalous mean meridional wind and ageostrophic terms. Thus, the stronger EMFC leads to the stronger zonal wind in TB_4km than that in Notopo, but the zonal wind response is somewhat weaker than expectation due to the contribution of the remaining terms on the zonal

wind response (cf. gray and black lines in Figs. 3.32a and b). The enhancement of the high-frequency eddies is re-confirmed in the spatial distribution of the v-wind response to the QBO (Fig. 3.34). As the TB height increases (from 2km to 4km), wave number 7 becomes evident especially in the downstream region of the topography, i.e., East Asia. The above results indicate that the TB makes the stronger QBO downward coupling in East Asia region.

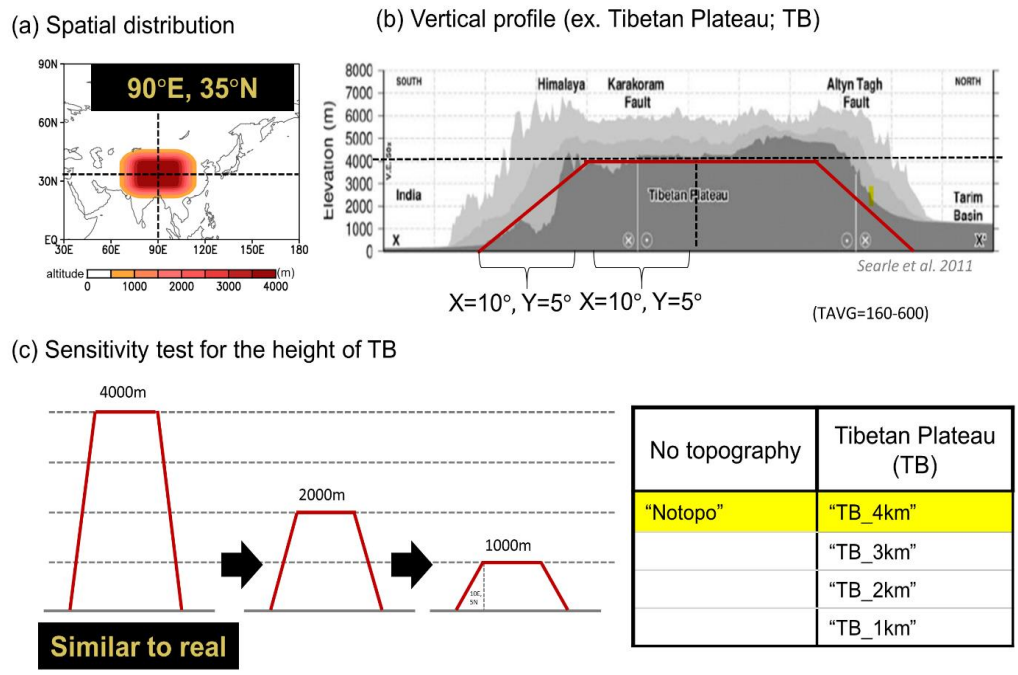

No topography	Tibetan Plateau (TB)
"Notopo"	"TB_4km"
	"TB_3km"
	"TB_2km"
	"TB_1km"

Figure 3.29. Idealized Gaussian-shaped Tibetan Plateau (TB). (a) its spatial distribution, (b) vertical profile, and (c) a variety of height of the TB for the sensitivity test.

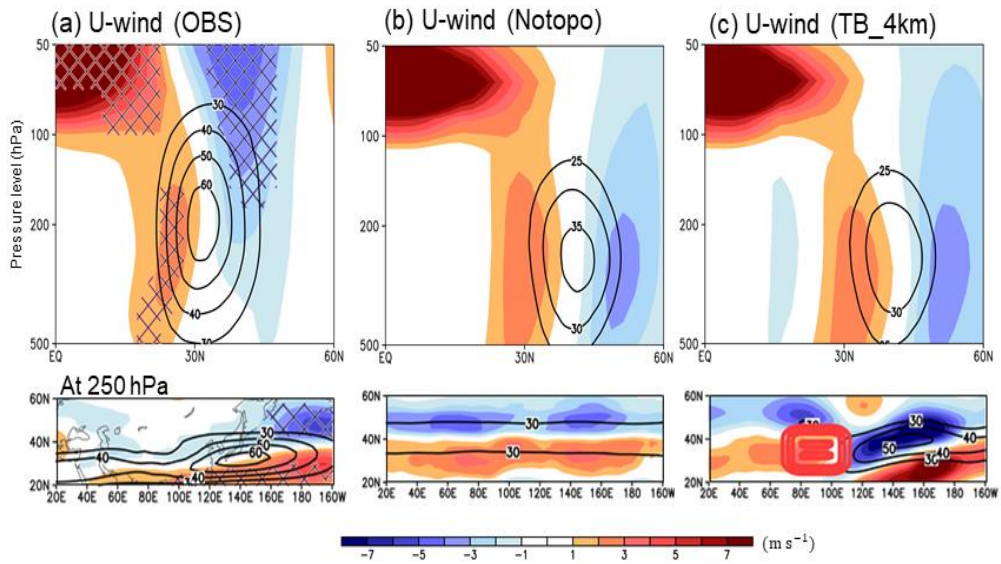

Figure 3.30. WQBO-CTL response of U-wind in (a) observation, (b) Notopo experiment, and (c) TB_4km. (lower panels) Same as upper panels but for the spatial distribution at 250hPa. The contour and shading represent the climatological mean jet and WQBO response, respectively. Red thick contour in (lower panel of c) indicates the TB_4km Gaussian-shaped topography.

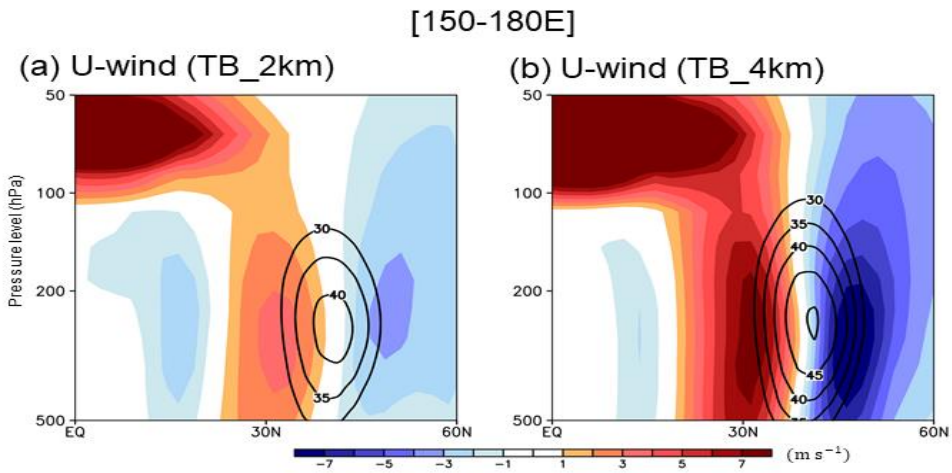

Figure 3.31. U-wind response averaged over the downstream region of the APJ (120°– 150°E). (a) TB_2km and (b) TB_4km experiments.

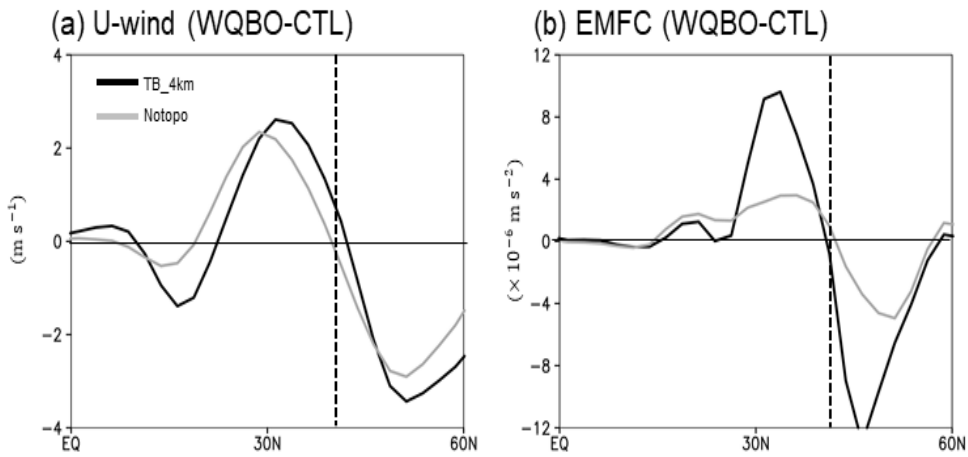

Figure 3.32. The WQBO-CTL response of the (a) U-wind in the upper troposphere (averaged over the 120 hPa to 400hPa) and (b) EMFC in the lower stratosphere and upper troposphere (averaged over around 80 hPa to 230 hPa in Notopo (gray) and TB_4km (black), respectively. The vertical dotted line represents the climatological mean jet position.

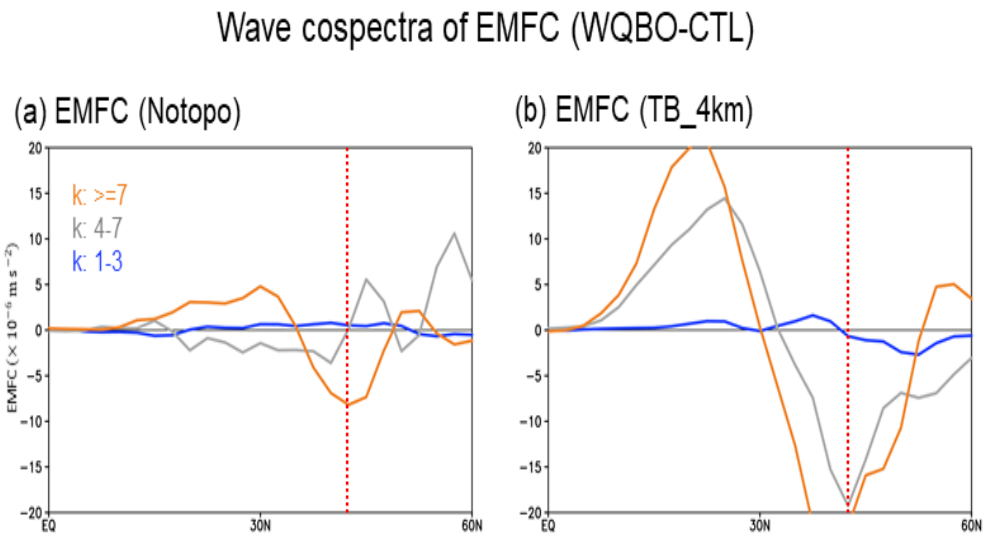

Figure 3.33. Wave cospectra of EMFC WQBO-CTL response in (a) Notopo and (b) TB_4km. The vertical dotted line represents the climatological mean jet position.

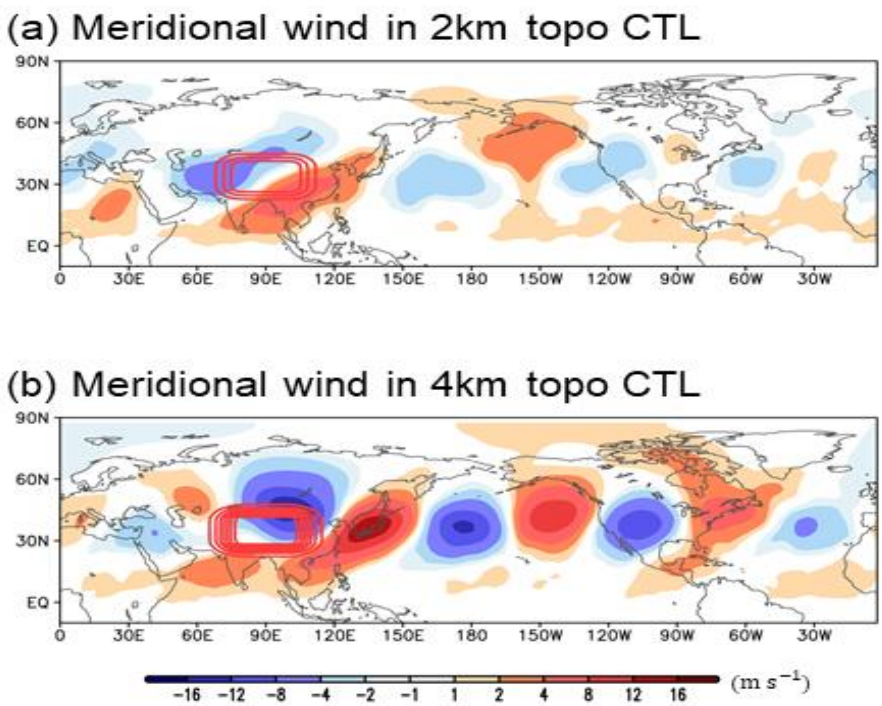

Figure 3.34. 250hPa meridional (V)-wind in CTL of (a) TB_2km and (b) TB_4km. The red contours denote the TB.

3.4. Climate models and operational prediction systems

In this section, whether the observed downward coupling is well predicted/reproduced are investigated. Figure 3.35 shows the FM-mean QBO downward coupling and QBO-East Asia teleconnection of the 7 ensemble reforecasts initialized at every 01 February and March. The QBO downward coupling (Fig. 3.35a) and the associated surface impacts (Fig. 3.35b) are well predicted in an operational prediction system. The operational prediction system also shows a high prediction skill of the

QBO downward coupling (Fig. 3.35c). The high ACC of the APJ-shift index remains even at a long forecast lead time (red dotted line after the 3-pentad forecast lead time). As mentioned earlier, the sub-seasonal prediction skill of the mid-latitudes is only three pentads (Son et al., 2020), thus the statistically significant ACC at 3-5 forecast lead pentad indicates that the QBO could be useful for the East Asian surface prediction. It is re-confirmed by removing the QBO-related signals from the APJ shift index. When the QBO signal is removed, the high skill disappears (black line in Fig. 3.35c).

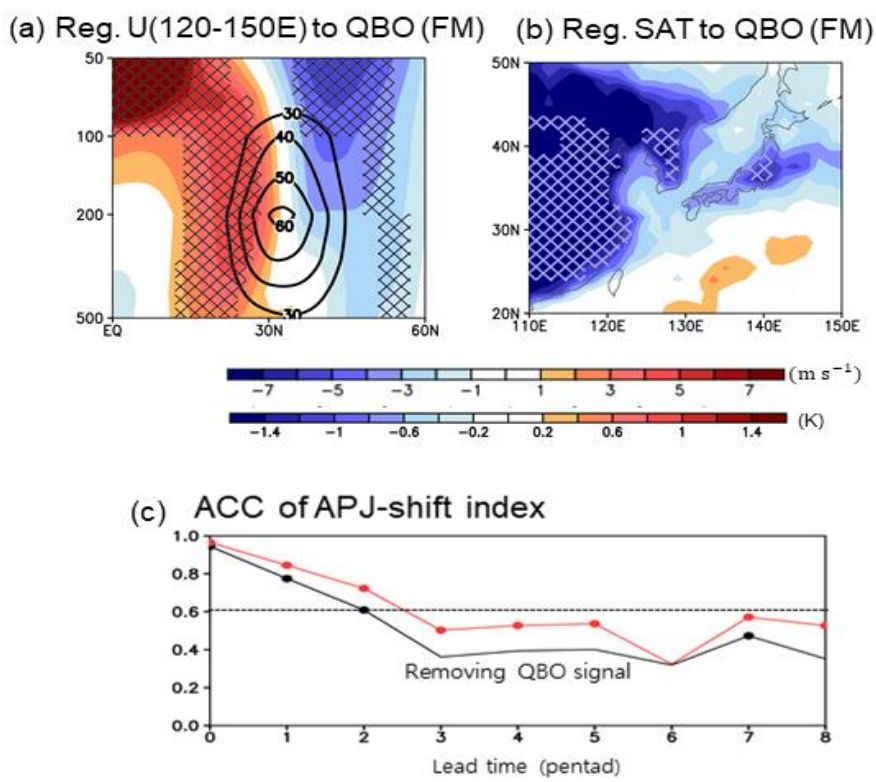

Figure 3.35. QBO downward coupling prediction in GloSea6 prediction system.

To improve the fidelity of QBO in state-of-the-art climate models, SPARC which is a core project of the World Climate Research Programme (WCRP) launched the QBOi (see the Section 3.1.1). 8 models participating in QBOi (Table 3.2) show a qualitatively well reproduce the climatological mean jet (black contour in Fig. 3.36). However, the equatorward shift of the APJ during the WQBO phase is reproduced only in the two models. The jet is strengthened in the two models, but weakened or even poleward shift in the other four models among 8 models (shading in Fig. 3.36). MRI-ESM2.0 and WACCM show a strengthening of the jet during the WQBO phase, but EC-EARTH, MIROC-ESM show the weakening of the jet. LMDz and MIROC-AGCM show the opposite response, i.e., poleward shift of the jet. Only ECHAM5sh and GISS-E2-2-G show equatorward shift of the APJ during the WQBO phase like observations. As a result, the multi-model mean anomaly becomes weak (not shown). This large inter-model spread of the jet response is closely related to the downward horseshoe-shaped zonal wind anomalies (shading in Fig. 3.37). The sector-mean zonal wind anomaly shows APJ response is connected to the downward horseshoe-shaped anomalies from lower stratosphere. Since all models reproduce well the QBO, a possible reason for the large inter-model spread of the jet response may be linked to the representation of the QBO seasonality itself or the wave and mean state responses in the upper troposphere as

found in section 3.3.

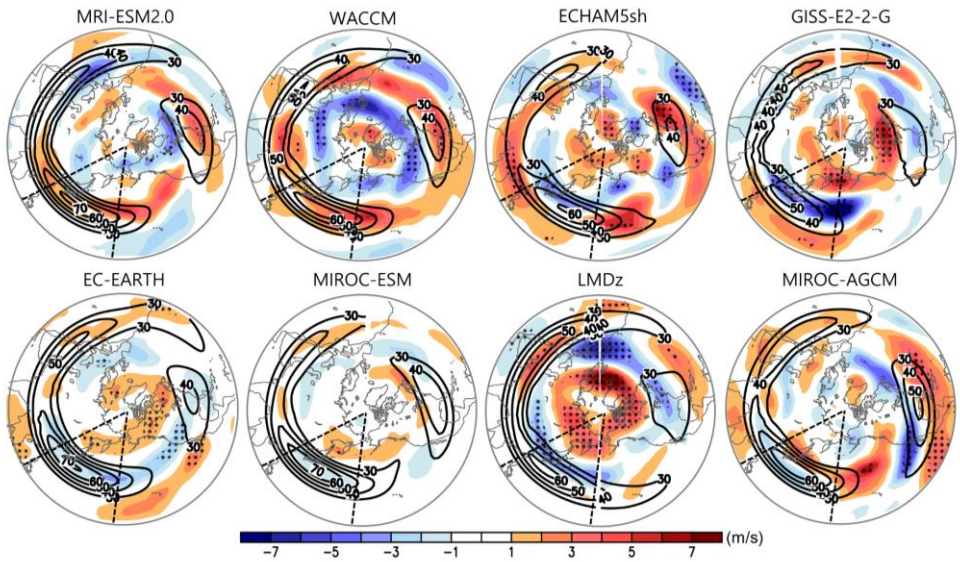

Figure 3.36. 250hPa U-wind response to the W-EQBO in QBOi climate models.

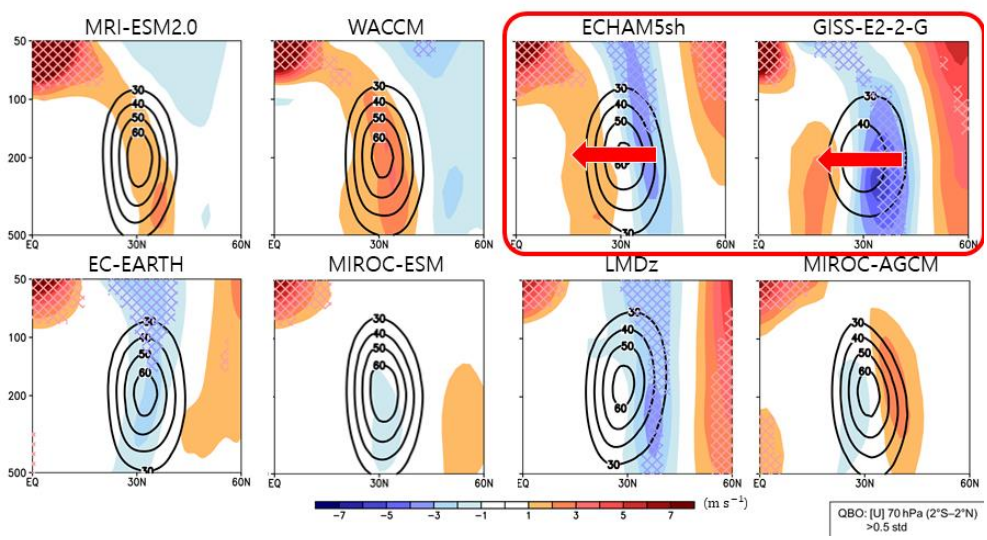

Figure 3.37. Pacific sector-mean U-wind response to the W-EQBO in QBOi climate models.

4. Summary and Discussion

This study documents that the East Asian SAT is significantly modulated by the ENSO in early winter and by the QBO in late winter. In the El Niño winters, anomalous surface warming is evident over the East Asia accompanied by anomalous anti-cyclonic circulation in the Kuroshio Extension region (KU). The atmospheric circulation anomaly drives the warm advection to the East Asia region, resulting in a relatively warm anomaly over the East Asia surface. As a result, a positive relationship is appeared in East Asia region between the ENSO and surface air temperature.

The ENSO-East Asia teleconnection is robust in early winter (December), which is closely related to two tropical convection variations over the MC and IO. In the El Niño winters, CP convection tends to be enhanced monotonously throughout the boreal winter, while MC and IO convection anomaly tend to be strong around mid-December.

The difference in sub-seasonal variations among tropical convection anomalies leads to a robust sub-seasonal modulation of the ENSO-East Asia teleconnection. As the CP convection anomaly becomes strong, the associated poleward Rossby wave trains make atmospheric circulation anomalies over the North Pacific region, i.e. PNA pattern. However, the poleward Rossby wave trains associated with the −1×MC

and IO convection anomalies tend to make a constructive interference of the atmospheric circulation anomalies over the KU region, which can directly influence on East Asia surface. As they become strong in early winter, the ENSO-East Asia teleconnection, modulated by anomalous circulation anomaly in the KU, also becomes strong in early winter as summarized in Fig. 4.1.

The physical mechanisms of the tropical convection anomalies in early ENSO winter has been investigated. The moistening, which is essential to the convection, may a key mechanism for the enhanced IO convection anomaly in early winter. All 14 El Niño years are accompanied by the enhanced IO convection anomaly in early winter. In the El Niño winters, the suppressed convection anomaly over the MC leads to the rotational flow between IO and MC as a part of the Rossby wave response. The associated horizontal wind anomalies between the IO and MC bring moist air to the IO. The moisture budget analysis confirms that the horizontal advection term is a primary contributor to the IO moistening in early winter. The additional moisture anomaly, added to the plentiful climatological mean moisture in early winter, helps the convection development efficiently. The IO moistening is closely related to the El Niño but not to IO SST variability such as IO dipole mode or IO basin-wide warming mode.

The state-of-the-art model prediction systems (i.e. MME) have

poor prediction skills in the ENSO-related tropical convection anomalies as well as the ENSO-East Asia teleconnections. Although the spatial distributions of the predicted ENSO-East Asia teleconnections are quantitively well represented, the East Asian SAT and KU Z500 prediction skills show a decline in a short forecast lead time. This is because the MME tends to predict the ENSO-related tropical convection anomalies much weaker and earlier than the observations. The poor representation of tropical convection sub-seasonal variations leads to poor representation of the sub-seasonal variations of the teleconnections from the −1×MC, and IO. Such discrepancy between the observations and MME is obvious in early winter when the observed teleconnections are robust. Thus, a better representation of the tropical convection in model predictions is required to improve the ENSO-East Asia teleconnection prediction.

The QBO-East Asia teleconnection is also important in late winter (February-March). During the QBO westerly phase (WQBO), a horseshoe-shaped zonal wind anomaly extends from the tropical lower stratosphere to the subtropical mid-troposphere. It results in an equatorward shift of the APJ. This equatorward shift of the jet enhances the cyclonic circulation anomaly on the equatorward side of the climatological APJ and an anticyclonic circulation anomaly on its poleward side. The associated surface wind anomalies induce cold

advection toward the East Asia region in late winter. This QBO downward coupling-induced East Asian SAT change is more important than the ENSO-induced change. Quantitatively, approximately 16% of the interannual variability of the East Asian SAT in February–March can be explained by the QBO. The Granger causality test further confirms that the QBO has a causal relationship with the East Asian SAT variability in this season.

To understand this QBO-APJ dynamics, QBO nudging experiment is conducted by using GFDL Flexible Modeling System atmospheric dry dynamic core model. Under the winter season background state, the tropospheric zonal wind response to the WQBO-like forcing shows an equatorward shift the subtropical jet. A horseshoe-shaped wind anomaly extends to subtropical mid-troposphere as in observation. This result indicates that the QBO-East Asian SAT relationship is directly affected by the QBO in stratospheric equator (i.e. subtropical route) not the tropical route or polar route. It is consistent with the Granger causality test, which indicates the late winter QBO downward coupling is only appeared in the subtropical route particularly in East Asia sector and the downward coupling is well represented in the simple dry dynamic core model.

The role of the stratospheric QBO-related atmospheric background changes in the QBO downward coupling is further

investigated with the 100-ensemble transient experiments. WQBO-related atmospheric background state induces changes of wind and temperature in the subtropical lower stratosphere-upper troposphere, leading to the change of PV gradient as well as the positive refractive index. Since the positive refractive index is favorable condition for the Rossby wave propagation, the equatorward and upward eddy propagation is induced in the subtropical lower stratosphere-upper troposphere. Such eddy propagation results in a horizontal eddy momentum and its convergence, and the resultant zonal wind anomaly in the region. This QBO downward coupling forms within a one-month lag in an idealized model experiments, which is consistent with the Granger causality test.

The presence of the topography may contribute to the strong QBO downward coupling in East Asia sector. QBO downward coupling becomes stronger in East Asia or Pacific sector than that in Atlantic sector when the topography such as Tibetan Plateau is introduced in the idealized experiments. As the topography increases, the downward coupling also becomes stronger particularly in the downstream region of the topography, i.e., East Asia. The above findings are summarized in Fig. 4.2.

The operational prediction systems show reasonable prediction skills of the QBO downward coupling and its surface impact. The

horseshoe-shaped zonal wind anomaly and surface response are well represented in the prediction systems. In addition, high prediction skill remains even in the sub-seasonal to seasonal time scale (longer than two-week forecast lead time). However, climate models do not well capture the QBO downward coupling. The equatorward shift of the APJ during the WQBO phase is reproduced only in the two out of eight QBOi models. The jet is strengthened in the two models, but weakened in the other two models, and even northward shift is seen in some models. A further study is needed to figure out the key factor for the improvement of the QBO-East Asia teleconnection prediction/simulation.

It is not clear why the QBO-East Asian SAT relationship is most pronounced in February–March. The climatological APJ forms at relatively lower latitudes, approximately at 32°N, in late winter. This equatorward shifted APJ is likely to be better connected to the QBO (Garfinkel and Hartmann, 2011a). It should be stated that the mechanism through which the QBO generates the horseshoe-shaped subtropical wind response is associated to the eddy propagation change, which can derive the zonal wind change based on the momentum balance in Eulerian mean. Furthermore, the physical mechanisms of the IO and MC convection anomalies in early ENSO winter is needed to investigate in detail. Some hints in the present dissertation indicates that it may be related to the Madden-Julian Oscillation (MJO), which is

characterized by eastward propagation of tropical deep convection from the IO. The convection moves within two regions, IO and MC, which are the pathways for the sub-seasonal tropical leading mode referred to as the MJO. 50% of El Niño years indeed are accompanied by MJO phase 3 in early winter, which corresponds to the MJO convection in the IO. Whether the IO convection is MJO or not, the convection moves eastward, resulting in an increase of precipitation near the western North Pacific.

Our finding has an important implication to seasonal prediction. The QBO is highly predictable in operational seasonal prediction models (Scaife et al., 2014; Lim et al., 2019). ENSO is also highly predictable in prediction systems (Ham et al., 2019). This may allow an extended prediction of the East Asian SAT in winter, a few months in advance. To utilize the high predictability of these two tropical leading modes to the teleconnection prediction, it is important to well simulate/predict the ENSO-related tropical convection and QBO-related mean state and eddy changes, which serve as the key mechanism of the teleconnections.

Overall, this dissertation sheds light on the teleconnections between ENSO, QBO, and East Asian winter surface climate, enhancing our understanding of climate variability in this crucial region, and providing valuable insights for sub-seasonal to seasonal prediction.

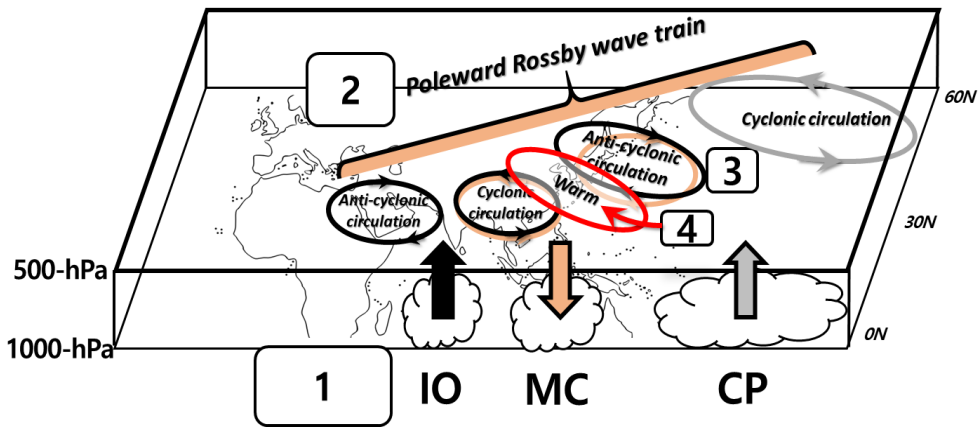

Figure 4.1. Schematic diagram of the early winter ENSO-East Asia teleconnections, which consists of 1) ENSO-related tropical convection, 2) Poleward Rossby wave trains, 3) constructive interference over the Kuroshio Extension region, 4) Warm advection induced by anti-cyclonic circulation change over the Kuroshio Extension region.

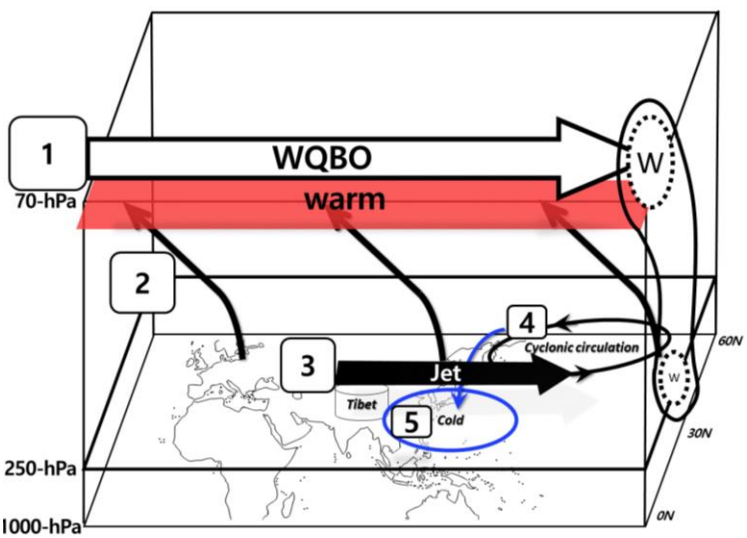

Figure 4.2. Schematic diagram of the late winter QBO-East Asia teleconnections, which consists of 1) westerly wind shear and warm anomalies over the subtropical lower stratosphere-upper troposphere, 2) equatorward, upward eddies, 3) equatorward shift of the Asian-Pacific jet, 4) Cold advection induced by cyclonic circulation change over the North Pacific Ocean, 5) cold anomaly in East Asia.

References

Abid, M. A. et al. (2021) Separating the Indian and Pacific Ocean impacts on the Euro-Atlantic response to ENSO and its transition from early to late winter. Journal of Climate, 34, 1531– 1548.

Ämiri, Ä. and Linden, M. (2016) Income and total expenditure on health in OECD countries: Evidence from panel data and Hsiao's version of Granger non-causality tests. Economics and Business Letters, 5, 1–9.

Arblaster, J. M. and Alexander, L. V. (2012) The impact of the El Niño-Southern Oscillation on maximum temperature extremes. Geophysical Research Letters, 39.

An, S. I. and Wang, B. (2001) Mechanisms of locking of the El Niño and La Niña mature phases to boreal winter. Journal of climate, 14, 2164–2176.

Andrews et al. (2020) Historical simulations with HadGEM3–GC3.1 for CMIP6. Journal of Advances in Modeling Earth Systems, 12, e2019MS001995.

Annamalai, H., Okajima, H., and Watanabe, M. (2007) Possible impact of the Indian Ocean SST on the Northern Hemisphere circulation during El Niño. Journal of Climate, 20, 3164–3189.

Anstey, J. A., et al. (2022) Teleconnections of the quasi-biennial oscillation in a multi-model ensemble of QBO-resolving models. Quarterly Journal of

the Royal Meteorological Society, 148, 1568-1592.

Bladé, I., Newman, M., Alexander, M. A. and Scott, J. D. (2008) The late fall extratropical response to ENSO: sensitivity to coupling and convection in the tropical West Pacific. Journal of Climate, 21, 6101–6118.

Baldwin, M. P et al. (2001) The quasi-biennial oscillation. Reviews of Geophysics, 39, 179–229.

Barnes, E. A. and Simpson, I. R. (2017) Seasonal sensitivity of the Northern Hemisphere jet streams to arctic temperatures on sub-seasonal time scales. Journal of Climate, 30, 10117–10137.

Baxter, S., Weaver, S., Gottschalck, J. and Xue, Y. (2014) Pentad evolution of wintertime impacts of the Madden-Julian oscillation over the contiguous United States. Journal of Climate, 27, 7356–7367.

Bjerknes, J. (1969) Atmospheric teleconnections from the equatorial Pacific. Monthly weather review, 97, 163-17

Boer, G. J. et al. (2016) The decadal climate prediction project (DCPP) contribution to CMIP6. Geoscientific Model Development, 9, 3751–3777.2.

Bretherton, C. S., Peters, M. E., and Back, L. E. (2004) Relationships between water vapor path and precipitation over the tropical oceans. Journal of Climate 17, 1517–1528.

Brown, R. G. and Zhang, C. (1997) Variability of midtropospheric moisture and its effect on cloud-top height distribution during TOGA COARE. Journal of the atmospheric sciences, 54, 2760–2774.

Bushell, A.C., et al. (2022) Evaluation of the Quasi-Biennial Oscillation in global climate models for the SPARC QBO-initiative. Quarterly Journal of the Royal Meteorological Society, 148, 1459– 1489.

Chen, W. and Li, T. (2007) Modulation of northern hemisphere wintertime stationary planetary wave activity: East Asian climate relationships by the Quasi-Biennial Oscillation. Journal of Geophysical Research: Atmospheres, 112. https://doi.org/10.1029/2007JD008611.

Collimore, C. C. et al. (2003). On the relationship between the QBO and tropical deep convection. Journal of climate, 16, 2552-2568.

Crooks, S. A. and Gray, L. J. (2005) Characterization of the 11-year solar signal using a multiple regression analysis of the ERA-40 dataset. Journal of Climate, 18, 996–1015.

Döscher et al. (2021) The EC-earth3 Earth system model for the climate model intercomparison project 6. Geoscientific Model Development Discussions, 1, 2021– 3020.

Eichelberger, S.J. and Hartmann, D.L. (2007) Zonal jet structure and the leading mode of variability. Journal of Climate, 20, 5149–5163.

Garfinkel, C. I. and Hartmann, D. L. (2011a) The influence of the quasi-biennial oscillation on the troposphere in winter in a hierarchy of models. Part I: Simplified dry GCMs. Journal of the Atmospheric Sciences, 68, 1273–1289.

Garfinkel, C. I. and Hartmann, D. L. (2011b) Influence of the quasi-biennial oscillation on the troposphere in winter in a hierarchy of models. Part II: Perpetual winter WACCM runs, Journal of the Atmospheric Sciences, 68, 2026–2041.

Geng, X., Zhang, W., Stuecker, M. F. and Jin, F. F (2017) Strong sub-seasonal wintertime cooling over East Asia and Northern Europe associated with super El Niño events. Scientific Reports, 7, 1–9.

Geweke, J. F. (1984) Measures of conditional linear dependence and feedback between time series. Journal of the American Statistical Association, 79, 907-915.

Glantz, M. H. (2001) Currents of change: impacts of El Niño and La Niña on climate and society. Cambridge University Press.

Goddard, L. et al. (2013) A verification framework for interannual-to-decadal predictions experiments. Climate Dynamics, 40, 245– 272.

Granger, C. W. (1969) Investigating causal relations by econometric models and cross-spectral methods. Econometrica: journal of the Econometric Society, 424–438.

Gray, L. J. et al. (2018) Surface impacts of the quasi biennial oscillation. Atmospheric Chemistry and Physics, 18, 8227–8247.

Ham, Y. G., Kim, J. H., and Luo, J. J. (2019) Deep learning for multi-year ENSO forecasts. Nature, 573, 568-572.

Haynes, P. et al. (2021) The influence of the stratosphere on the tropical troposphere. Journal of the Meteorological Society of Japan. Ser. II, 99, https://doi.org/10.2151/jmsj.2021-040.

Held, I. M., and Suarez, M. J. (1994) A proposal for the intercomparison of the dynamical cores of atmospheric general circulation models. Bulletin of the American Meteorological society, 75, 1825-1830.

Hersbach, H. et al. (2020) The ERA5 global reanalysis. Quarterly Journal of the Royal Meteorological Society, 146, 1999–2049.

Hoell, A., Barlow, M., Wheeler, M. C. and Funk, C. (2014) Disruptions of El Niño-southern oscillation teleconnections by the Madden-Julian Oscillation. Geophysical Research Letters, 41, 998–1004.

Holloway, C. E., and Neelin, J. D. (2009) Moisture vertical structure, column water vapor, and tropical deep convection. Journal of Atmospheric Sciences, 66, 1665–1683.

Holton, J. R. and Tan, H. C. (1980) The influence of the equatorial quasi-biennial oscillation on the global circulation at 50 mb. Journal of Atmospheric

Sciences, 37, 2200–2208.

Hood, L. L., Redman, M. A., Johnson, W. L., and Galarneau, T. J. (2020) Stratospheric influences on the MJO-induced Rossby wave train: effects on intraseasonal climate. Journal of Climate, 33, 365-389.

Horel, J. D. and Wallace, J. M. (1981) Planetary-scale atmospheric phenomena associated with the Southern Oscillation. Monthly Weather Review, 109, 813–829.

Hsiao, C. (1981) Autoregressive modelling and money-income causality detection. Journal of Monetary economics, 7, 85–106.

Huang, B. et al. (2017) Extended reconstructed sea surface temperature, version 5 (ERSSTv5): upgrades, validations, and inter-comparisons. Journal of Climate, 30, 8179–8205.

Jin, F. and Hoskins, B. J. (1995) The direct response to tropical heating in a baroclinic atmosphere. Journal of the Atmospheric Sciences, 52, 307–319.

Jong, B. T., Ting, M. and Seager, R (2016) El Niño's impact on California precipitation: Seasonality, regionality, and El Niño intensity. Environmental Research Letters, 11, 054021.

Kang I. S. (1998) Relationship between El Niño and climate variation over Korea peninsula. Journal of Korean Meteorology Society, 34, 390-396

(in Korean with English abstract).

Karoly, D. J., and Hoskins, B. J. (1982) Three dimensional propagation of planetary waves. Journal of the Meteorological Society of Japan. Ser. II, 60, 109-123.

Kim, S., Son, H. Y. and Kug, J. S (2017) How well do climate models simulate atmospheric teleconnctions over the North Pacific and East Asia associated with ENSO? Climate Dynamics, 48, 971–985.

_____ (2018) Relative roles of equatorial central Pacific and western North Pacific precipitation anomalies in ENSO teleconnection over the North Pacific. Climate Dynamics, 51, 4345–4355.

Kim, H., Lee, J., Hyun, Y.-K., and Hwang, S.-O. (2021). The KMA Global Seasonal Forecasting System (GloSea6) - Part 1: Operational System and Improvements, Atmosphere-KOREA, 31, 341-359 [In Korean].

Klotzbach, P. et al. (2019) On the emerging relationship between the stratospheric Quasi-Biennial oscillation and the Madden-Julian oscillation. Scientific Reports, 9, 1–9.

Kobayashi, C. et al. (2014) Preliminary results of the JRA-55C, an atmospheric reanalysis assimilating conventional observations only. SOLA, 10, 78–82.

Kobayashi, S. et al. (2015) The JRA-55 reanalysis: General specifications and basic characteristics. Journal of the Meteorological Society of Japan. Ser. II, 93, 5–48.

Kug J. –S. et al. (2010) Statistical relationship between two types of El Niño events and climate variation over the Korean Peninsula. Asia-Pacific Journal of Atmospheric Science, 46, 467-474.

Kug, J.-S. et al. (2015) Two distinct influences of Arctic warming on cold years over North America and East Asia. Nature Geoscience, 8, 759–762.

Lee, S. et al. (2020) Interannual variation of the East Asia Jet Stream and its impact on the horizontal distribution of aerosol in boreal spring. Atmospheric Environment, 223, 117296.

Li, W. et al. (2018) Influence of Tibetan Plateau snow cover on East Asian atmospheric circulation at medium-range time scales. Nature Communications, 9, 1–9.

Liebmann, B. and Smith, C. A. (1996) Description of a complete (interpolated) outgoing longwave radiation dataset. Bulletin of the American Meteorological Society, 77, 1275–1277.

Lim, Y et al. (2019) Influence of the QBO on MJO prediction skill in the sub-seasonal-to-seasonal prediction models. Climate Dynamics, 53, 1681–1695.

Lindzen, R. S., and Nigam, S. (1987) On the role of sea surface temperature gradients in forcing low-level winds and convergence in the tropics. Journal of the Atmospheric Sciences, 44, 2418– 2436.

Lu, H. et al. (2014) Mechanisms for the Holton-Tan relationship and its decadal variation. Journal of Geophysical Research: Atmospheres, 119, 2811–2830.

Luo, X. and Zhang, Y. (2015) The linkage between upper-level jet streams over East Asia and East Asian winter monsoon variability. Journal of Climate, 28, 9013–9028.

Ma, T. et al. (2021) The observed influence of the Quasi-Biennial Oscillation in the lower equatorial stratosphere on the East Asian winter monsoon during early boreal winter. International Journal of Climatology.

Madden, R. A., and Julian, P. R. (1971) Detection of a 40–50 day oscillation in the zonal wind in the tropical Pacific. Journal of Atmospheric Sciences, 28, 702-708.

Marshall, A. G., and Scaife, A. A. (2009) Impact of the QBO on surface winter climate. Journal of Geophysical Research: Atmospheres, 114(D18).

Martin, Z. et al. (2021) The influence of the quasi-biennial oscillation on the Madden–Julian oscillation. Nature Reviews Earth & Environment, 1–13.

McGraw MC and Barnes East Asia. (2018) Memory matters: A case for Granger

causality in climate variability studies. Journal of Climate, 31, 3289-3300.

McPhaden, M. J., Zebiak, S. E., and Glantz, M. H. (2006) ENSO as an integrating concept in earth science. science, 314, 1740-1745.

Moon, J. Y. Wang, B. and Ha, K. J. (2011) ENSO regulation of MJO teleconnection. Climate Dynamics, 37, 1133–1149.

Müller, W. A. et al. (2018) A higher-resolution version of the max planck institute Earth system model (MPI-ESM1. 2-HR). Journal of Advances in Modeling Earth Systems, 10, 1383– 1413.

Naujokat, B. (1986) An update of the observed quasi-biennial oscillation of the stratospheric winds over the tropics. Journal of Atmospheric Sciences, 43, 1873–1877.

Nicholls, N. et al. (2005). The El Niño–Southern Oscillation and daily temperature extremes in east Asia and the west Pacific. Geophysical Research Letters, 32.

Park, C.-H., Choi, J., Son, S.-W., Kim, D., Yeh, S.-W. and Kug, J.-S. (2023) Sub-seasonal variability of ENSO teleconnections in western North America and its prediction skill, Journal of Geophysical Research - Atmospheres, 128, e2022JD037985.

Park, C.-H., Son, S.-W., Lim, Y. and Choi, J. (2022) Quasi-biennial oscillation-

related surface air temperature change over the western North Pacific in late winter, International Journal of Climatology, 30, 4351-4359.

_____. and Choi, J. (2018) Granger Causality Test between ENSO and Winter Climate Variability over the Korean Peninsula, Journal of Climate Change Research, 9, 171-179 [In Korean].

_____. (2022) Relationship between the QBO and Surface Air Temperature in the Korean peninsula, Atmosphere-KOREA, 32, 39-49 [In Korean].

Philander, S. G. (1989) El Niño, La Niña, and the southern oscillation. International Geophysics Series, 46, X– 289.

Rao, J., Garfinkel, C. I. and White, I. P. (2020) How does the Quasi-Biennial Oscillation affect the boreal winter tropospheric circulation in CMIP5/6 models? Journal of Climate, 33, 8975–8996.

Ropelewski, C. F. and Halpert, M. S. (1986) North American precipitation and temperature patterns associated with the El Niño/Southern Oscillation (ENSO). Journal of the Atmospheric Sciences, 114, 2352–2362.

Rushley, S. S., Kim, D., Bretherton, C. S., and Ahn, M. S. (2018) Reexamining the nonlinear moisture-precipitation relationship over the tropical oceans. Geophysical research letters, 45, 1133–1140.

Ruti, P. M. et al. (2006) Does the subtropical jet catalyze the midlatitude

atmospheric regimes?, Geophysical research letters, 33, L06814, https://doi.org/10.1029/2005GL024620.

Scaife, A. A. et al. (2014) Predictability of the quasi-biennial oscillation and its northern winter teleconnection on seasonal to decadal timescales. Geophysical Research Letters, 41, 1752–1758.

Seo, K. H. and Son, S. W. (2012) The global atmospheric circulation response to tropical diabatic heating associated with the Madden-Julian oscillation during northern winter. Journal of the Atmospheric Sciences, 69, 79–96.

Seo, K. H. and Lee, H. J. (2017) Mechanisms for a PNA-like teleconnection pattern in response to the MJO. Journal of the Atmospheric Sciences, 74, 1767–1781.

Sherwood, S. C. (1999) Convective precursors and predictability in the tropical western Pacific. Monthly Weather Review, 127, 2977–2991.

Simpson, I.R., Blackburn, M. and Haigh, J.D. (2009) The role of eddies in driving the tropospheric response to stratospheric heating perturbations. Journal of the Atmospheric Sciences, 66, 1347–1365.

Simpson, I.R., Blackburn, M., Haigh, J.D. and Sparrow, S.N. (2010) The impact of the state of the troposphere on the response to stratospheric heating in a simplified GCM. Journal of Climate, 23, 6166–6185.

Son, H. Y. et al. (2014) Winter precipitation variability over Korean PeNiñsula associated with ENSO. Climate Dynamics, 42, 3171–3186.

Son, S.W. et al. (2017) Stratospheric Control of the Madden-Julian Oscillation, Journal of Climate, 30, 1909-1922

Son, S.W. et al. (2020) Extratropical prediction skill of the subseasonal-to-seasonal (S2S) prediction models. Journal of Geophysical Research: Atmospheres, 125, e2019JD031273..

Sponberg, K. (1999) Compendium of Climatological Impacts, National Oceanic and Atmospheric Administration, Office of Global Programs, Washington, DC.

Takayabu, Y. N., Yokomori, J. I., and Yoneyama, K. A (2006) diagnostic study on interactions between atmospheric thermodynamic structure and cumulus convection over the tropical western Pacific Ocean and over the Indochina PeNiñsula. Journal of the Meteorological Society of Japan. Ser. II, 84, 151–169.

Tatebe, H. et al. (2019) Description and basic evaluation of simulated mean state, internal variability, and climate sensitivity in MIROC6. Geoscientific Model Development, 12, 2727– 2765.

Thompson, D. W. and Wallace, J. M. (1998) The Arctic Oscillation signature in the wintertime geopotential height and temperature fields. Geophysical research letters, 25, 1297–1300.

Thompson, D. W., Baldwin, M. P. and Wallace, J. M. (2002) Stratospheric connection to Northern Hemisphere wintertime weather: Implications for prediction. Journal of Climate, 15, 1421–1428.

Wallace, J. M. and Gutzler, D. S. (1981) Teleconnections in the geopotential height field during the Northern Hemisphere winter. Journal of the Atmospheric Sciences, 109, 784–812.

Wang, B., Wu, R. and Fu, X. (2000) Pacific-East Asian teleconnection: how does ENSO affect East Asian climate? Journal of Climate, 13, 1517–1536.

Watanabe, M., and Kimoto, M. (2000) Atmosphere-ocean thermal coupling in the North Atlantic: A positive feedback. Quarterly Journal of the Royal Meteorological Society, 126, 3343– 3369

Webster, P. J. (1983). Large scale dynamical processes in atmosphere..

Xie, S. P. et al. (2009) Indian Ocean capacitor effect on Indo–western Pacific climate during the summer following El Niño. Journal of Climate, 22, 730–747.

Xie, P., and Arkin, P. A. (1997) Global precipitation: A 17-year monthly analysis based on gauge observations, satellite estimates, and numerical model outputs. Bulletin of the american meteorological society, 78, 2539-2558.

Yang, S., Lau, K. M. and Kim, K. M. (2002) Variations of the East Asian Jetstream

and Asian–Pacific–American winter climate anomalies. Journal of Climate, 15, 306–325.

Yeh, S.-W., Kug, J.-S. and An, S.-I. (2014) Recent progress on two types of El Niño: Observations, Dynamics, and Future changes. Asia-Pacific Journal of Atmospheric Sciences, 50, 69-81.

Yeh, S. W. et al. (2018) ENSO atmospheric teleconnections and their response to greenhouse gas forcing. Reviews of Geophysics, 56, 185–206.

Zhang, C. (2005) Madden-julian oscillation. Reviews of Geophysics, 43.

*Some contents, figures, and tables were originated from the below studies:

Park, C.-H., Choi, J., Son, S.-W., Kim, D., Yeh, S.-W. and Kug, J.-S. (2023) Sub-seasonal variability of ENSO teleconnections in western North America and its prediction skill, Journal of Geophysical Research - Atmospheres, 128, e2022JD037985.

_____, Son, S.-W., Lim, Y. and Choi, J. (2022) Quasi-biennial oscillation-related surface air temperature change over the western North Pacific in late winter, International Journal of Climatology, 30, 4351-4359.

_____, and Choi, J. (2018) Granger Causality Test between ENSO and Winter Climate Variability over the Korean Peninsula, Journal of Climate Change Research, 9, 171-179 [In Korean].

_____ (2022) Relationship between the QBO and Surface Air

Temperature in the Korean peninsula, Atmosphere-KOREA, 32, 39-49 [In Korean].

국문 초록

열대 지역에는 ENSO(El Niño-Southern Oscillation)와 QBO(Quasi-Biennial Oscillation)라는 두 가지 주요 모드가 존재한다. 열대 해수면 온도의 경년 변동인 ENSO와 열대 성층권 동서방향 바람의 준2년 주기 변동인 QBO다. 이 두 모드는 열대 지역의 겨울철 변동성의 90% 이상을 설명하는 동시에 원격 상관을 통하여 중위도 지상 기후에도 막대한 영향을 미친다고 알려져 있다. 따라서 ENSO와 QBO의 영향을 정확하게 이해하고 이를 겨울철 동아시아 지상 기온 예측에 활용하는 것이 중요하다. 그러나 그동안의 연구가 겨울철 평균적인 영향에만 한정되어 있었기 때문에, 이들이 계절내 시간규모에서 어떠한 영향을 미치는 지에 대한 연구가 상대적으로 부족한 실정이었다. 따라서 본 학위 연구는 두 열대 모드가 계절내-계절 시간 규모에서 동아시아 지상 기후에 미치는 영향 및 메커니즘을 조사하여 예측에 활용가능한 가이던스를 제시하고자 하였다. 그 결과, 아래와 같이 세 가지 의미 있는 발견을 하였다.

첫째로, 이들이 동아시아에 미치는 영향이 계절내 변동하고 있으며, 영향의 시기가 서로 구분될 수 있다는 점을 발견하였다. 12월 초겨울은 ENSO가 동아시아에 지배적인 영향을 미치는 것으로 나타났다. 이 시기의 ENSO-동아시아 원격상관은 뚜렷한 양(+)의 관계를 띄며 쿠로시오 지역의 대기 순환장 변동에 의해 조절되는 것으로 나타났다. 그러나 2-3월 늦겨울이 되면서 ENSO의 영향은 약해지고 상대적으로

QBO의 영향이 지배적이게 되는 것으로 나타났다. 이때 QBO-동아시아 원격상관은 뚜렷한 음(-)의 관계를 띄며 아시아-태평양 제트의 남북변동과 밀접한 관련이 있는 것으로 나타났다. 이는 겨울철 동아시아의 계절내-계절 예측에 기존의 기후 인자들(해빙, 눈덮임 등등)뿐만 아니라 ENSO와 QBO를 함께 고려해야 하고, 특히 1990년대 이후로 뚜렷해진 QBO-동아시아 원격상관을 현재보다 적극적으로 활용해야 함을 나타낸다. 또한 초겨울의 ENSO, 늦겨울의 QBO처럼 이들의 영향 시기를 달리 고려해야 함을 다시 한번 더 강조하였다.

둘째로, 원격상관의 핵심 메커니즘을 발견하였다. ENSO-동아시아 원격상관은 ENSO와 관련된 열대 대류 활동 변동에 야기된 로스비파의 선형 조합의 결과로써 쿠로시오 지역의 대기 순환장이 강화되기 때문으로 나타났다. 엘니뇨 시기에 인도양의 대류활동은 증가하고 Maritime Continent의 대류활동은 감소하는데 여기서 유도된 로스비파는 쿠로시오 지역에서 보강간섭을 야기하는 것으로 나타났다. 그 결과, ENSO-동아시아 원격상관을 강화되고 엘니뇨 해 동아시아는 평년 대비 따뜻해지는 경향을 보였다. 이러한 보강간섭에는 열대 대류가 배경장보다 상대적으로 더 중요한 역할을 하였고, 12월에 두 열대 대류활동이 강화되기 때문에 ENSO-동아시아 원격상관 또한 강화되는 것으로 나타났다. 반면, QBO-동아시아 원격상관은 아열대 하부 성층권과 상부 대류권의 배경장 및 에디 변화에 의해 발생하는 제트의 남북변동에 의해 조절되는 것으로 나타났다. QBO가 서풍인 경우, 적도 하부 성층권 지역의 서풍 연직시어와 양의 온도 아노말리는 해당

지역으로 향하는 파를 강화시키는데, 이는 아열대 하부 성층권과 상부 대류권에 에디 모멘텀 수렴 및 아시아-태평양 제트의 남하를 유도한다. 제트의 남하는 북태평양 지역에 저기압성 순환장을 유도하여 동아시아에 평년대비 차가운 공기의 이류를 야기하였다. 이를 통하여 동아시아에 QBO의 세 가지 영향 경로(북극 경로, 아열대 경로, 열대 경로)중 두 번째 경로가 가장 중요하다는 사실을 확인하였다. 또한 아시아-태평양 제트와 티벳 고원의 하부 지역에 위치한 동아시아의 지리적 영향으로 QBO의 영향이 동아시아에서 강할 수 밖에 없음을 확인하였다.

셋째로, 최신 예측 시스템과 기후 모형의 예측성 향상 방안을 제안하였다. ENSO-동아시아 원격상관의 경우, 최신 예측 시스템이 공간 분포는 어느정도 예측하였으나 계절내변동을 잘 예측하지 못하는 특징을 보였다. 반면, QBO-동아시아 원격상관의 경우, 현업 예측 시스템에서 잘 예측되었지만 기후 모형에서는 잘 모의되지 않는 특징을 보였다. 이러한 예측성 저하의 원인은 ENSO와 관련된 열대 대류활동의 계절내변동을 잘 모의하지 못하는 점과 QBO-동아시아 원격상관에 중요한 아열대 경로를 잘 모의하지 못하는 점에서 비롯되었음을 확인하였다. 따라서 동아시아 지상 기온 예측 향상을 위해서 초겨울의 열대 대류 및 이와 관련된 중위도 원격상관과 늦겨울의 QBO와 관련된 평균장 모의 능력을 향상시키는 게 중요함을 제안하였다.

주요어: 엘니뇨-남방진동, 준2년주기진동, 원격상관, 하향 커플링, 계절내-계절 예측

학 번: 2013-23010